Fall 2021

TRANSFORMATION INDUCED PLASTICITY IN A HIGH ENTROPY ALLOY, REUSING POWDER IN LASER POWDER BED FUSION OF INCONEL 718, AND GEOMETRIC FACTOR IN FRACTURE TOUGHNESS OF NANO-LAYERED COMPOSITES

Shubhrodev Bhowmik
University of New Hampshire, Durham

TRANSFORMATION INDUCED PLASTICITY IN A HIGH ENTROPY ALLOY, REUSING POWDER IN LASER POWDER BED FUSION OF INCONEL 718, AND GEOMETRIC FACTOR IN FRACTURE TOUGHNESS OF NANO-LAYERED COMPOSITES

BY

SHUBHRODEV BHOWMIK

B.Sc. in Materials and Metallurgical Engineering (MME), Bangladesh University of Engineering and Technology (BUET) 2017

THESIS

Submitted to the University of New Hampshire

in Partial Fulfillment of

the Requirements for the Degree of

Master of Science

in

Materials Science

September 2021

THESIS COMMITTEE PAGE

This thesis was examined and approved in partial fulfillment of the requirements for the degree of Master of Science in Materials Science by:

Dr. Marko Knezevic, Associate Professor (Mechanical Engineering)

Dr. James Krzanowski, Professor (Mechanical Engineering)

Dr. Todd Gross, Professor (Mechanical Engineering)

On August 4, 2021

Original approval signatures are on file with the University of New Hampshire Graduate School.

ACKNOWLEDGEMENTS

At first, I would like to thank Dr. Marko Knezevic for giving me the opportunity to perform research under his supervision. None of the research work would have been completed without his continuous support. Then, I would like to thank Dr. James Krzanowski for his help and guidance while my time as a graduate student. Furthermore, I would like to thank Dr. Todd Gross, Dr. James Krzanowski, and Dr. Marko Knezevic for agreeing to be part of my committee. I would also like to thank Jeff Miller from Applied Test Systems (ATS) for his assistance with the creep system, as well as Nancy Cherim, John Wilderman, and Mark Townley of the University Instrumentation Center for their collective support and mentorship. Moreover, I would like to thank Dr. Sven Vogel for all his help with neutron diffraction data analysis and my family and friends for their support throughout my graduate studies, specifically, baba, ma, dada, boudi, and my roommate Nikolay Dimitrov (Nick). Lastly, many thanks to my fellow graduate students (Dan, Nick, Evgenii, Adnan) for their support by providing necessary advice on the research work and Jie Wang, for his friendship as well as giving me rides during our frequent visits to the Olson center facility for performing creep tests.

Table of Contents

ABSTRACT

TRANSFORMATION INDUCED PLASTICITY IN A HIGH ENTROPY ALLOY, REUSING POWDER IN LASER POWDER BED FUSION OF INCONEL 718, AND GEOMETRIC FACTOR IN FRACTURE TOUGHNESS OF NANO-LAYERED COMPOSITES

by

Shubhrodev Bhowmik

University of New Hampshire

This research explores the effects of processing history and compressive strain on a microstructurally flexible high entropy alloy (HEA), $Fe_{42}Mn_{28}Co_{10}Cr_{15}Si_5$ (in at%) – named DP-5Si-HEA. The material was characterized by electron back scatter diffraction (EBSD), scanning electron microscopy (SEM) and neutron diffraction. The as-rolled material had metastable gamma austenite (γ), stable sigma (σ), and stable epsilon martensite (ε) phases at room temperature. Friction stirrer processing (FSP) at different tool speeds changed the microstructure by decreasing the grain size and varying the phase fractions because of low stacking fault energy of the chosen HEA. The HEA exhibited peak ultimate tensile strength of ~1850 MPa because of refined microstructure, transformation induced plasticity (TRIP) because of $\gamma \rightarrow \varepsilon$ phase transformation, and transformation-induced Hall-Petch-type barrier effect. Furthermore, an investigation on the effect of reusing powder on compressive, tensile and creep properties of Inconel 718 (IN 718) fabricated by laser powder bed fusion (LPBF) was carried out. To achieve that, room, and high temperature (600^0C, 650^0C,700^0C, 750^0C) tensile tests, room temperature compression tests, and high temperature (550^0C, 650^0C, 700^0C) tensile creep tests for samples prepared by both virgin as well as reused powder in LPBF were performed. The study showed the reused powder had higher strength at room and high temperature tensile tests except for 650^0C. The virgin powder lasted longer at 550^0C and 650^0C creep test, but the reused powder lasted longer at 700^0C. It was concluded in this study that the parts made by virgin powder samples should be used for

temperatures at creep conditions until 650^0C for the real-life applications. Moreover, finite element analyses were carried out on micro single edge notched bend (MSENB) specimens to obtain fracture toughness of Cu/TiN and Al/TiN nanocomposites within the realm of Linear Elastic Fracture Mechanics. The shape function or geometric factor was first calculated by considering the effects of the geometry, the cono-spherical indenter stress field, and the phase interface shielding/anti-shielding on the crack tip driving force. It was found that adding either Al or Cu nanolayers to TiN nanolayers did not weaken or significantly improve fracture toughness relative to the single TiN thin film. Based on the results, some recommendations were also made for future experiments.

INTRODUCTION

Exploring microstructural flexibility of recently developed high entropy alloys provides a great way to avoid the compromise between contrasting material properties like strength and ductility. Moreover, powder reusing during additive manufacturing to make the process more economical and environment friendly is a great concern for industry application. Furthermore, the effect of making nano-layered composites on fracture toughness are of growing interest in both academia and industry. This work discusses about these issues and consists of three chapters.

Chapter 1 contains the microstructural and textural examination of $Fe_{42}Mn_{28}Co_{10}Cr_{15}Si_5$ (in at%), also called DP-5Si-HEA, in its as-rolled, 350 rotations per minute (RPM) friction stirred processing (FSP), 150 RPM FSP, and double pass (350 RPM + 150 RPM) condition. Optical microscopy, neutron diffraction (NeD), and electron back scatter diffraction (EBSD) was performed for characterization. The as-rolled microstructure, which consisted of metastable γ-austenite, stable σ-phase, and stable ε-martensite phases, was further processed by three different parameters of FSP to take advantage of the metastability of γ phase while tuning its strength and deformation characteristics. Simple compression tests were performed on as-rolled and FSP materials to observe the strength, phase and texture evolution. Based on these data, the effect of initial microstructure (grain size, texture, phase content) on the phase transformation rate were rationalized and discussed. Furthermore, the changes in $\frac{c}{a}$ ratio with strain and its effect on deformation mechanism of ε-martensite phase was also discussed.

Chapter 2 contains discussion on the effects of powder reusing on the mechanical properties of Inconel 718 fabricated by laser powder bed fusion (LPBF). High temperature tensile and room temperature tensile and compression as well as high temperature tensile creep tests were

performed for samples from both virgin and reused powders. The initial microstructure was characterized by EBSD and showed Goss texture. The results of mechanical tests were also discussed in detail in this chapter.

In chapter 3, equations for calculating geometric factor, f were developed, and fracture toughness of laminated nanocomposites made by metals (Al or Cu) and ceramics (TiN) at different temperatures were estimated from micro single edge notched bend (MSENB) specimens. To that end, different crack lengths, a, were considered in both metal (Al or Cu) and ceramic (TiN) layers for a given geometry. f was calculated based on linear elastic fracture mechanics (LEFM), beam theory for composites, interface effects on the crack tip driving force, and the finite element method (FFEM). Fracture toughness values for Cu/TiN and Al/TiN multilayers with different layer thickness at several temperatures were estimated by using the equations obtained for f. It was observed that the leg geometry had significant effect on fracture toughness when crack ligament length was varied. The design of beam geometry against bending moment variation were also discussed in this chapter.

Results produced in first two chapters are intended for using as boundary conditions in polycrystal plasticity modelling. The combination of crystal plasticity modeling with experimental datasets of HEA and Inconel 718 could provide great insight into the micro-mechanics of observed systems.

CHAPTER 1:

Effects of plasticity-induced martensitic transformation and grain refinement on the evolution of microstructure and mechanical properties of a metastable high entropy alloy

This chapter has been submitted to Journal of Alloys and Compounds and is under review as: "Effects of plasticity-induced martensitic transformation and grain refinement on the evolution of microstructure and mechanical properties of a metastable high entropy alloy," Shubhrodev Bhowmik, Jianzhong Zhang, Sven C. Vogel, Saurabh S. Nene, Rajiv S. Mishra, Brandon A. McWilliams, Marko Knezevic.

In this work, I performed the characterization techniques such as: optical microscopy, scanning electron microscopy, electron backscatter diffraction, and energy dispersive spectroscopy (EDS). I prepared all samples for characterization. I also performed all the compression tests and carried out all the analysis using data from both characterization and mechanical testing. I performed the Rietveld analyses for neutron diffraction data. The text was written under the guidance of Dr. Marko Knezevic and other co-authors.

Effects of plasticity-induced martensitic transformation and grain refinement on the evolution of microstructure and mechanical properties of a metastable high entropy alloy

Shubhrodev Bhowmik[a], Jianzhong Zhang[b], Sven C. Vogel[b], Saurabh S. Nene[c,d], Rajiv S. Mishra[d], Brandon A. McWilliams[e], Marko Knezevic[a,*]

[a]Department of Mechanical Engineering, University of New Hampshire, Durham, NH, 03824, USA

[b]Materials Science and Technology Division, Los Alamos National Laboratory, Los Alamos, NM, 87545, USA.

[c]Department of Metallurgical and Materials Engineering, Indian Institute of Technology Jodhpur, Karwar, Jodhpur, Rajasthan 342037.

[d]Department of Materials Science and Engineering, University of North Texas, Denton, TX, 76207, USA.

[e]Weapons and Materials Research Directorate, DEVCOM Army Research Laboratory, Aberdeen Proving Ground, MD, 21005, USA.

Abstract

This paper describes the main results from an experimental investigation into tailoring the phase content and grain structure for high strength of a microstructurally flexible high entropy alloy (HEA), $Fe_{42}Mn_{28}Co_{10}Cr_{15}Si_5$ (in at%), using rolling, friction stir processing (FSP), and compression. Optical microscopy, neutron diffraction, and electron backscatter diffraction were employed to characterize microstructure and texture evolution. The material upon rolling was found to have triplex structure consisting of metastable gamma austenite (γ), stable sigma (σ), and stable epsilon martensite (ε) phases. The adaptive phase stability exhibited by the selected HEA of very low stacking fault energy with strain, strain rate, and temperature was used along with grain refinement to enhance the strength. To this end, the complex structure was refined by FSP at 350 revolutions per minute (RPM) tool rotation rate, while increasing the fraction of γ and decreasing the σ and ε content. The strength was further enhanced by FSP at 150 RPM by further refinement of the grain structure and increasing the fraction of ε phase. The peak ultimate tensile strength of ~1850 MPa was achieved by double pass FSP (350 RPM followed by 150 RPM), the sequence

* Corresponding author at: University of New Hampshire, Department of Mechanical Engineering, 33 Academic Way, Kingsbury Hall, W119, Durham, New Hampshire 03824, United States.

E-*mail address*: marko.knezevic@unh.edu (M. Knezevic).

which refined the microstructure even more and increased the fraction of σ phase. While the amount of σ phase created by diffusional transformation remains constant during subsequent compression, the fraction of ε increases due to the diffusionless, strain-induced $\gamma \rightarrow \varepsilon$ phase transformation. The transformation facilitates plastic strain accommodation and rapid strain hardening, which has been attributed to the increase in highly dislocated ε phase fraction and transformation-induced dynamic Hall-Petch-type barrier effect. Interestingly, a great deal of hardening ability was exhibited by the HEA even at very high strength. Roles of texture, grain size, and phase content on the transformation during compression have been rationalized and discussed in this paper.

Keywords: High entropy alloys; Friction stir processing; Phase transformations; Grain structure; Texture

1 Introduction

In an effort to maximize the strengthening effect of solid solution while avoiding brittle intermetallic phases, a special class of sophisticated materials termed high entropy alloys (HEAs) are being developed [9, 10]. These materials have shown the potential to improve the contrasting material properties of strength and ductility. An equiatomic HEA like $Fe_{20}Mn_{20}Ni_{20}Co_{20}Cr_{20}$ is an example HEA exhibiting outstanding strength, ductility, and fracture toughness at both cryogenic and room temperatures [9]. Beyond the equiatomic HEAs, other variants of the Fe-Mn-Ni-Co-Cr HEA system like $Fe_{40}Mn_{27}Ni_{26}Co_5Cr_2$ (at. %) or different types of non-equiatomic HEAs are being explored, e.g., $Al_{33.4}Co_{22.2}Cr_{11.1}Fe_{22.2}Ni_{11.1}$ (at. %) [11-15]. The primary advantage of HEAs pertains to the tunable microstructure and deformation characteristics by modifying the composition and processing. For example, dual phase HEAs (DP-HEAs) of Fe-Mn-Co-Cr were developed, e.g. $Fe_{50}Mn_{30}Co_{10}Cr_{10}$ (all in at. %) to contain austenite (γ) of face-centered cubic (FCC) structure, which is a metastable phase undergoing the strain-induced phase transformation to highly dislocated epsilon martensite phase (ε) with hexagonal close-packed (HCP) structure [14, 16]. The mechanism is referred to as the transformation induced plasticity (TRIP), and in addition to dislocation slip, is a predominant deformation mode in these alloys. As a result, these HEAs offer an opportunity to control volume fraction and thermodynamic stability of γ-austenite and ε-martensite to increase both ductility and strength [11, 12, 14]. In addition to TRIP and slip, twinning induced plasticity (TWIP) can also operate in HEAs offering an additional degree of freedom for plastic deformation and hardening [17]. Accordingly, the stacking fault energy (SFE) of a given alloy must be low enough to decrease the critical stress for twin formation or to allow the separation between partial dislocations forming shear bands of ε-martensite phase [18]. The TWIP is promoted in the range $\sim 20 < SFE < 40$ mJ/m^2, while the TRIP is promoted for SFE$<\sim$15 mJ/m^2 [19-23].

Studies into the effect of increasing Cr at the expense of Fe and Mn alloying elements on γ phase in DP-HEA have been carried out in [22, 24]. It was found that adding extra Cr increases the driving force of $\gamma \rightarrow \varepsilon$ phase transformation. For example, in the case of $Fe_{47}Mn_{28}Co_{10}Cr_{15}$, the extra 5% of Cr decreases the γ phase fraction at room temperature with a very small change to the onset temperature (T_0) of transformation. Additionally, the effect of adding non transition elements such as C, Al, and Si on Fe-Mn alloys was explored using thermodynamic simulations [24].

Following these initial works, the effect of Si in $Fe_{47}Mn_{28}Co_{10}Cr_{15}$ alloy was investigated with thermodynamic calculations. The work found that adding 5% of Si increases the T_0 to a threshold value of 425 ^{0}C as well as the metastability of γ phase [25]. Si has the advantage over other elements like Ni and Al, by providing increased γ phase metastability and higher T_0 value (i.e. stable ($\gamma + \varepsilon$) phase field until a higher temperature). As a result, a new composition was developed with an alloy chemistry of $Fe_{42}Mn_{28}Cr_{15}Co_{10}Si_5$ (all in at. %) referred to as DP-5Si-HEA. The alloy in its as-cast condition exhibits about 100 MPa increase in YS relative to the as-cast $Fe_{50}Mn_{30}Co_{10}Cr_{10}$ DP-HEA, while ~600 MPa increase in YS after M-pass (performing three overlapping passes with 650 rotations per minute (RPM) down to 350 RPM in the second pass and the last pass being carried out at 250 RPM) compared to the as-cast DP-HEA counterpart [11, 12, 25]. Recently, a HEA ($Fe_{40}Mn_{20}Co_{20}Cr_{15}Si_5$ (all in at. %), also known as CS-HEA because of the increased amount of Co and added Si relative to the reference DP-HEA, $Fe_{50}Mn_{30}Co_{10}Cr_{10}$, from [12], was developed to take the advantages of both TRIP and TWIP [14, 20]. In this alloy, increased Co in addition to Si stabilize and promote ε-martensite by lowering the SFE [21-23]. The large fraction of ε phase promotes strain accommodation by twinning and pyramidal slip. Interestingly a decrease in $\frac{c}{a}$ ratio of ε-martensite from 1.619 in the initial microstructure to 1.588 at fracture upon tension was reported for this alloy [26].

The enhanced metastability of γ phase can also enhance the temperature, strain, and strain rate sensitive phase evolution in HEAs during thermomechanical processing [21-23]. To this end, deformation processing of such material via rolling or forging can substantially change their microstructure [20]. The microstructural changes can be even more dramatic by processing of the material using high temperature severe plastic deformation techniques such as equal channel angular pressing (ECAP), high pressure torsion (HPT), and friction stir processing (FSP) [27-29]. Significant enhancements in strength and ductility over as-cast $Fe_{40}Mn_{30}Co_{10}Cr_{15}Si_5$ (in at%) HEA was obtained via FSP processing because of intense grain refinement and larger fraction of high angle grain boundaries [17, 29, 30]. In contract, intense grain refinement via fragmentation of grains due to dislocation storage in ECAP and HPT results in large fractions of low angle grain boundaries [31, 32].

The as-cast DP-5Si-HEA provides the ($\gamma + \varepsilon$) mixture with more dominance of γ phase [25]. The multi-pass friction stir processing of the alloy (M-pass, 3 overlapping passes with 650

rotations per minute (RPM) in the first pass down to 350 RPM in the second pass and to 250 RPM in the third pass) refined the grain size from 100 μm to 1.3 μm as well as increased the ε phase fraction [25]. The FSP increased the yield strength (YS) to 950 MPa with an ultimate tensile strength (UTS) of 1.15 GPa relative to the cast 400 MPa YS. The alloy after FSP had a ductility of 7%. These improvements in mechanical properties after FSP have been associated to the increase in metastability of γ phase, which promotes $\gamma \rightarrow \varepsilon$ phase transformation and subsequent twinning in the ε phase.

To complement the above research involving the as-cast DP-5Si-HEA and FSP, this paper studies the changes in the microstructure and associated mechanical properties upon hot rolling of the $Fe_{42}Mn_{28}Co_{10}Cr_{15}Si_5$ (in at%) composition (DP-5Si-HEA). The evolution of microstructure and texture was measured by optical microscopy, neutron diffraction (NeD), and electron back scatter diffraction (EBSD). The material upon rolling was found to have triplex structure consisting of metastable γ-austenite, stable σ-phase, and stable ε-martensite phases. The rolled HEA was further processed by FSP using a range of process parameters to potentially take advantage of metastability of γ phase while tuning its strength and deformation characteristics. Simple compression tests were performed on as-rolled and FSP materials to study strength and the evolution of phases: volume fraction, size, and texture. These microstructural features were measured and quantified. Based on the data, roles of texture, grain size, and phase content in the initial microstructure on the transformation rate in the presence of three phases and associated mechanical properties during compression have been rationalized and discussed. Moreover, the changes of the c/a ratio was observed and underlying implications on the shifts in active deformation mechanisms and ductility have been discussed.

2 Experimental procedures

2.1 Material processing

The rolled plate of $Fe_{42}Mn_{28}Co_{10}Cr_{15}Si_5$ (in at%) HEA was received from Sophisticated Alloys, Inc. After casting a 50.8 mm thick ingot, the ingot went through a homogenization heat

treatment at 1100^0C for 2 hrs. After heat treatment, the ingot was rolled into a plate of 8.9 mm thickness in multiple passes.

The rolled plate was processed by FSP following the procedures presented in [33, 34]. A W-RE processing tool was used with a shoulder diameter of 12 mm and the root diameter of 7.5 mm. The shoulder also contained a tapered pin of 6 mm in diameter and 3.5 mm in length. Since the length of the tool was 3.5 mm, the depth of FSP beads would be ~3.7 mm. Based on the bead dimensions, the diameter and height of the compression cylinders were determined.

Three different FSP beads were created with varying tool rotational rates in the plate. The 1st FSP bead was made with a tool rotational rate of 350 RPM (100 mm long bead), the 2nd bead was made with 150 RPM tool rotational rate (80 mm long bead), and the 3rd bead was made with two overlapping passes of 350 RPM followed by 150 RPM tool rotational rate (120 mm long bead). The traverse speed was 50.8 mm/min for all. The FSP was performed along the transverse direction (TD) of the rolled plate. Samples for compression were machined from the four regions and classified into four categories: as-rolled, 350 RPM FSP, 150 RPM FSP, and 350 RPM followed by 150 RPM FSP denoted as “A”, “B”, “C” and “D”, respectively.

2.2 Mechanical testing

Cylinders for compression testing were machined by wire electrical discharge machining (EDM) in two plate directions: (1) the in-plane (IP) along the TD direction, the direction which is also parallel to the FSP direction (FSPD) and (2) the through thickness (TT) direction or the normal direction (ND) of the plate. The purpose of making samples in two different directions is to evaluate any plastic anisotropy in compression. 3 mm and 4 mm diameter TT and IP cylinders were made for the four categories of samples. Height of B, C, and D category cylinders was 3 mm in both TT and IP directions. Only 3 mm diameter cylinders were used for the IP direction testing because of the bead height. Height of the A category cylinders was 4.8 mm.

An Instron servo hydraulic testing machine model #1350 was used for compression testing. The tests were performed at room temperature and under a constant strain rate of $10^{-3}/\mathrm{s}$. The machine is equipped with a load cell of 100 kN capacity, hardened steel compression fixtures, and DAX software. Oil was used as a lubricant to minimize the effects of friction between compression

dies and the sample. By placing a ball between the upper force arm and upper die, uniaxial state of the test was better ensured. The compliance of the testing setup was measured and subtracted from the raw compression data to correct load vs. displacement data before calculating the true stress-true strain curves. The tests were performed either to fracture or interrupted at given strain levels. Samples upon the interrupted tests were used to measure microstructural evolution. The tests to fracture were repeated at least three times to ensure accuracy of the data.

2.3 Microstructural characterization

2.3.1 Microscopy

To characterize the microstructure both optical microscopy and EBSD in a scanning electron microscope (SEM) were performed. The optical imaging was performed using Olympus OLS5000 capable of performing scans by both laser and incoherent light. All the images reported here were taken by laser. The EBSD was performed in a Tescan Lyra (Ga) field emission type of SEM equipped with Pegasus system (Octane Plus SDD detector and Hikari High Speed Camera). Scans were performed in the depth mode with a spot size of 50 - 320 nm and 19.4 -20 beam intensity (BI) at a voltage of 10-15 kV. The working distance was kept at ~8.9 mm. To obtain statistically significant data, multiple scans were taken for each category of the materials. For samples with bigger grains, larger areas were scanned, while for fine grains samples, the scan size was small. All the scans contained about 500,000 - 1,000,000 points with step size 0.2-0.6 μm for scans with bigger grains and 0.03-0.05 μm for scans with fine grains. Post processing of collected data was performed using the analysis software package OIM 8.

The samples from all categories were prepared by grinding with SiC papers from 180 to 1200 grit. After grinding, the samples were polished by 3, and 1 μm glycol based polycrystalline diamond solution with red lubricant. As for the final step, 0.05 μm master-prep alumina was used. The optical microscopy imaging was performed after etching with Kalling's-2 reagent for 5-10 s. The etching solution is comprised of 5g of $CuCl_2$, 100 ml of HCl, 100 ml ethanol (C_2H_5OH).

Energy dispersive spectroscopy (EDS) was also carried out at 15 kV voltage and 9 mm working distance to observe the elemental composition of phases present in the microstructure.

2.3.2 Neutron diffraction

NeD was performed in Los Alamos Neutron Science Center (LANSCE) at Los Alamos National Laboratory [35]. The facility is equipped with a time-of-flight (TOF) high-pressure-preferred orientation (HIPPO) neutron diffractometer with pulsed neutron source. The diffractometer contains five HIPPO detector rings at the nominal diffraction angles of 144°, 120°, 90°, 60°, and 40°. The cylinders were oriented such that the loading direction (LD) is perpendicular to the incoming neutron beam. Three different sample orientations (0°, 67.5°, and 90°), with each having count time about an hour and average proton current 100 μA, provided 132 histograms from all five detector rings. For phase analysis, the diffraction data was binned with 5 rings and three rotations were integrated to create single histograms for each detector rings or banks. These made the phase analysis largely free from the texture influence for each bank and easier to identify the minority phases. The orientation distribution function (ODF) was calculated from 132 histograms, which were binned with 45 panels. This way of analysis provided the necessary statistical accuracy for texture analysis since all 132 histograms are being fitted to complete the whole Debye ring. A software package called Maud was used to analyze the experimental histograms [36].

3 Results

3.1 Mechanical testing

True stress – true strain curves recorded during compression testing of the materials in the four conditions are shown in Fig. 1. As is evident, the as-rolled A material category has the lowest strength. The as-rolled material is approximately isotropic and able to accumulate more compressive strain in IP than in TT. The strength of the material increases with FSP. Since FSP was performed at different tool rates, the true stress – true strain curves and underlying microstructures are different. Decreasing the tool speed from 350 RPM to 150 RPM and performing the double pass increase the strength of the material. The D category material tested along the IP direction exhibits the highest strength reaching 1850 MPa UTS. The increase in strength from C to D material did not result in substantial loss of strain to fracture. This is attributed to similar accommodation of plastic strain in the samples, and in particular, to the extent of the

TRIP effect. The FSP materials show some anisotropy with the higher strength in the IP than in the TT direction. The directional dependence of the compressive strength is attributed to the microstructure morphology created by FSP and the difference in the rate of TRIP with texture. To rationalize the strength behavior of the materials, microscopy and NeD characterizations were performed, and these results are presented in the next section.

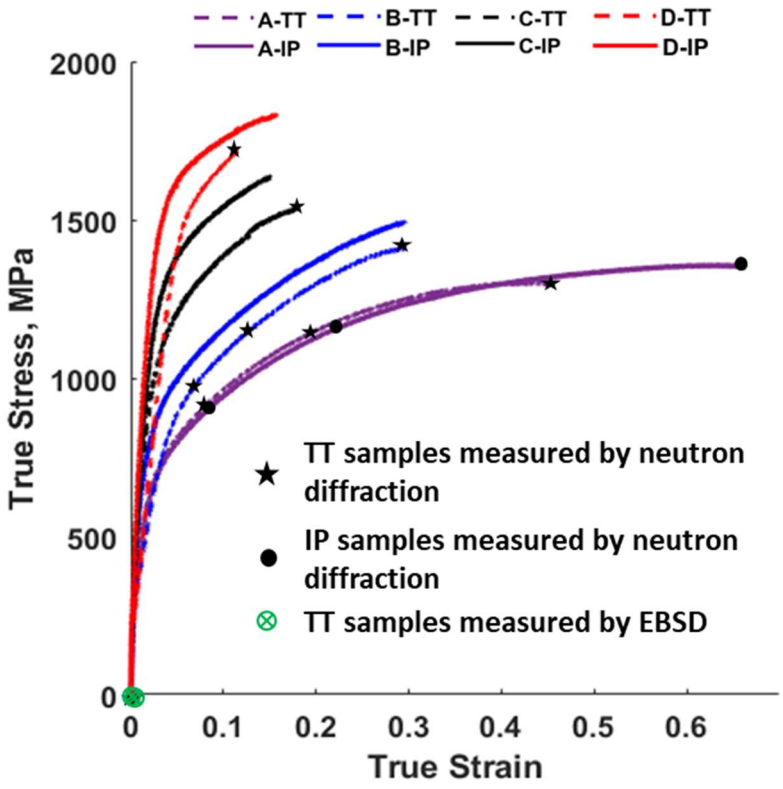

Figure 1: True stress - true strain curves for the four categories of the samples compressed to fracture in both in-plane (IP) and through thickness (TT) directions. Several compression tests are interrupted before fracture at the strain levels indicated by the symbols for the NeD and EBSD characterization.

3.2 Microstructural characterization

3.1.1 EBSD

The inverse pole figure maps (IPF) and phase maps are shown in Fig. 2 for the four material categories before compression testing. Three phases are identified with green, red, and yellow

colors, which corresponds to γ-austenite, ε-martensite and σ-phase. While the γ and ε phases are solid solution of all the 5 elements (Fe, Mn, Co, Cr, Si), the σ phase is an intermetallic of slightly increased Fe and Cr content with tetragonal crystal structure. The higher percentage of Cr (>15 wt%) increases the probability of σ-phase formation in the range between 600^0C and 1000^0C at favorable cooling rates in stainless steels [37, 38]. However, the use of Si along with higher Cr than typical for the Fe-Mn-Co-Cr systems (10 at%) can increase the propensity of σ-phase precipitation [39, 40].

The average grain size of γ phase was estimated in every scan and provided in Table 1. The grain size was estimated keeping the grain misorientation angle at 15°. The annealing twins observed in A-TT were not considered during the grain size calculation. As is evident, the as-rolled A category samples have the largest average grain size of ~20 μm. Because the as-rolled grain structure is refined with FSP, the average grain size in the B category samples is ~4 μm. The FSP conditions at 350 RPM provide a heat input into the material facilitating some grain growth and increase in the amount of γ phase content. The fraction of ε and σ phase slightly decreased in B samples relative to A samples. As a consequence of FSP at 150 RPM, the C category samples have average grain size of ~2 μm. Grain refinement as well as an increase in the ε phase volume fraction is achieved with the FSP at 150 RPM relative to the A samples. The D category samples showed both the major grain size refinement and a major increase in the σ phase volume fraction relative to the A category material. The D category samples show similar γ phase fractions to C category but the finest average grain size (~1 μm) because of the double pass FSP. The IPF maps of the FSP materials show some elongation of grains along the FSPD governing some anisotropy.

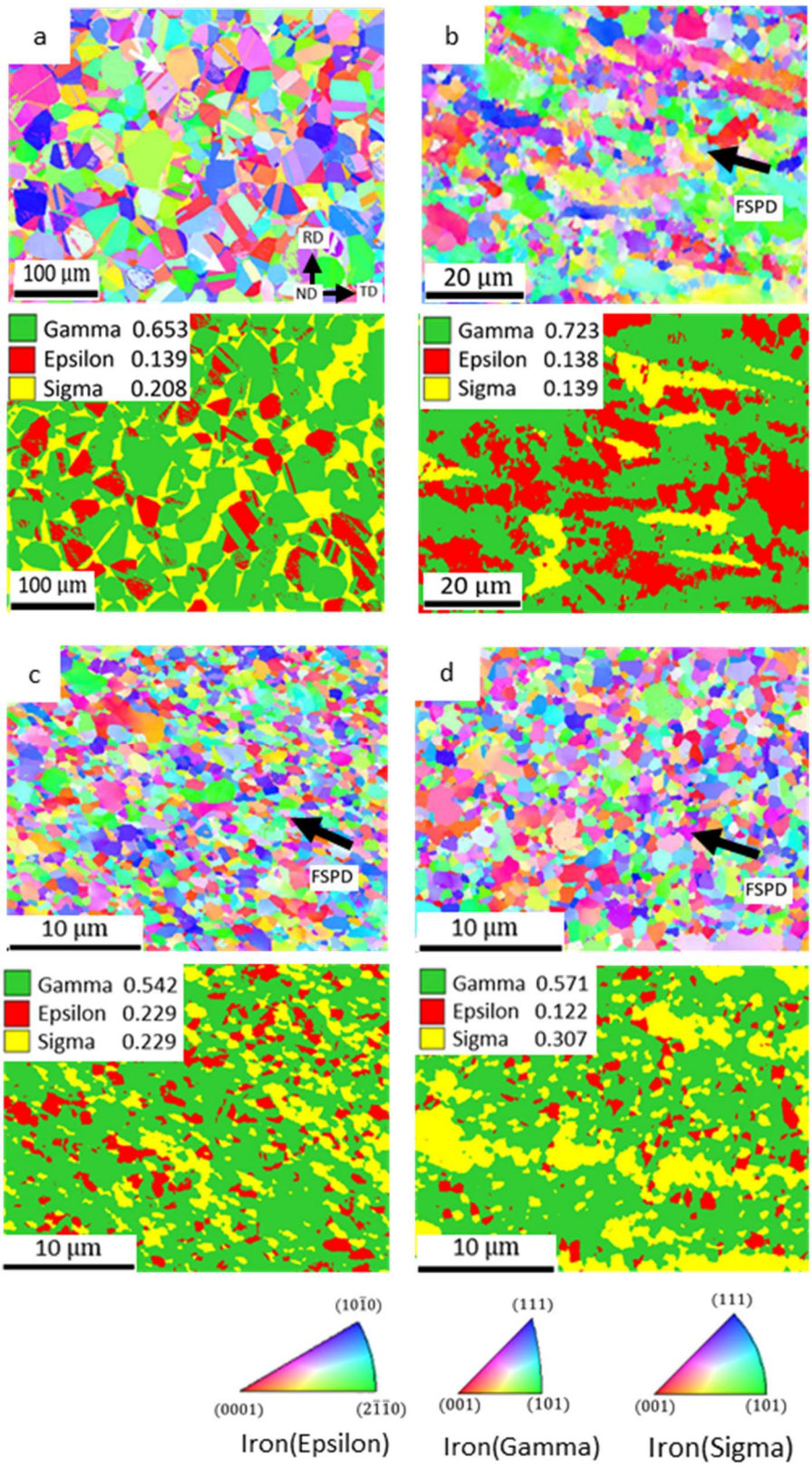
a
100 µm
RD
ND
TD
Gamma 0.653
Epsilon 0.139
Sigma 0.208
100 µm
b
FSPD
20 µm
Gamma 0.723
Epsilon 0.138
Sigma 0.139
20 µm
c
FSPD
10 µm
Gamma 0.542
Epsilon 0.229
Sigma 0.229
10 µm
d
FSPD
10 µm
Gamma 0.571
Epsilon 0.122
Sigma 0.307
10 µm
(10$\bar{1}$0)
(0001)
(2$\bar{1}\bar{1}$0)
Iron(Epsilon)
(111)
(001)
(101)
Iron(Gamma)
(111)
(001)
(101)
Iron(Sigma)

Figure 2: Inverse pole figure and phase maps acquired by EBSD for samples: (a) A-TT-initial (as rolled), (b) B-TT-initial (FSP at a tool speed of 350 rpm), (c) C-TT-initial (FSP at a tool speed of 150 rpm), and (d) D-TT-initial (double pass - FSP with two consecutive runs at tool speeds of 350 RPM and 150 RPM, respectively). Perpendicular to the maps is the sample TT direction. The colors in the IPF maps represent the orientation of ND/TT sample axis with respect to the crystal lattice frame according to the coloring in the standard IPF triangles. Phase fraction values are averages of at least two scans. Annealing twins are present in the A category samples and indicated with dark orange arrows.

Table 1: Average grain size in γ phase per sample category.

Category	FCC (μm)
A-TT-initial	20
B-TT-initial	4
C-TT-initial	2
D-TT-initial	1

3.1.2 Neutron diffraction analysis

The integrated histograms for 144^0 detector banks are shown in Fig. 3 for A-IP sample category for initial ($\epsilon = 0$), $\epsilon = 0.098$, $\epsilon = 0.216$ and fractured ($\epsilon = 0.669$) samples. Although there are four main categories of samples, histograms from only A-IP are shown to present the phase identification procedure. Such data for the other samples look similar. The Bragg reflections for the present phases are identified in the figure. It is evident that the intensity of γ phase decreases with increasing the amount of compressive strain, while the intensity of the ε phase increases. A procedure for extracting phase fractions from neutron diffraction in Maud was described in detail in [41]. Similar procedure was used here to analyze the phase fractions for the HEA material, as

briefly described below. The integrated experimental histograms were fit by calculating the contribution of individual phases present in the samples along with the contribution from the background.

Since the height of cylindrical samples was about 3-4 mm, the diffraction peaks from α and γ phases from screws made of stainless steel were observed. These screws were used to mount the sample onto the holder. During neutron diffraction Cd foil shields the sample holder in order to stop originating peaks from the holder. The slit (2 mm) used to focus the neutron beam onto the sample was also made of Cd [42]. The Cd peaks were observed to the backscatter (144^0, 120^0) banks emerging from the Cd slit. Additionally, the neutron spallation inside the metal tube during the production of neutron beam changes the wavelength of part of the beam and shows up as a hump in the histogram of 144^0 detector bank. After isolating the peaks from the background, the histograms were fitted with the phases present in the HEA samples to get the phase fractions.

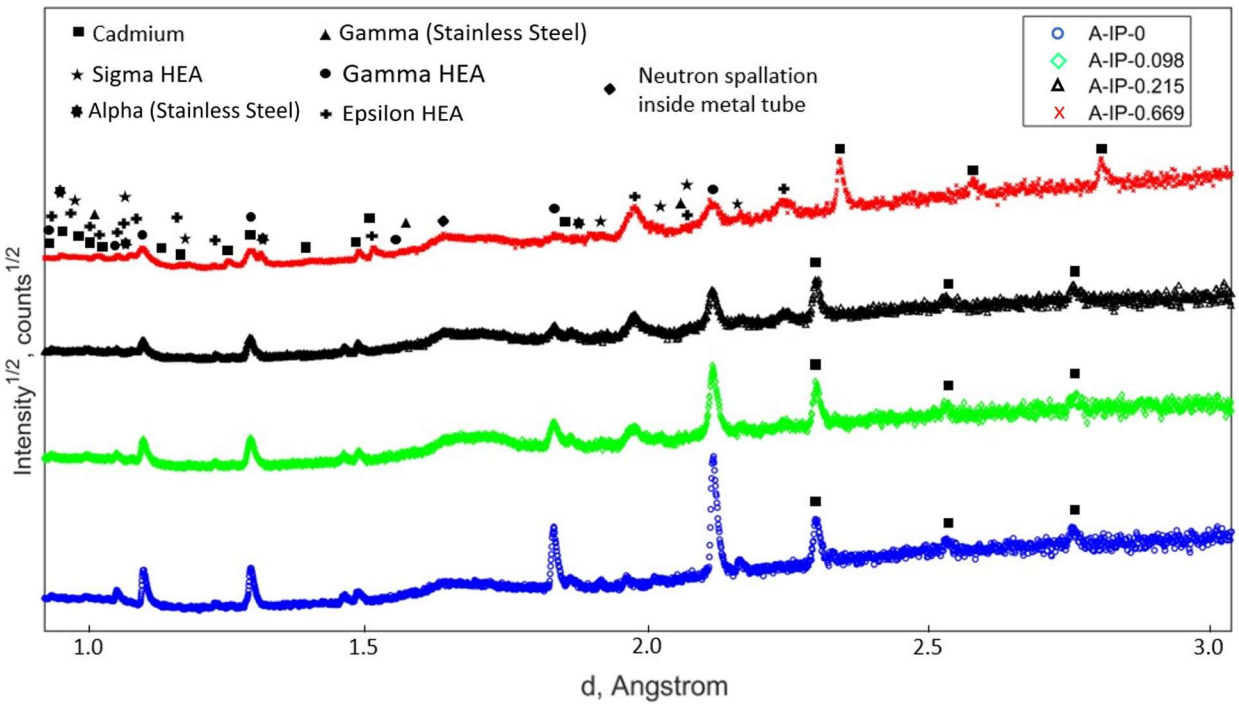

Figure 3: Phases in the neutron diffraction histograms for initial ($\epsilon = 0$), $\epsilon = 0.098$, $\epsilon = 0.216$ and fractured ($\epsilon = 0.669$) samples from A-IP category for 144 banks. The data from 2 mm slit is presented. The y-axis represents the square-root of the intensity of peaks in the square root of counts of photons, while the x-axis denotes the interplanar spacing (d-spacing). Since sigma phase has tetragonal crystal structure and has a lot of peaks, only selected ones were identified here.

Some additional peaks are also identified such as cadmium, neutron spallation inside metal tube, and alpha and gamma phases from stainless steel. Cadmium was used to shield the sample holder and as the slit during measurement and the peaks are only observed to the back scatter (144^0, 120^0) banks. The stainless steel (alpha and gamma phases) peaks originated from the screws, used to mount the small cylinders to a holder.

As mentioned in the previous sections, three phases of the HEA samples were extracted from the diffraction peaks. The Rietveld refinement was in the core of the procedure. The refinement was performed by refining the relevant crystallographic and scaling parameters of all the phases to increase the quality of least square fit between calculated and experimental diffraction histograms. At first, a fourth order polynomial was selected to fit each histograms background. After getting the background intensity of the calculated histogram close to the experimental one, the background was not refined in the further stages to avoid Cholesky negative diagonal per sample. The diffractometer constants (DIFC) were continuously refined in all steps through refining the basic parameters. In doing so, the lattice parameters of the three phases were also identified and has been discussed later. The micro-strain, which contributes to the peak broadening, was initially set to 6×10^{-4} $\mu\epsilon$ assuming a little effect on peak broadening. As refining heavily correlated variables such as crystallite size and micro-strain together can cause convergence issues, the crystallite size was kept fixed at ~1000 nm (meaning no peak broadening due to crystallite size in NeD). Since the atomic displacement parameters, B_{iso}, for the ε phase was not available in the literature, a weighted average of the B_{iso} of all five constituent elements (based on the at% of each element present in the material) was taken to get $B_{iso} = 0.43$. The B_{iso} of constituent elements were taken from the literature [43] and the intermetallic σ phase B_{iso} was kept at 0.8. The B_{iso} values were not refined during refinement process. After achieving convergence, the micro-strain was slightly refined. Since the crystallite size was kept fixed, the increase in the micro-strain values during the fitting is an indication of peak broadening and underlying increase in the dislocation density [44]. The atomic partial occupancies were set by literature values for all three phases and were not refined [45-47]. The parameters were refined in series to allow for convergence through the least-square fitting process.

The dependence of phase fraction on strain is presented in Fig. 4. The most evident change in the plots is the transformation of γ phase to ε as a consequence of the strain induced transformation process. The trends are approximately linear. In contrast to γ and ε, the σ phase

fraction is unchanged under the compressive strain. The measurement for A-IP samples were performed with a 2 mm slit and without a slit. The purpose of using a slit was to focus the neuron beam just on the sample and increase the accuracy. We can notice that the phase fractions obtained from 2 mm slit and without slit diffraction data are nearly identical verifying the accuracy of the measurements. The 2 mm slit neutron diffraction data was used to get the trend in phase transformation. Table 2 includes the linear trend fit parameters.

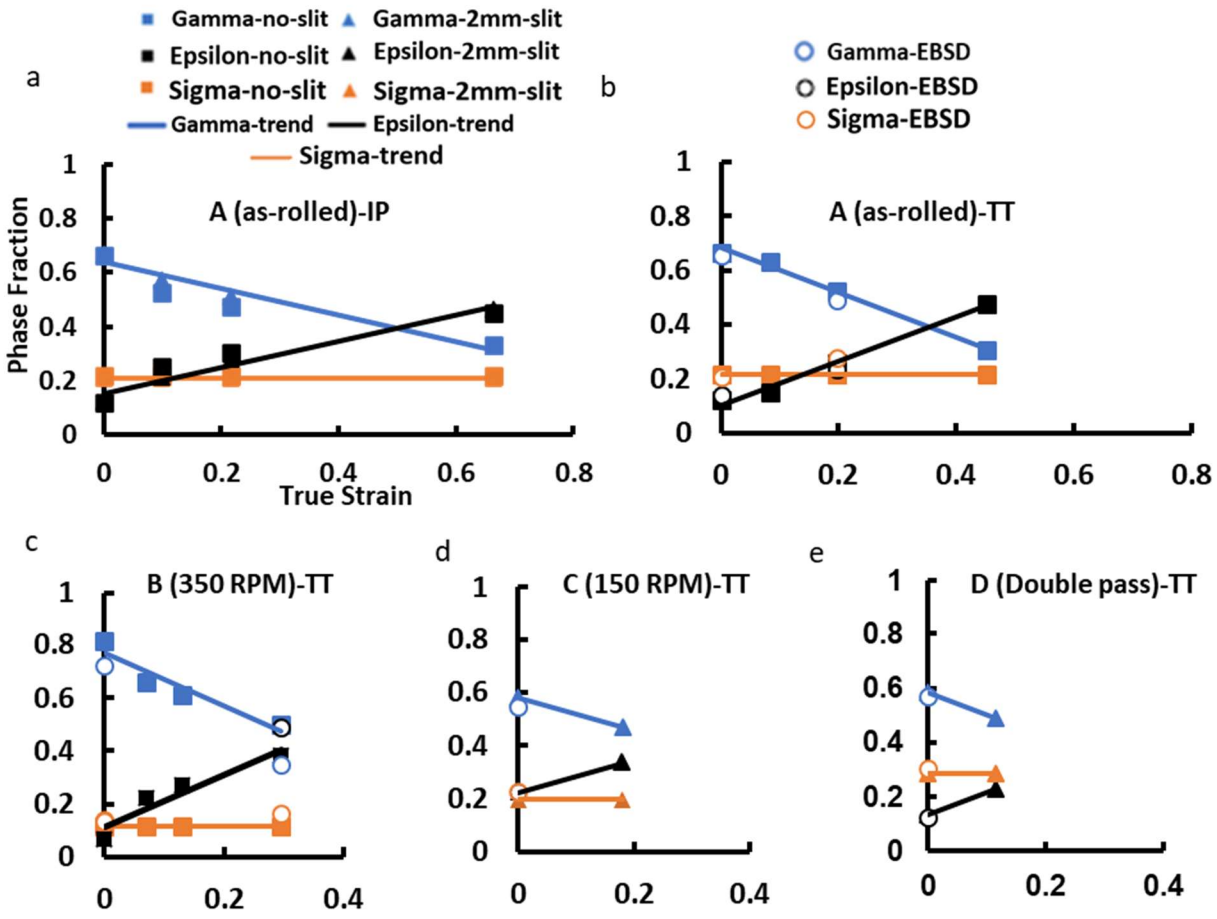

Figure 4: Evolution of phase fractions with plastic strain in compression for: (a) A-IP, (b) A-TT, (c) B-TT, (d) C-TT and (e) D-TT samples.

Table 2: Summary of the linear trend parameters for the evolution of phase fractions with plastic strain during compression measured by NeD: $P(\epsilon) = C_0 + C_1 \epsilon$; P = phase fraction and ϵ = true strain.

Category	Phase	C_0	C_1	R^2
A-TT	Gamma	0.682	-0.818	0.99
	Epsilon	0.100	0.818	0.99
	Sigma	0.218	0	---
A-IP	Gamma	0.639	-0.489	0.97
	Epsilon	0.151	0.485	0.97
	Sigma	0.210	0	---
B-TT	Gamma	0.768	-0.989	0.92
	Epsilon	0.113	0.989	0.90
	Sigma	0.118	0	---
C-TT	Gamma	0.579	-0.615	1.00
	Epsilon	0.223	0.615	1.00
	Sigma	0.197	0	---
D-TT	Gamma	0.583	-0.840	1.00
	Epsilon	0.132	0.840	1.00
	Sigma	0.285	0	---

During TOF neutron diffraction analysis, the sample has to be placed within ~0.1 m of the diffractometer center to achieve a precision of 10^{-4} to the lattice parameter. Otherwise, the diffractometer constant ($1/L\sin\theta$, where L is the total flight path) will be changed which could

provide different lattice parameters [48, 49]. Since the cylinders were very small, it was difficult to achieve the exact alignment while mounting on the holder. Hence, the lattice parameters in neutron diffraction are accurate to about three significant figures. From the phase fraction analyses of many samples, the average lattice parameters are inferred along with the standard deviation values: $a_{gamma} = 3.62374 \pm 0.02700$ Å, $a_{sigma} = 8.87510 \pm 0.07997$ Å and $c_{sigma} = 4.64307 \pm 0.04558$ Å with a ratio of 0.52315. These values agree well with the literature [45, 47]. Unlike the lattice parameters of γ and σ, we observe changes in the lattice parameters of ε-martensite. Such changes can occur due to the changes in chemical ordering or phase separations. The $\frac{c}{a}$ ratio changes are shown in Fig. 5. Interestingly, we observe that the ratio decreases but then increases during compression of the A and B samples.

Pole figures showing crystallographic texture evolution for γ and ε are presented in Fig. 6. The Rietveld refinement of all the 132 histograms from NeD data was used to reconstruct an ODF per sample for every phase. The analysis was performed using E-WMIV texture algorithm following the process described in [35, 42]. The initial texture in γ of A material category is a typical rolling texture of FCC metals. As expected, the pole figures for γ phase exhibit strengthening of $\{110\}$ fiber along the loading direction with compressive strain. For ε phase, the texture strengthens along the RD direction is primarily a consequence of phase transformation and some slip. There is no signature of deformation twinning in the texture of ε phase. The σ phase texture was also calculated but is not shown since it is very weak and approximately random. Texture appears relatively weak in all phases in all samples meaning that it likely has secondary effects on anisotropy in the material properties.

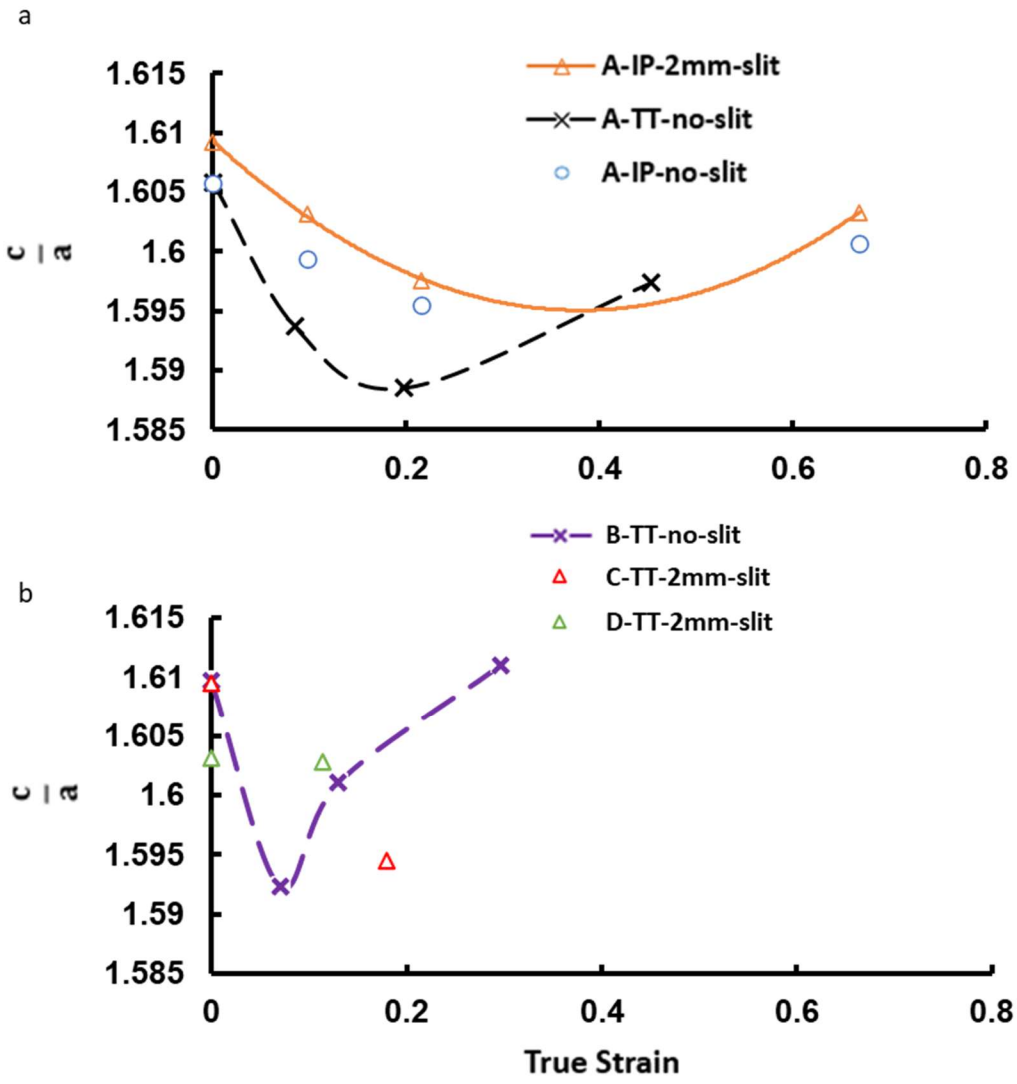

Figure 5: $\frac{c}{a}$ ratio measured by NeD for the samples from the four material categories.

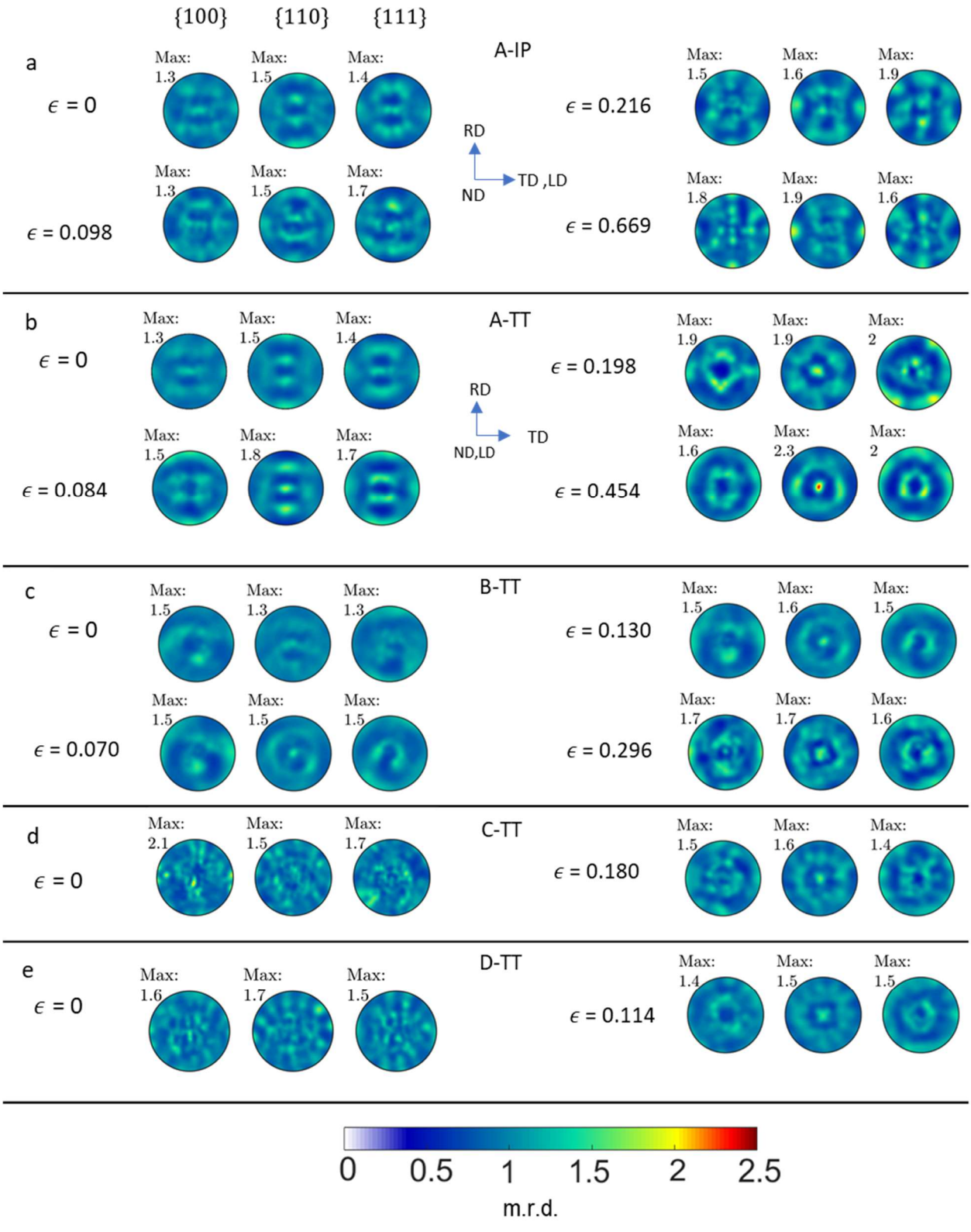
{100}
{110}
{111}
a
A-IP
ϵ = 0
Max: 1.3
Max: 1.5
Max: 1.4
ϵ = 0.216
Max: 1.5
Max: 1.6
Max: 1.9
RD
TD ,LD
ND
ϵ = 0.098
Max: 1.3
Max: 1.5
Max: 1.7
ϵ = 0.669
Max: 1.8
Max: 1.9
Max: 1.6
b
A-TT
ϵ = 0
Max: 1.3
Max: 1.5
Max: 1.4
ϵ = 0.198
Max: 1.9
Max: 1.9
Max: 2
RD
TD
ND,LD
ϵ = 0.084
Max: 1.5
Max: 1.8
Max: 1.7
ϵ = 0.454
Max: 1.6
Max: 2.3
Max: 2
c
B-TT
ϵ = 0
Max: 1.5
Max: 1.3
Max: 1.3
ϵ = 0.130
Max: 1.5
Max: 1.6
Max: 1.5
ϵ = 0.070
Max: 1.5
Max: 1.5
Max: 1.5
ϵ = 0.296
Max: 1.7
Max: 1.7
Max: 1.6
d
C-TT
ϵ = 0
Max: 2.1
Max: 1.5
Max: 1.7
ϵ = 0.180
Max: 1.5
Max: 1.6
Max: 1.4
e
D-TT
ϵ = 0
Max: 1.6
Max: 1.7
Max: 1.5
ϵ = 0.114
Max: 1.4
Max: 1.5
Max: 1.5
0
0.5
1
1.5
2
2.5
m.r.d.

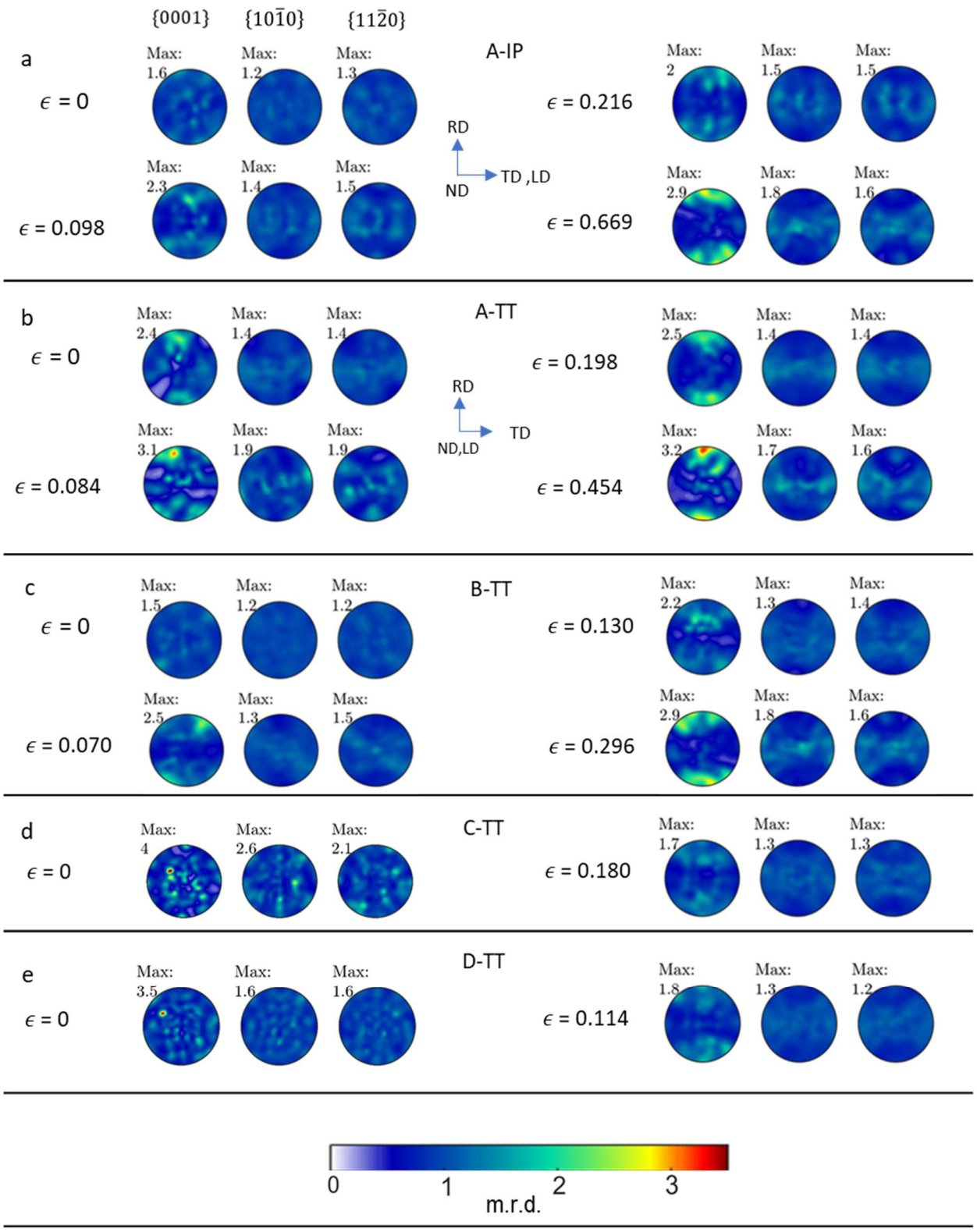
{0001}
{10$\bar{1}$0}
{11$\bar{2}$0}
a
ϵ = 0
Max: 1.6
Max: 1.2
Max: 1.3
A-IP
ϵ = 0.216
Max: 2
Max: 1.5
Max: 1.5
RD
TD ,LD
ND
ϵ = 0.098
Max: 2.3
Max: 1.4
Max: 1.5
ϵ = 0.669
Max: 2.9
Max: 1.8
Max: 1.6
b
ϵ = 0
Max: 2.4
Max: 1.4
Max: 1.4
A-TT
ϵ = 0.198
Max: 2.5
Max: 1.4
Max: 1.4
RD
TD
ND,LD
ϵ = 0.084
Max: 3.1
Max: 1.9
Max: 1.9
ϵ = 0.454
Max: 3.2
Max: 1.7
Max: 1.6
c
ϵ = 0
Max: 1.5
Max: 1.2
Max: 1.2
B-TT
ϵ = 0.130
Max: 2.2
Max: 1.3
Max: 1.4
ϵ = 0.070
Max: 2.5
Max: 1.3
Max: 1.5
ϵ = 0.296
Max: 2.9
Max: 1.8
Max: 1.6
d
ϵ = 0
Max: 4
Max: 2.6
Max: 2.1
C-TT
ϵ = 0.180
Max: 1.7
Max: 1.3
Max: 1.3
e
ϵ = 0
Max: 3.5
Max: 1.6
Max: 1.6
D-TT
ϵ = 0.114
Max: 1.8
Max: 1.3
Max: 1.2
0
1
2
3
m.r.d.

Figure 6: Stereographic pole figures showing the evolution of texture in austenite and martensite phases during compression at the indicated strain levels for: (a) A-IP, (b) A-TT, (c) B-TT, (d) C-TT, and (e) D-TT sample categories. For A-IP, the data from 2 mm slit is presented.

4 Discussion

In order to rationalize the evolution of strength of the HEA studied in this work, it is important to reflect on the thermodynamics of microstructure and phase evolution in the material. The metastable phase of austenite, γ, has an activation barrier for the diffusionless (no partitioning of elements) transformation to a stable phase ε at a given temperature and composition. The ε phase is stable in the Fe-Mn-Co-Cr HEA system at room temperature. The change in Gibb's free energy or the driving force for $\gamma \rightarrow \varepsilon$ transformation ($\Delta G^{\gamma \rightarrow \varepsilon}$ in J/mol) is related to the change in entropy ($\Delta S_{config}^{\gamma \rightarrow \varepsilon}$) using $\Delta G^{\gamma \rightarrow \varepsilon} = \Delta H_{mix}^{\gamma \rightarrow \varepsilon} - T\Delta S_{config}^{\gamma \rightarrow \varepsilon}$ [39]. Here, the $\Delta H_{mix}^{\gamma \rightarrow \varepsilon}$ is the enthalpy of mixing effect on the transformation kinetics and T is the temperature in K. The metastability of γ for $\gamma \rightarrow \varepsilon$ transformation is increased by adding the ε phase stabilizers, Co and Si, which increase $\Delta S_{config}^{\gamma \rightarrow \varepsilon}$ and is in the core of high entropy approach. These not only increase $\Delta S_{config}^{\gamma \rightarrow \varepsilon}$ to increase the metastability of γ for easy $\gamma \rightarrow \varepsilon$ transformation but also lower the SFE of the material. As already mentioned, if SFE is sufficiently low, formation of ε-martensite is favored. Microstructural defects introduced by plasticity such as slip bands are necessary for strain-induced transformation [50, 51]. Under the action of a local stress field separation between partials increases to form a slip band. Such bands usually include multiple dislocations on nearby $\{111\}_\gamma$ planes. These partial dislocations on neighboring $\{111\}_\gamma$ planes are boundaries of a thick fault [52]. If dislocations are positioned at every 2nd $\{111\}_\gamma$ plane in a slip band in γ, the band has HCP structure, which is ε. In contrast, if dislocations are positioned at every $\{111\}_\gamma$ plane in a slip band in γ, the band has FCC structure, which is a twin. Whether ε or twin formation within a slip band is favored depends on the SFE. A higher value of SFE favors formation of twins. The intrinsic SFE (γ_{SFE}) is directly related to $\Delta G^{\gamma \rightarrow \varepsilon}$ using $\gamma_{SFE} = n\rho\Delta G^{\gamma \rightarrow \varepsilon} + n\sigma^{\gamma/\varepsilon}$ [39], where, $\sigma^{\gamma/\varepsilon}$ is the interfacial energy between γ and ε phases, ρ is the planar density of closed packed {111} planes, and n is the thickness of an HCP embryo. The interfacial energy barrier for ε phase formation is low because of coherency.

Lowering the γ_{SFE}, the stress required for the dissociation of perfect dislocations into partials in the γ matrix to form stable intrinsic stacking faults also decreases.

However, keeping the composition, i.e. $\Delta S_{config}^{\gamma\rightarrow\varepsilon}$ constant, $\Delta G^{\gamma\rightarrow\varepsilon}$ can be changed using material's stored energy (accumulated strain level), which is embedded in the $\Delta H_{mix}^{\gamma\rightarrow\varepsilon}$ term. Therefore, the enthalpy term varies with prior processing [53]. The last effect to $\Delta G^{\gamma\rightarrow\varepsilon}$ comes from the temperature. In our work, the FSP conditions govern these strain and temperature effects on the transformation kinetics [39]. In summary, accommodated strain and temperature increase are competing effects promoting ε and γ, respectively. The added effects come from size and geometry of grains and dislocation structures. Given the two tool rotation rates explored in the present work, we define two scenarios. In the *scenario 1*, the tool rotation rate is 350 RPM and a higher temperature develops. The FSP substantially refines grains with some recovery, dynamic recrystallization, and grain growth taking place [30].

In the *scenario 2*, the tool rotation rate is 150 RPM and a higher stored energy accumulates in the material because of the lower temperature than at 350 RPM. Note that both tool rotation rates take the material into the γ phase to sufficiently soften the material for FSP, but the 350 RPM rate induces a higher temperature (~900^0C) than the 150 RPM FSP (~700^0C). As a result of lower temperature in FSP at 150 RPM, the material is less recovered and accumulates higher dislocation density and underlying stored energy, which in turn reduces the barrier to $\gamma\rightarrow\varepsilon$ transformation. The high stored energy state of the material corresponds to the high enthalpy state. We emphasize that different processing conditions leave γ in different states of enthalpy, while the entropy remains same as the solid solution configuration remains the same. As a result, the ε phase is thermodynamically more present and stable at room temperature upon FSP at 150 RPM than upon FSP at 350 RPM. In summary, as the strain rate, strain, and temperature depending on the tool rate at which the material is processed change, stored dislocation density changes in the microstructure at high temperature. This initial high temperature structure influences microstructure formation during cooling from γ to room temperature ($\gamma + \varepsilon + \sigma$).

The phases are determined by NeD and EBSD and also verified by optical microscopy (see appendix) in the materials before performing compression and during compression. Consistent with the above discussion, the fraction of phases is evidently a strong function of processing

history. The as-rolled material (A) microstructure contains a small amount of ε phase fraction (~0.12), a higher amount of σ-phase fraction (~0.21), and the highest amount of γ phase fraction (~0.66). The material exhibits a great deal of true strain before fracture with more in the IP than in the TT direction. While the phase fractions at fracture appear similar, the transformation rates are different. The $\gamma \rightarrow \varepsilon$ transformation rate in the TT is greater than in the IP during compression. We attribute this difference in the transformation rate as a function of compression direction to texture.

The strain-induced transformation is strongly affected by texture, i.e. by individual crystal orientation of grains undergoing the transformation [54-59]. In general, soft grains have a higher tendency to transform. In tension, grains with <011> and <111> parallel to a tensile direction form slip bands of ε, while grains with <001> parallel to tensile direction do not produce slip bands [55] because partial dislocations do not have sufficient driving force to produce wide stacking faults [58]. The effect of crystal orientation on the transformation kinetics in compression is reversed. Crystals with the <001> orientation parallel to a compression direction easily transform [57], the crystals compressed along <011> or <011> cannot transform under compression [55]. Inverse pole figures (IPFs) showing the local crystal orientations in the samples relative to the compression direction are provided in the appendix for easier recognition of the texture effects on the transformation in addition to the pole figures. Comparing the IPFs of the A category samples deformed in the IP direction versus in the TT direction reveals a higher number of crystals with the <001> direction parallel to the compression direction in the TT sample. These texture effects on the rate of transformation likely play a role for compressive strain at fracture. The IP samples deforming at a lower transformation rate accumulate more strain before fracture.

To better observe the strain induced phase transformation, a high resolution EBSD map is provided in Fig. 7 for an A sample at a compressive strain of $\epsilon = 0.198$. This meso-scale data is used to verify the macroscopic NeD measurements and evaluate occurrence of any deformation twinning in the structure. Slip bands of the γ as sheaves of fine parallel laths strung out on the $\{111\}_\gamma$ planes of the γ phase carry out the strain-induced ε martensite formation while accommodating plastic strain. The ε-martensite phase was not observed to further transform to α'-martensite. The fraction of the diffusion created σ phase during processing does not change during compression at room temperature meaning that the σ phase can only stably form in DP-5Si-HEA during cooling from high temperature and not because of mechanical straining. The Kernel average

misorientation (KAM) map shows a higher presence of geometrically necessary dislocations (GNDs) in the highly dislocated ε phase upon TRIP than in the γ phase. The ε phase is thus harder contributing to the overall hardening of the material, in addition to the dynamic Hall-Petch-type hardening as a consequence of more interfaces in the microstructure forming barriers to mobile dislocations. Therefore, the material exhibits a great deal of strain hardening during compression.

FSP of the as-rolled material increases the strength, which is attributed to the microstructural changes as described above. The B category samples underwent FSP at 350 RPM, the processing condition of higher strain rate and temperature, and a faster cooling rate after the processing relative to FSP at 150 RPM. Because the temperature has dominated over the strain at 350 RPM (the scenario 1), the fraction of γ even increased (~0.81) at the expense of ε (0.067) and σ (0.12) relative to the initial A category material. However, the average grain size substantially decreased to 4 μm after the processing. As a result of fine grain size, the B material is stronger than the A material even though it has less of harder ε and σ phases. The low fraction of the σ phase is due to the fast cooling rate preventing the diffusion driven precipitation of the phase in the microstructure [40]. The low fraction of the ε phase is due to the high temperature conditions governing a low dislocation density driven stored energy. Moreover, the material B exhibits even more rapid hardening than the material A, which is attributed to a greater transformation rate from a very large fraction of γ phase. Although the higher rate of transformation is associated primarily to the initially large fraction of deforming γ, grain size may play a secondary role. As grain boundaries act as nucleation sites for ε, back-stress fields and higher stability of grain boundaries hinders the growth of ε [26, 60, 61]. We observe that ε phase starts from grain boundaries at the provided maps in the appendix for B-TT-0.296 sample. No deformation twins are observed in this map as well. The IPF from the appendix shows that γ phase crystal orientations have sufficient preferential orientation for transformation, although the intensity of them is lower than the A category. The rate of TRIP is likely higher in the IP than in the TT sample.

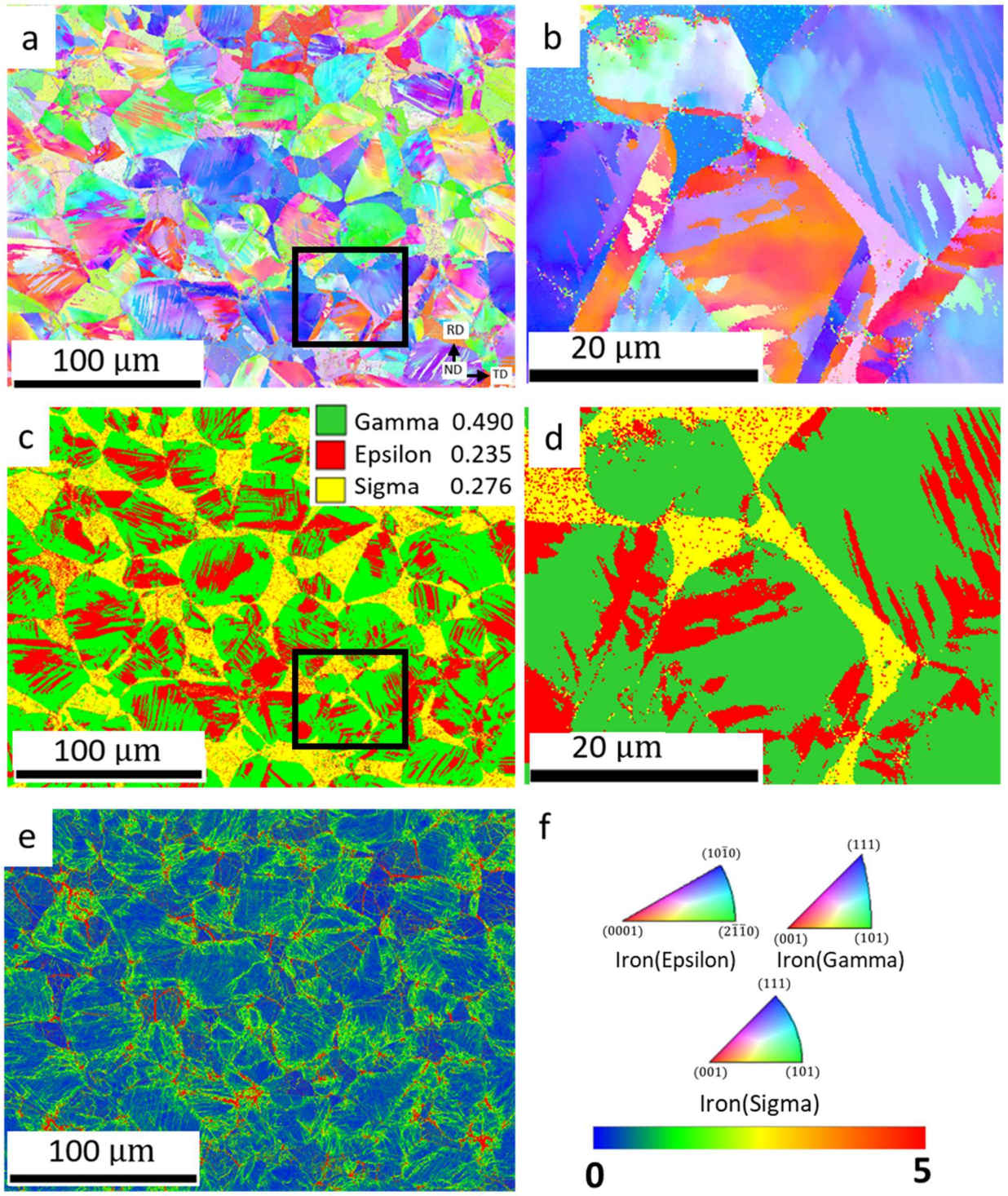

Figure 6: (a, b) IPF, (c, d) phase, and (e) KAM maps obtained by EBSD for the A-TT-0.198 sample. (b, d) are zoom ins. Perpendicular to the IPF map is the ND, which is also the compression

loading direction. (f) ND standard IPF triangles for Iron (γ), Iron (ε) and Iron (σ) phases and the intensity bar for the KAM map.

In contrast to A and B material categories, the C material category created by FSP at 150 RPM contains a much larger fraction of harder ε and σ phases (~0.42). The large fraction of ε in the microstructure before compression is a consequence of high stored energy induced during FSP (the scenario 2). The higher σ-phase in C compared to the B category specimens could be because of the operation of FSP at ~700^0C which is known to be the favorable σ-phase precipitation region [40]. The grain size is refined (2 μm) relative to the as-rolled material, A. Owing to the grain structure and phase content, the material is strong and still accumulates a decent amount of TRIP accommodated compressive strain and hardening. Peak broadening and micro-strain increase with plastic strain of the ε phase suggests that the phase is deforming, which contributes to the plasticity of the alloy. The C material category exhibits a lower rate of phase transformation than B, which is attributed to the lower content of γ and some strain accommodation by ε [26]. The IPFs provided in the appendix show some intensity around <001> direction, especially for the IP sample governing some anisotropy in strain hardening with more in IP than in TT.

The D category samples that underwent double pass (two consecutive FSP passes at 350 RPM followed by 150 RPM) are the strongest. The combined phase fraction of ε and σ in these samples is (~0.41), like in the C material category while the ε phase fraction decreased (~0.13). The presence of higher σ phase fraction can be a consequence of finer grain size after 350 RPM FSP than after as-rolled material providing much more nucleation sites at the grain boundary and favorable 700^0C during 150 RPM FSP processing. The average grain size is about 1 μm. As a result of phase fractions and grain size, the material is the strongest and reaches UTS of 1850 MPa. Furthermore, the IPF in the appendix shows some amount of γ favorably oriented for transformation. The TRIP effect has a slightly higher rate in D than the C material category, despite undergoing the same final FSP processing.

The evolution of texture in the γ phase due to compressive strain shows the formation of a typical $\{110\}$ fiber. After analyzing the texture components, it was observed that the brass, copper and Goss components predominate. On the other hand, the texture formation of the ε phase is primarily driven by the variant selection of the TRIP mechanism. The orientation relationship

between γ and ε is $\{111\}_\gamma \parallel \{0001\}_\varepsilon$, $\langle 110\rangle_\gamma \parallel \langle 2\bar{1}\bar{1}0\rangle_\varepsilon$ [62]. While ε phase is stronger than the γ phase, the strength differential is not such to prevent dislocation slip in the ε phase. Therefore, the phases are co-deforming and a minor contribution to texture evolution in the ε phase is due to slip in it. While twins are not observed by EBSD, existence of nano-twins in ε is not ruled out. However, existence of nano-twins would not appreciably influence the texture evolution but would influence strain hardening by restricting the slip length associated with slip. Finally, the texture analysis of the σ phase reveals a random texture throughout the compression deformation indicating that the phase likely does not deform. The texture may be slightly evolving only by the rigid rotation of the σ precipitations.

The intrinsic $\frac{c}{a}$ ratio in metals like Mg or Be or Ti alloys does not change during deformation. In a dual phase HEA ($Fe_{50}Mn_{30}Co_{10}Cr_{10}$), the $\frac{c}{a}$ ratio of 1.616 is reported in the literature [63]. As expected, changes in alloying change the $\frac{c}{a}$ ratio. The addition of Co, Mn and Si (HCP stabilizers) increases the lattice distortion and the $\frac{c}{a}$ ratio, while the addition of austenite stabilizers such as Cu or Al decreases the $\frac{c}{a}$ ratio. For all the cases, the $\frac{c}{a}$ ratio was lower than the ideal $\frac{c}{a}$ = 1.633. However, processing history of such HEA can change the $\frac{c}{a}$ ratio. For CS-HEA, the ratio decreases from as-cast 1.6254 to FSP 1.615 and further to ~1.598 for samples fractured in tension [64]. The present work observed similar changes in the $\frac{c}{a}$ ratio for $Fe_{42}Mn_{28}Co_{10}Cr_{15}Si_5$ HEA. While the actual origin of lattice parameter changes with plasticity is not known, these changes in $\frac{c}{a}$ for ε-martensite have been attributed to the volume reduction (~1.6%) that occurs during $\gamma \rightarrow \varepsilon$ transformation and underlying shear as well as shuffle along the habit plane for **a**-axis and perpendicular to the plane for **c**-axis [64]. The change in $\frac{c}{a}$ is likely increasing the ductility by shifting relative activity of slip systems since in HCP metals $\frac{c}{a}$ ratio influences the selection of mode of deformation accommodating an applied plastic strain: basal <**a**>, prismatic <**a**>, and pyramidal <**c**+**a**> slip or twinning. HCP metals with lower than the ideal ratio have a higher probability for activating <**c**+**a**> slip systems, which given their multiplicity improve ductility. Given the low $\frac{c}{a}$ ratio of ε, <**c**+**a**> slip operates in the alloy as observed in [26, 64].

In closing, to verify the formation of σ phase, we show a secondary electron (SE) SEM micrograph along with energy-dispersive X-ray spectroscopy (EDS) elemental maps of the same area for an A-TT initial sample in Fig. 8. Given the composition of the alloy, the cooling rates during processing were such that the kinetics of σ diffusion transformation was operating in the 600 ˚ – 1000 ˚C temperature range. The kinetics during cooling in FSP also created the σ-phase but the structure was much finer than upon rolling. As discussed earlier, the σ phase is an intermetallic forming at the Cr rich regions. Figs. 8b and c verify the high Si and Cr at the σ-phase region. Additionally, the spot analysis validates higher Cr and Si at% in the sigma phase (Table 3). Interestingly, some untransformed γ phases is present as colonies of small particles in the σ-phase. A high resolution EBSD map verifying the untransformed γ phase in σ is presented in the appendix.

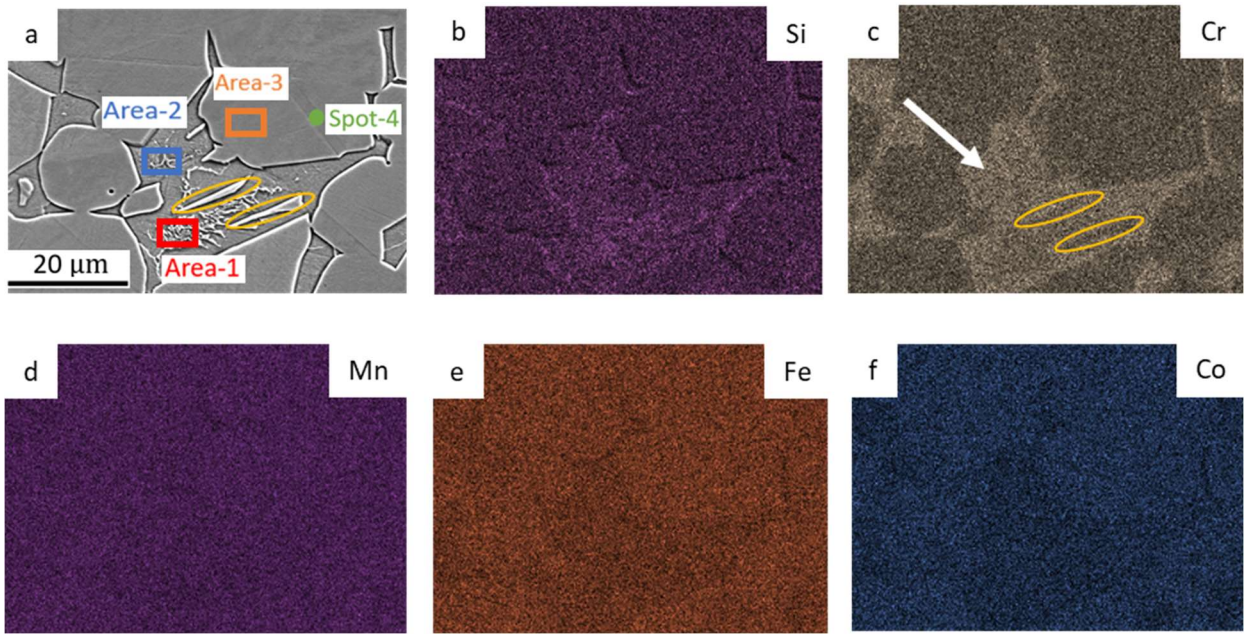

Figure 7: SEM-SE micrograph of A-TT category (a). The composition maps of (b) Si, (c) Cr, (d) Mn, (e) Fe, and (f) Co. The composition map shows a higher Cr in σ-phase (denoted with the white arrow). Yellow ellipses in (a) and (c) show low Cr phases inside a higher Cr zone. These were identified as γ phases using EBSD.

Table 3: EDS measured composition at the marked regions and points in Fig. 8a. EDS over very large area recovers accurately the nominal composition.

	Position	Si (at%)	Cr (at%)	Mn (at%)	Fe (at%)	Co (at%)
A-TT-initial	Area-1	4.97	17.78	27.85	41.72	7.69
	Area-2	3.84	19.80	28.11	40.65	7.60
	Area-3	3.21	14.17	29.95	43.22	9.46
	Spot-4	3.25	14.57	29.89	42.96	9.33
	Nominal	5.00	15.00	28.00	42.00	10.00

5 Conclusions

In this study, strength and microstructure evolution of a very low SFE $Fe_{42}Mn_{28}Co_{10}Cr_{15}Si_5$ (in at%) HEA were investigated. The primarily focus was on the evolution during compression of the initial microstructures created by rolling and FSP. The initial microstructures had triplex structure consisting of metastable γ, stable σ, and stable ε phases in different ratios and various grain sizes depending on the processing. FSP at 350 RPM slightly increased the γ phase content to that created by rolling but substantially refined grains. In contrast, the FSP at 150 RPM increased the fraction of ε phase along with refining the grain structure. Finally, the FSP with 350 RPM followed by 150 RPM significantly refined the structure and also increased fraction of the σ phase. The tremendous microstructural flexibility exhibited by the alloy facilitates a creation of the material with 1850 MPa UTS. In the core of the flexibility is the transformation facilitated plastic strain accommodation and underlying strain hardening. The hardening is a consequence of the increased fraction of the highly dislocated ε phase fraction and transformation induced dynamic

Hall-Petch-type barrier effect. Strain to fracture of the material is greater with a larger amount of the γ phase and a slower rate of TRIP. The rate of TRIP was found to increase with the initial content on γ and favorable texture i.e. more grains with the <001> orientation parallel to a compression direction. Texture of γ phase exhibits strengthening of $\{110\}$ fiber along the compression direction, while the texture formation of the ε phase is primarily driven by the variant selection of the TRIP mechanism. Given the measured low $\frac{c}{a}$ ratio of ε with a decreasing trend with plastic strain, the activation of non-basal slip systems contributing to the ductility of the alloy is promoted. Therefore, some texture evolution in ε is due to slip as the phases are co-deforming. The texture analysis of the σ phase reveals a random texture throughout the compression deformation, which means that the phase likely does not deform but only floats in the matrix.

Acknowledgements

This research was sponsored by the U.S. Army Research Laboratory under the W911NF-15-2-0084 cooperative agreement and the U.S. National Science Foundation under the OIA-1757371 grant.

Appendix

This appendix presents optical microscopy images corresponding to Fig. 3 in Fig. A1, inverse pole figures (IPFs) showing the initial texture in the samples in Fig. A2, deformed structure of B-TT sample at 0.296 strain in Fig. A3, zoom in SEM secondary electrons (SE) image of A-TT-initial sample revealing phases in Fig. A4. Table A1 shows a comparison of measured phase fractions data using three different methods.

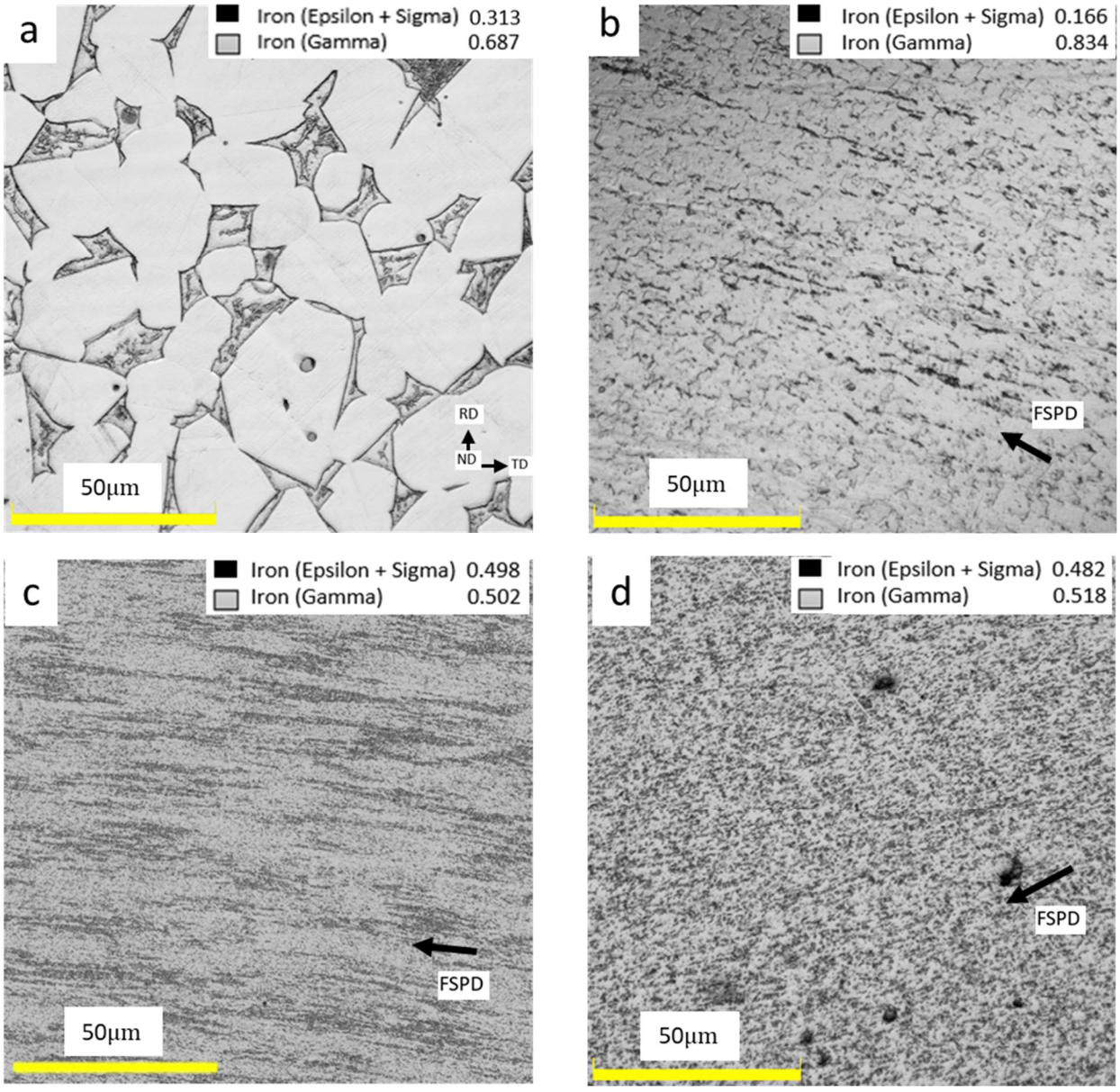

Figure A1: Optical microscopy images for the following samples: (a) A-TT-initial (as rolled), (b) B-TT-initial (FSP at a tool speed of 350 rpm), (c) C-TT-initial (FSP at a tool speed of 150 rpm), and (d) D-TT-initial (FSP with two consecutive runs at tool speeds of 350 RPM and 150 RPM, respectively). Image thresholding in MATLAB is used to obtain the phase fractions. The reported fraction values are averaged over at least 3 images per sample category. The white regions are gamma phase, while the black areas are epsilon and sigma phases.

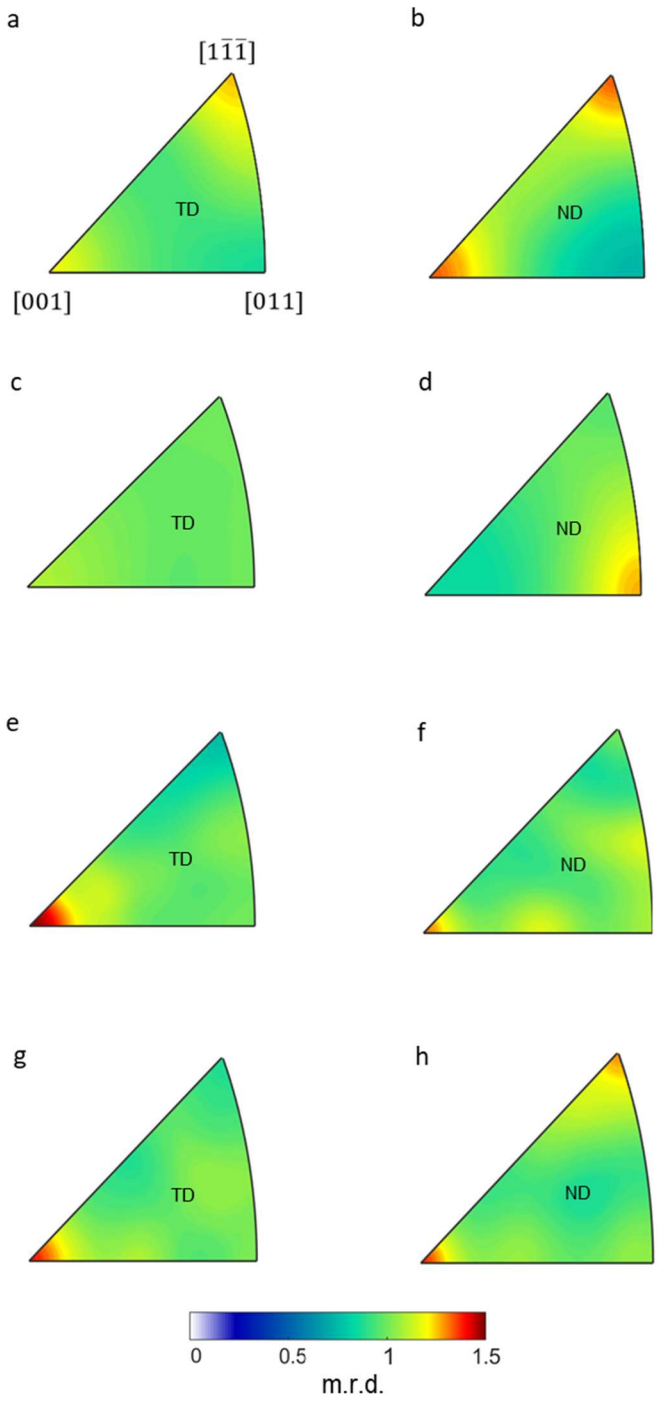

Figure A2: Inverse pole figures (IPFs) showing texture relative to the loading direction in: (a) A-IP, (b) A-TT, (c) B-IP, (d) B-TT, (e) C-IP (f) C-TT, (g) D-IP, and (h) D-TT samples.

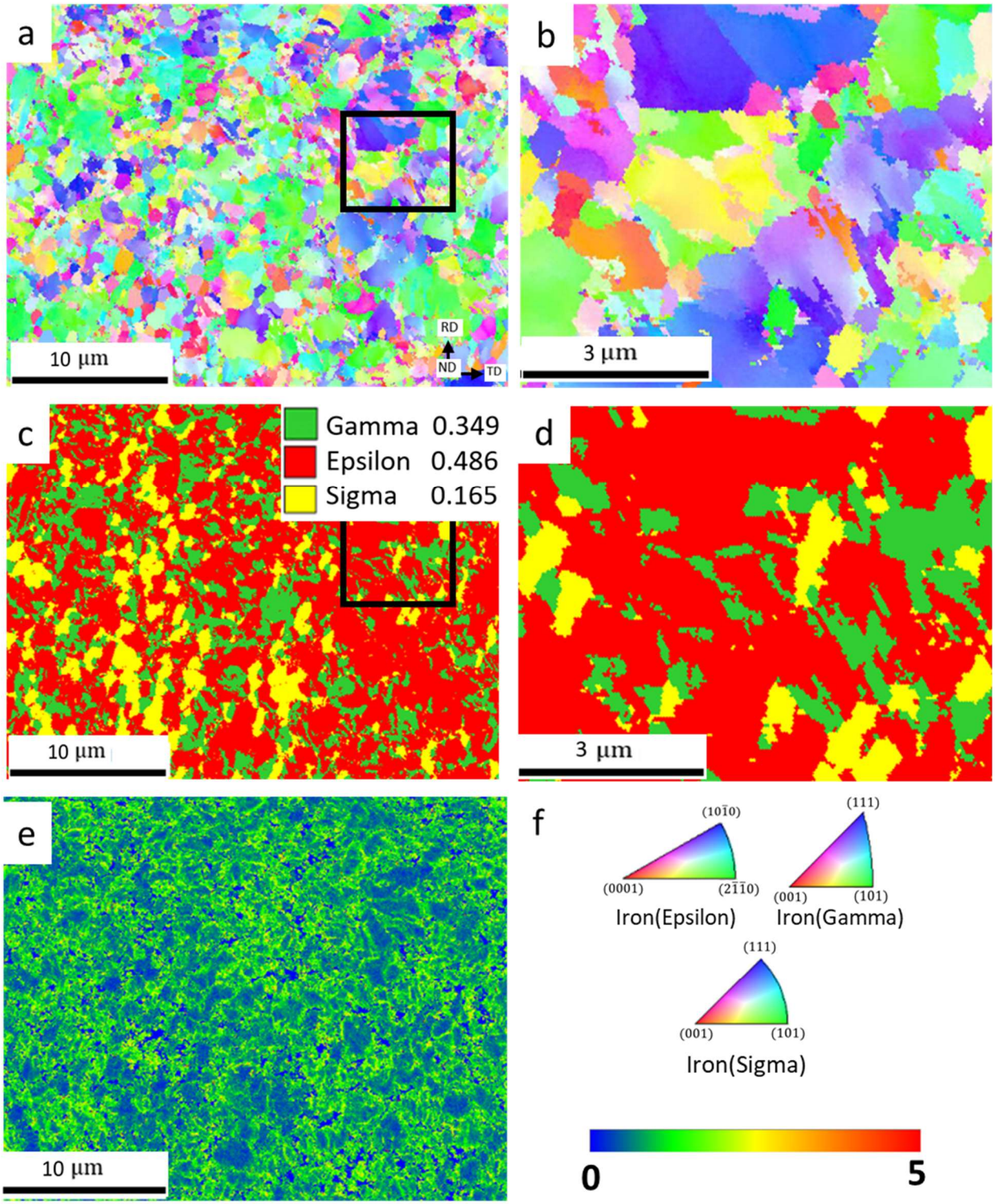

Figure A3: (a,b) IPF, (c,d) phase, and (e) KAM maps obtained by EBSD for a B-TT-0.296 sample. (b,d) are zoom ins. Although the red and yellow color represent the epsilon and sigma phase respectively (c,d), their fraction was not reported because of the low confidence index. Perpendicular to the maps is the sample ND, which is also the compression direction. (f) ND

standard IPF triangles for Iron (γ), Iron (ε) and Iron (σ) phases and the intensity bar for the KAM map.

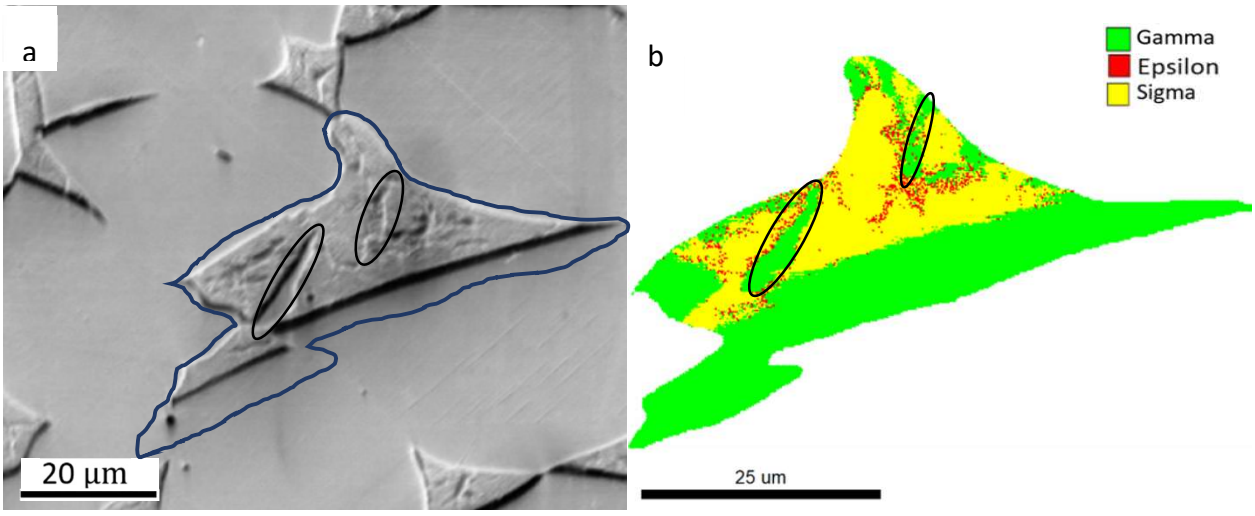

Figure A4: (a) SEM–SE micrograph for A-TT-initial sample at 70^0 tilt. (b) The corresponding EBSD phase map for the selected area surrounded by the blue color. The black ellipses show γ phase inside σ phase.

Table A1: Measured phase fractions data using three different methods.

	NeD			Optical images thresholding		EBSD		
	Gamma	Epsilon	Sigma	Gamma	Epsilon + Sigma	Gamma	Epsilon	Sigma
D-TT-initial-0.0	0.583	0.131	0.286	0.542	0.458	0.571	0.122	0.307
C-TT-initial-0.0	0.579	0.224	0.197	0.515	0.485	0.542	0.229	0.229
B-TT-initial-0.0	0.814	0.067	0.118	0.759	0.241	0.723	0.138	0.139

B-TT-0.070	0.660	0.221	0.118	-----	-----	-----		
B-TT-0.130	0.610	0.271	0.118	-----	-----	-----		
B-TT-frac-0.296	0.482	0.384	0.118	0.366	0.636	0.349	0.486	0.165
D-TT-frac-0.114	0.487	0.227	0.286	0.484	0.516	-----		
C-TT-frac-0.18	0.469	0.331	0.197	0.495	0.505	-----		
A-TT-initial-0.0 (A-IP-initial-no-slit)	0.663	0.119	0.218	0.687	0.313	0.653	0.139	0.208
A-TT-0.085	0.634	0.148	0.218	------	------	------		
A-TT-0.198	0.522	0.260	0.218	------	------	0.49	0.235	0.275
A-TT-frac-0.454	0.306	0.476	0.218	0.315	0.685	------		
A-IP-0.098 (no slit)	0.528	0.254	0.218	------	------	------		
A-IP-0.215 (no slit)	0.476	0.306	0.218	------	------	------		
A-IP-frac-0.669 (no slit)	0.333	0.449	0.218	------	------	------		

A-IP-initial-0.0 (2mm slit)	0.670	0.119	0.211	------	------	------
A-IP-0.098 (2mm slit)	0.575	0.214	0.211	------	------	------
A-IP-0.215 (2mm slit)	0.510	0.278	0.211	------	------	------
A-IP-frac-0.669 (2mm slit)	0.325	0.464	0.211	------	------	------

References

[1] P. Akerfeldt, Antti, M. L., Pederson, R., Influence of microsructure on mechanical properties of laser metal wire-deposited Ti-6Al-4V, Materials Science and Engineering: A 674 (2016) 428-437.

[2] D.W. Brown, Adams, D. P., Balogh, L., Carpenter, J. S., Clausen, B., King, G., Reedlunn, B., Palmer, T. A., Maguire, M. C., Vogel, S. C., In situ neutron diffraction study of the influence of microstructure on the mechanical response of additively manufactured 304L stainless steel, Metallurgical and Materials Transactions A 48(12) (2017) 6055-6069.

[3] B.E. Carroll, Palmer, T. A., Beese, A. M., Anisotropic tensile behavior of Ti-6Al-4V components fabricated with directed energy deposition additive manufacturing, Acta Materialia 87 (2015) 309-320.

[4] N.C. Ferreri, Ghorbanpour, S., Bhowmik, S., Lussier, R., Bicknell, J., Patterson, B. M., Knezevic, M., Effects of build orientation and heat treatment on the evolution of microstructure and mechanical properties of alloy Mar-M-509 fabricated via laser powder bed fusion, International Journal of Plasticity 121 (2019) 116-133.

[5] S. Gribbin, Ghorbanpour, S., Ferreri, N. C., Bicknell, J., Tsukrov, I., Knezevic, M., Role of grain structure, grain boundaries, crystallographic texture, precipitates, and porosity on fatigue behavior of Inconel 718 at room temperature and elevated temperatures, Mater Charact 149 (2018) 184-197.

[6] Z. Wang, Palmer, T. A., Beese, A. M., Effect of processing parameters on microstructure and tensile properties of austenitic stainless steel 304L made by directed energy deposition additive manufacturing, Acta Materialia 110 (2016) 226-235.

[7] S. Gribbin, J. Bicknell, L. Jorgensen, I. Tsukrov, M. Knezevic, Low cycle fatigue behavior of direct metal laser sintered Inconel alloy 718, Int J Fatigue 93 (2016) 156-167.

[8] D.H. Smith, J. Bicknell, L. Jorgensen, B.M. Patterson, N.L. Cordes, I. Tsukrov, M. Knezevic, Microstructure and mechanical behavior of direct metal laser sintered Inconel alloy 718, Materials Characterization 113 (2016) 1-9.

[9] B. Cantor, Multicomponent and high entropy alloys, Entropy 16(9) (2014) 4749-4768.

[10] J.W. Yeh, S.K. Chen, S.J. Lin, J.Y. Gan, T.S. Chin, T.T. Shun, C.H. Tsau, S.Y. Chang, Nanostructured high-entropy alloys with multiple principal elements: novel alloy design concepts and outcomes, Advanced Engineering Materials 6(5) (2004) 299-303.

[11] Z. Li, K.G. Pradeep, Y. Deng, D. Raabe, C.C. Tasan, Metastable high-entropy dual-phase alloys overcome the strength–ductility trade-off, Nature 534(7606) (2016) 227-230.

[12] Z. Li, C.C. Tasan, K.G. Pradeep, D. Raabe, A TRIP-assisted dual-phase high-entropy alloy: grain size and phase fraction effects on deformation behavior, Acta Materialia 131 (2017) 323-335.

[13] Y. Deng, C.C. Tasan, K.G. Pradeep, H. Springer, A. Kostka, D. Raabe, Design of a twinning-induced plasticity high entropy alloy, Acta Materialia 94 (2015) 124-133.

[14] Z. Li, D. Raabe, Strong and ductile non-equiatomic high-entropy alloys: design, processing, microstructure, and mechanical properties, Jom 69(11) (2017) 2099-2106.

[15] M.J. Yao, K.G. Pradeep, C.C. Tasan, D. Raabe, A novel, single phase, non-equiatomic FeMnNiCoCr high-entropy alloy with exceptional phase stability and tensile ductility, Scripta Materialia 72-73 (2014) 5-8.

[16] B. He, B. Hu, H. Yen, G. Cheng, Z. Wang, H. Luo, M. Huang, High dislocation density–induced large ductility in deformed and partitioned steels, Science 357(6355) (2017) 1029-1032.

[17] S.S. Nene, M. Frank, K. Liu, S. Sinha, R.S. Mishra, B. McWilliams, K.C. Cho, Reversed strength-ductility relationship in microstructurally flexible high entropy alloy, Scr. Mater. 154 (2018) 163-167.

[18] Z. Feng, M. Zecevic, M. Knezevic, Stress-assisted ($\gamma \rightarrow \alpha'$) and strain-induced ($\gamma \rightarrow \varepsilon \rightarrow \alpha'$) phase transformation kinetics laws implemented in a crystal plasticity model for predicting strain path sensitive deformation of austenitic steels, Int. J. Plast. 136 (2021) 102807.

[19] B.C. De Cooman, Y. Estrin, S.K. Kim, Twinning-induced plasticity (TWIP) steels, Acta Materialia 142 (2018) 283-362.

[20] S.S. Nene, K. Liu, M. Frank, R.S. Mishra, R.E. Brennan, K.C. Cho, Z. Li, D. Raabe, Enhanced strength and ductility in a friction stir processing engineered dual phase high entropy alloy, Scientific reports 7(1) (2017) 1-7.

[21] R. Xiong, H. Peng, S. Wang, H. Si, Y. Wen, Effect of stacking fault energy on work hardening behaviors in Fe–Mn–Si–C high manganese steels by varying silicon and carbon contents, Materials & Design 85 (2015) 707-714.

[22] E. Galindo-Nava, P. Rivera-Díaz-del-Castillo, Understanding martensite and twin formation in austenitic steels: A model describing TRIP and TWIP effects, Acta Materialia 128 (2017) 120-134.

[23] J.J. Jonas, C. Aranas Jr, S.F. Rodrigues, Dynamic transformation of austenite at temperatures above the Ae3, Materials Science Forum, Trans Tech Publ, 2018, pp. 633-638.

[24] R. Xiong, H. Peng, H. Si, W. Zhang, Y. Wen, Thermodynamic calculation of stacking fault energy of the Fe–Mn–Si–C high manganese steels, Materials Science and Engineering: A 598 (2014) 376-386.

[25] S.S. Nene, M. Frank, K. Liu, R.S. Mishra, B.A. McWilliams, K.C. Cho, Extremely high strength and work hardening ability in a metastable high entropy alloy, Scientific Reports 8(1) (2018) 9920.

[26] M. Frank, Y. Chen, S.S. Nene, S. Sinha, K. Liu, K. An, R.S. Mishra, Investigating the deformation mechanisms of a highly metastable high entropy alloy using in-situ neutron diffraction, Materials Today Communications 23 (2020) 100858.

[27] A. Heczel, M. Kawasaki, J.L. Lábár, J.-i. Jang, T.G. Langdon, J. Gubicza, Defect structure and hardness in nanocrystalline CoCrFeMnNi high-entropy alloy processed by high-pressure torsion, Journal of Alloys and Compounds 711 (2017) 143-154.

[28] V.H. Hammond, M.A. Atwater, K.A. Darling, H.Q. Nguyen, L.J. Kecskes, Equal-channel angular extrusion of a low-density high-entropy alloy produced by high-energy cryogenic mechanical alloying, Jom 66(10) (2014) 2021-2029.

[29] N. Kumar, M. Komarasamy, P. Nelaturu, Z. Tang, P. Liaw, R. Mishra, Friction stir processing of a high entropy alloy Al 0.1 CoCrFeNi, Jom 67(5) (2015) 1007-1013.

[30] S. Palanivel, A. Arora, K. Doherty, R. Mishra, A framework for shear driven dissolution of thermally stable particles during friction stir welding and processing, Materials Science and Engineering: A 678 (2016) 308-314.

[31] R.Z. Valiev, T.G. Langdon, Principles of equal-channel angular pressing as a processing tool for grain refinement, Progress in materials science 51(7) (2006) 881-981.

[32] A.P. Zhilyaev, T.G. Langdon, Using high-pressure torsion for metal processing: Fundamentals and applications, Progress in Materials science 53(6) (2008) 893-979.

[33] S. Nene, M. Frank, K. Liu, S. Sinha, R. Mishra, B. McWilliams, K. Cho, Reversed strength-ductility relationship in microstructurally flexible high entropy alloy, Scripta Materialia 154 (2018) 163-167.

[34] P. Agrawal, S. Shukla, S. Gupta, P. Agrawal, R.S. Mishra, Friction stir gradient alloying: A high-throughput method to explore the influence of V in enabling HCP to BCC transformation in a γ-FCC dominated high entropy alloy, Applied Materials Today 21 (2020) 100853.

[35] H.-R. Wenk, L. Lutterotti, S. Vogel, Texture analysis with the new HIPPO TOF diffractometer, Nuclear Instruments and Methods in Physics Research Section A: Accelerators, Spectrometers, Detectors and Associated Equipment 515(3) (2003) 575-588.

[36] H.-R. Wenk, L. Lutterotti, S. Vogel, Rietveld texture analysis from TOF neutron diffraction data, Powder diffraction 25(3) (2010) 283-296.

[37] C.-C. Hsieh, W. Wu, Overview of intermetallic sigma (?) phase precipitation in stainless steels, International Scholarly Research Notices 2012 (2012).

[38] T. Liang, X.Q. Hu, X.H. Kang, D.Z. Li, Effect of the sigma phase on the mechanical properties of a cast duplex stainless steel during the ageing treatment at 850° C, Advanced Materials Research, Trans Tech Publ, 2013, pp. 325-329.

[39] S. Nene, M. Frank, P. Agrawal, S. Sinha, K. Liu, S. Shukla, R. Mishra, B. McWilliams, K. Cho, Microstructurally flexible high entropy alloys: Linkages between alloy design and deformation behavior, Materials & Design 194 (2020) 108968.

[40] S. Nene, K. Liu, S. Sinha, M. Frank, S. Williams, R. Mishra, Superplasticity in fine grained dual phase high entropy alloy, Materialia 9 (2020) 100521.

[41] N.C. Ferreri, S.C. Vogel, M. Knezevic, Determining volume fractions of γ, γ′, γ ″, δ, and MC-carbide phases in Inconel 718 as a function of its processing history using an advanced neutron diffraction procedure, Materials Science and Engineering: A 781 (2020) 139228.

[42] S. Takajo, S.C. Vogel, Determination of pole figure coverage for texture measurements with neutron time-of-flight diffractometers, Journal of Applied Crystallography 51(3) (2018) 895-900.

[43] L.-M. Peng, G. Ren, S. Dudarev, M. Whelan, Debye–Waller factors and absorptive scattering factors of elemental crystals, Acta Crystallographica Section A: Foundations of Crystallography 52(3) (1996) 456-470.

[44] R.E. Smallman, K.H. Westmacott, Stacking faults in face-centred cubic metals and alloys, Philosophical magazine 2(17) (1957) 669-683.

[45] J. Häglund, A. Fernández Guillermet, G. Grimvall, M. Körling, Theory of bonding in transition-metal carbides and nitrides, Physical Review B 48(16) (1993) 11685-11691.

[46] L.S. Dubrovinsky, P. Lazor, S.K. Saxena, P. Häggkvist, H.-P. Weber, T. Le Bihan, D. Hausermann, Study of laser heated iron using third generation synchrotron X-ray radiation facility with imaging plate at high pressures, Physics and Chemistry of Minerals 26 (1999) 539.

[47] G. Bergman, D.P. Shoemaker, The determination of the crystal structure of the [sigma] phase in the iron-chromium and iron-molybdenum systems, Acta Crystallographica 7(12) (1954) 857-865.

[48] X.-L. Wang, Y. Wang, J. Richardson, Experimental error caused by sample displacement in time-of-flight neutron diffractometry, Journal of applied crystallography 35(5) (2002) 533-537.

[49] I.C. Noyan, J.R. Bunn, M. Tippett, E. Payzant, B. Clausen, D.W. Brown, Experimental determination of precision, resolution, accuracy and trueness of time-of-flight neutron diffraction strain measurements, Journal of Applied Crystallography 53(2) (2020) 494-511.

[50] G.B. Olson, M. Cohen, A mechanism for the strain-induced nucleation of martensitic transformations, Journal of the Less Common Metals 28(1) (1972) 107-118.

[51] G.B. Olson, M. Cohen, Kinetics of strain-induced martensitic nucleation, Metallurgical Transactions A 6(4) (1975) 791.

[52] G.B. Olson, M. Cohen, A general mechanism of martensitic nucleation: Part I. General concepts and the FCC→ HCP transformation, MTA 7(12) (1976) 1897-1904.

[53] R.S. Mishra, R.S. Haridas, P. Agrawal, High entropy alloys – Tunability of deformation mechanisms through integration of compositional and microstructural domains, Mater. Sci. Eng. A 812 (2021) 141085.

[54] W.G. Burgers, J.A. Klostermann, Influence of the direction of deformation on the transition of austenite into martensite, Acta Metallurgica 13(5) (1965) 568-572.

[55] D. Goodchild, W.T. Roberts, D.V. Wilson, Plastic deformation and phase transformation in textured austenitic stainless steel, Acta Metallurgica 18(11) (1970) 1137-1145.

[56] B. Petit, N. Gey, M. Cherkaoui, B. Bolle, M. Humbert, Deformation behavior and microstructure/texture evolution of an annealed 304 AISI stainless steel sheet. Experimental and micromechanical modeling, International Journal of Plasticity 23(2) (2007) 323-341.

[57] E. Polatidis, W.N. Hsu, M. Šmíd, T. Panzner, S. Chakrabarty, P. Pant, H. Van Swygenhoven, Suppressed martensitic transformation under biaxial loading in low stacking fault energy metastable austenitic steels, Scr. Mater. 147 (2018) 27-32.

[58] M. Zecevic, M.V. Upadhyay, E. Polatidis, T. Panzner, H. Van Swygenhoven, M. Knezevic, A crystallographic extension to the Olson-Cohen model for predicting strain path dependence of martensitic transformation, Acta. Mater. 166 (2019) 386-401.

[59] R. Lagneborgj, The martensite transformation in 18% Cr-8% Ni steels, Acta Metall. 12(7) (1964) 823-843.

[60] M. Wang, Z. Li, D. Raabe, In-situ SEM observation of phase transformation and twinning mechanisms in an interstitial high-entropy alloy, Acta Materialia 147 (2018) 236-246.

[61] R.S. Mishra, S.S. Nene, M. Frank, S. Sinha, K. Liu, S. Shukla, Metastability driven hierarchical microstructural engineering: Overview of mechanical properties of metastable complex concentrated alloys, Journal of Alloys and Compounds 842 (2020) 155625.

[62] L. Bracke, L. Kestens, J. Penning, Transformation mechanism of α′-martensite in an austenitic Fe–Mn–C–N alloy, Scripta Materialia 57(5) (2007) 385-388.

[63] Y. Bu, Z. Li, J. Liu, H. Wang, D. Raabe, W. Yang, Nonbasal Slip Systems Enable a Strong and Ductile Hexagonal-Close-Packed High-Entropy Phase, Physical Review Letters 122(7) (2019) 075502.

[64] S. Sinha, S.S. Nene, M. Frank, K. Liu, P. Agrawal, R.S. Mishra, On the evolving nature of c/a ratio in a hexagonal close-packed epsilon martensite phase in transformative high entropy alloys, Scientific Reports 9(1) (2019) 13185.

CHAPTER 2:

Effect of powder reuse on tensile, compressive and creep strength of Inconel 718 fabricated via laser powder bed fusion

This chapter will be submitted to Additive Manufacturing as: "Effect of powder reuse on tensile, compressive and creep strength of Inconel 718 fabricated via laser powder bed fusion," Shubhrodev Bhowmik, Brandon A. McWilliams, Marko Knezevic.

In this work, I performed all the room temperature compression and creep tests. I also performed electron backscatter diffraction (EBSD) for microstructural characterization. I carried out analysis of data from both characterization and mechanical testing. The text was written under the guidance of Dr. Marko Knezevic and other co-authors.

Effect of powder reuse on tensile, compressive and creep strength of Inconel 718 fabricated via laser powder bed fusion

Shubhrodev Bhowmik[a], Brandon A. McWilliams[b], Marko Knezevic[a,†]

[a]Department of Mechanical Engineering, University of New Hampshire, Durham, NH, 03824, USA

[b]Weapons and Materials Research Directorate, DEVCOM Army Research Laboratory, Aberdeen Proving Ground, MD, 21005, USA.

Abstract

This work is concerned with determining the effect powder reusing has on tensile, compressive and creep strength of Inconel 718 fabricated via laser powder bed fusion (LPBF). Test specimens are machined from rods fabricated by LPBF using virgin powder and powder that had been used in the process for some period of time. The rods were treated by hot isostatic pressing (HIP) and then heat treated as per AMS 2774. While grain structure and texture are not appreciably different in the samples made from virgin versus reused powder, dislocation density and dispersion strengthening are estimated higher in the samples made from reused than virgin powder due to multiple heating cycles experienced by reused powder. As a result, samples made from reused powder are stronger in tension and compression. Moreover, the distribution of solute atoms is such that the samples made from reused powder exhibit serrated yielding at higher temperatures. The creep strength is higher for the samples made from virgin powder up to 650^0C but not at 700^0 C. These results are rationalized based on the dislocation density, dispersion hardening and underlying diffusion governing solute distribution and precipitates in the materials. The creep parameters were estimated using the measured data and then refined by a subsequent data fitting using the Mukherjee – Bird – Dorn equation. The quality of fits and established parameters for the creep behavior for the two material categories are presented and discussed.

* Corresponding author at: University of New Hampshire, Department of Mechanical Engineering, 33 Academic Way, Kingsbury Hall, W119, Durham, New Hampshire 03824, United States.

E-*mail address*: marko.knezevic@unh.edu (M. Knezevic).

Keywords: Microstructures; Strength; Creep; Mukherjee – Bird – Dorn equation; Inconel 718

1 Introduction

Inconel 718 (IN 718) is a widely used nickel-based superalloy [1]. The primary use pertains to jet engine and industrial gas turbines components like blades, shafts, disks, and fasteners because of superior static strength, high temperature stability, and resistance to the elevated temperature creep and rupture exhibited by the alloy [2-4]. Since the alloy also has excellent corrosion and oxidation resistance, it is suitable for making containers for molten salt reactors [5]. The amount and types of constituent phases depend on the heat treatment conditions, manufacturing process and solidification [6]. The primary phase is austenite (γ), which is a solid solution of Ni-Fe-Cr with substitutional and interstitial alloying elements. Niobium (Nb), Molybdenum (Mo), and Manganese (Mn) are the common substitutional alloying elements, whereas Carbon (C) serves as interstitial one. These elements introduce localized lattice strains. The dislocation motion is impeded by these lattice strains causing hardening [1]. In addition to γ phase, there are secondary phases present in IN 718. The secondary phases are incoherent intermetallic δ (needle shaped), η, and Laves phases. Various carbides (i.e., MC and $M_{23}C_6$ where M = Metal and C = Carbon) are also observed in IN 718 microstructure[7-9]. Moreover, there are semi coherent or coherent particle-matrix interfaces present in the microstructure providing the greatest contribution to the hardening mechanism of IN 718. These are ordered cubic γ' ($L1_2$) and body-centered tetragonal (bct) γ'' ($D0_{22}$) with spherical and disk-shaped morphology, respectively [1]. The elemental compositions are listed in the Table 1. All these secondary phases (both coherent/semi-coherent and incoherent) have significant effects on the mechanical properties which depends on their morphology, chemistry, distribution, and interface coherency between particle and matrix. For example: the secondary incoherent phases play a significant role in refining grain size increasing the strength. However, if they have exceedingly coarse size and acicular shape, they exhibit detrimental effects on mechanical properties by providing less dispersion hardening. Furthermore, when these incoherent phases are located at the grain boundary, they will impede grain boundary sliding. Consequently, the ductility is reduced, but creep resistance is improved in some cases [1, 10, 11].

Table 4: Phases present in IN 718 with chemical composition, crystal structure, and space group per phase.

	Name	Crystal system	Space group	Primary composition
Solid solution matrix	γ	Cubic	Fm-3m	Ni, Cr, Fe – based
Intermetallic	γ'	Cubic	Pm-3m	Ni_3 (Ti, Al, Nb)
	γ''	Tetragonal	I4/mmm	Ni_3 (Nb, Ti)
Topographically closed packed (Intermetallic)	δ	Orthorhombic	Pmmn	Ni_3 (Nb, Ti)
	η	Hexagonal	P63/mmc	Ni_3 (Ti, Al)
	Laves	Hexagonal	P63/mmc	$(Ni, Cr, Fe)_2$ (Nb, Ti)
Carbide	MC	Cubic	Fm-3m	(Nb, Ti) (C, N)
	$M_{23}C_6$	Cubic	Fm-3m	$(Cr, Fe)_{23}$ C_6

Recently, additively manufacturing (AM) has become very popular in manufacturing fully functional end-use parts [12] like LEAP engine fuel nozzle [13] and low-pressure turbine blades [14] in the aviation and aerospace industries. Laser powder bed fusion, also known as LPBF, is one of the examples of AM technology and being extensively evaluated to make complex parts in the industries with the advantage of reducing the requirement of machining and expensive tooling over the traditional methods like forging [12, 15]. In LPBF, the component is built layer by layer. The powder particle is distributed to the build area within an inert gas atmosphere to build one layer. The laser fuses the particles together by fusion or melting and the layer of the component is built. Then, the build tray is lowered. Powder is spread again on the tray, and the next layer is fused. This process continues layer-by-layer until a full three-dimensional component is completed [16]. However, since LPBF is a novel manufacturing technology, studies are still being performed [16-19] to make connections between processing parameters, microstructure, phase content, mechanical and oxidation properties. Moreover, a fundamental requirement of AM in industrial implementation is the repeatability of the process [20]. Ensuring the input material (i.e., powder) quality is a critical step to achieve repeatability. Normally, the powders used in LPBF process are spherical and the particle size distribution (PSD) is to be optimized for both bulk density, should fit adequately within the layer, and layer thickness [21, 22]. There are other important features like morphology, flowability, chemical composition, humidity etc. [22-24]. According to several

studies [25, 26], highest real density and repeatability of the finished parts can be achieved by using spherical powders with PSD of 10-45μm. Moreover, the amount of nitrogen content (N), depending on argon (Ar) or N atomization, can affect the mechanical properties of final parts by controlling the recrystallization rate during heat treatment and morphology of carbides and nitrides [27].

Considerable research is being performed to confirm whether the components made by AM would be comparable to cast and wrought ones under monotonic and cyclic loading at the adverse conditions expected at typical applications. The presence of pores in the additively manufactured products is one of the primary concerns [28]. Porosity may occur due to unoptimized process parameters, scan strategies, powder feedstock properties etc. They can have different forms such as lack-of-fusion pores, metallurgical and keyhole pores [29]. It was also observed that despite the best optimization of LPBF parameters, formation of pores is inevitable [28]. During mechanical testing (monotonic or cyclic loading), pores could act as crack initiators causing premature failure [30]. Hot isostatic pressing (HIP) is a process where a part is placed under high temperature and confining gas pressure simultaneously for pore closure and microstructure homogenization of various metals which can provide beneficial effect on mechanical properties [31]. However, gas pores will not be closed due to the presence of confined gas inside [17].

Jiang et. al. found that because of HIP on IN 718 fabricated by LPBF, the specimen had MC-type carbide precipitates with ~39% decrease in microhardness ($HV_{2.0}$) and ~4% increase in Young's modulus [17]. After the HIP operation, the texture, previously exhibited moderate <001> fiber texture with columnar grains due to additive manufacturing of IN 718, changed to weak Goss component {110} <001> with equiaxed larger grain size. The high content (33%) of annealing twin boundaries were found to be the consequences of recrystallization and grain growth during HIP [32-38].

According to the literature, IN 718 exhibits the serrated yielding (SY) or dynamic strain aging (DSA) at high temperature regions (around 300^0-860^0C). The primary reason for DSA is the interaction between diffusing solute atoms and mobile dislocations [39-41]. According to dislocation arrest theory, solute atoms, immobile within lattice at room temperature, become mobile at high temperature along with dislocations. When load is applied, these mobile dislocations encounter obstacles (i.e., immobile forest dislocations surrounded by solute

atmosphere) and gets temporarily or permanently blocked. During this waiting period, solute atoms are diffused (pipe diffusion) from the forest dislocations to mobile dislocations. This accumulation of solutes strengthens the obstacles causing rise in the critical stress needed to overcome these obstacles. At a flow stress higher than this critical stress, these mobile dislocations quickly jump to the next obstacle, consequently increased strain and relaxed stress is observed [39, 42, 43]. Nalawade et. al. observed that there are two regimes of DSA for IN 718 – one below 525^0C which is controlled by diffusion of carbon (C) and other above 525^0C controlled by the diffusion of substitutional atom mainly Nb IN 718 It has also been observed that IN 718 processed by LPBF contains finely distributed intragranular δ phase [38] and smaller carbides than their wrought counterpart. During loading, the mobile dislocations glide and encounter obstacles like finely distributed precipitates at the grain interior with high dispersion hardening effect. The precipitates act as sinks for solute atoms, thus, draining them, causing less obstacles for mobile dislocations. This can result in the disappearance of DSA in additively manufactured IN 718. However, the wrought IN 718 consists of large carbides and delta phases, and they are coarsely distributed mostly at the grain boundaries. As a result, probability of arresting mobile dislocations is lower than AM IN 718, allowing them to move. The pipe diffusion mechanism dominates to drain solute atoms from forest dislocation to mobile dislocation, hence more obstacles, creating serrations at the same conditions for wrought material where AM IN 718 might not show serrated behavior [39, 42, 43]. So, the presence of finely distributed precipitation within the grains can affect the appearance or disappearance of DSA. Moreover, it has been observed that grain size, texture, negative strain rate sensitivity of flow stress might have on an influence on DSA phenomena [39, 42, 44].

When materials are placed at elevated temperature and static mechanical stress, deformation under such conditions is called creep [45]. In pure metals and simple alloys, three distinct stages were observed, i.e., primary, secondary and tertiary. However, for precipitation strengthened alloys, usually a short primary creep regime before progressively increasing creep strain was perceived [46]. Since IN 718 is commercially used in aerospace industry to make turbine blades under constant stress and temperature for a long period of time, the creep properties of this alloy made by AM technology need to be studied and considerable research is being performed at different operating temperatures [47-50]. Data exists in the literature for temperature range between 650^0C and 900^0C for IN 718 in both additive and wrought conditions. Z. Xu et al. [47]

performed tensile creep tests on samples fabricated by SLM at 700^0C under 500MPa and compared creep properties with wrought IN 718 after both materials went through the same double aging heat treatment. Poor creep performance was attributed to large columnar grains with broad distribution, continuous coarse δ precipitates distributed at grain boundaries and high residual stress for SLM IN 718. On the other hand, wrought IN 718 had fine equiaxed grains with narrow distribution, more twin boundaries, micro-twin, smaller size of γ'' phase and low residual stress to the structure before creep. The fracture surface analysis of SLM materials revealed no plastic deformation close to fracture and intergranular crack propagation. However, the wrought samples had unusual dimpled fracture surface with large plastic deformation with trans-granular crack propagation. [47].

Powder quality control is essential to obtain parts with desired mechanical properties in AM. During the process of making a part, a significant amount of powder remains unused. From ecological and economical perspectives, recycling these unused powders is an important aspect of making AM process more affordable. However, powder properties may change due to heating. Studies are being performed on the recycled powder characteristics such as PSD, morphology, composition (chemical, oxygen content, and microstructure), porosity, and flowability as well as the mechanical properties of parts made of reused powder [51, 52]. The effect of powder reuse on powder characteristics was investigated for IN 718 , Ti6Al4V, AlSi10Mg and Scalmalloy in [53]. Differences between the virgin and reused powder characteristics were observed and discussed from large for AlSi10Mg to small for Ti6Al4V. Given that recycled powder can change for IN 718, limited studies have been performed to evaluate the consequences on the material properties [26, 52, 54]. It is important to point out that Ardila et. al. [26, 52, 54] noticed significant difference for Nb content (~10% higher in reused powder) after characterizing both virgin and reused powders by energy dispersive spectroscopy (EDS) which could play a vital role in changing the inner microstructure and ultimately the mechanical properties.

The main goal of this study is to compare mechanical properties (tensile, compressive, and creep strength) between virgin and reused powders and the results will be explained by the available literature microstructure and composition data. IN 718 The mechanical properties are compared after testing specimens machined from rods fabricated via LPBF using virgin powder and powder that had been used in the process for some period of time. To this end, room

temperature compression tests, room temperature and elevated temperature tensile tests (600^0C, 650^0C, 700^0C and 750^0C), and creep tests (550^0C, 650^0C, 700^0C) under several constant stress conditions were performed. Results from these experiments are presented and discussed revealing the effects of powder reuse on the behavior of IN 718.

2 Experimental methods

2.1 Material processing

The LPBF was performed by EOS M280 using standard method of printing IN 718 with 400W laser power [55]. The layers were sintered by 40 μm of IN 718 powder at a time. Laser spot diameter at the metal pool was roughly 100 μm. During each building layer the laser sinters linearly in one direction. The following layer sinters linearly 67° from the previous layer's melting direction. To reduce the stress induced by thermal cycles, the build platform was heated to 80 °C. Rods were printed and underwent HIP at 1163 °C for 4 h under 100 MPa. The HIP temperature was high enough to trigger recrystallization. HIPing is known to stress relieve the alloy microstructure. Finally, the rods underwent heat treatment according to AMS 2774 [56].

2.2 Mechanical testing

2.2.1 Compression test

Cylinders with 6.33 mm in diameter and 8 mm in height were machined for compression testing from the as-received virgin and reused powder-based rods of IN 718. The testing procedure was established in earlier works [57-60] using an Instron Model # 1350 servohydraulic testing machine at a constant strain rate of $\sim 10^{-3}/\mathrm{s}$. The machine was equipped with DAX software, a controller along with a customized compression fixture. The fixture consisted of two hydraulic compression dies. They were aligned vertically along the axis of the actuator. At first, the compliance of the dies was measured. The raw data obtained after the compression of cylindrical IN 718 samples was corrected by subtracting the compliance data before computing the true stress-true strain curves. The load cell capacity was 100kN. The tests were interrupted before fracture. For repeatability, three samples per category were tested.

2.2.2 High temperature tensile tests

Reduced size tensile specimens where prepared per ASTM E8/E8M – 13a (Standard Test Methods for Tension Testing of Metallic Materials). A sketch of sample dimensions is provided in the appendix. Tensile specimens were threaded into custom Inconel load frame (Instron Model 1332 Servo Hydraulic Load Frame) grip adapters. The infrared (IR) heater controller (Research Inc. ControlIR Model 915) thermocouple was installed around the gage section of the tensile specimen. The IR heater (Research Inc. Model E4-2) was positioned and secured around specimen and grip adapters. Insulation was stuffed into the gaps between the IR heater and grip adapters to reduce thermal leakage. The specimen temperature was steadily increased to the test temperature over 20 minutes and then held at the test temperature for 10 minutes. Specimen was then preloaded to approximately 1kN before loading to failure at an extension rate of ~10^{-4} /s. After specimen failure the IR heater was powered off and the unit was allowed to cool to room temperature before removing specimen halves. Specimens were tested at room temperature, 600°C, 650°C, 700°C, and 750°C.

2.2.3 Creep tests

The creep tests were performed at *constant stress* on two WinCCS controlled lever arm testers (model # 2320-MM) manufactured by applied test systems (ATS). Each machine consists of extensometer frame (Series 4124A), load train (the combination of two series 4043 series pull rods, two series 4031A threaded couplings), two displacement encoders (left and right), and thermocouple junction where two K-type thermocouples (top and bottom) are plugged. The sample dimensions are shown in the appendix. The samples were heated steadily to the test temperature for about 1-1.5 hours and then held at that temperature for an hour. Cylinders made by LPBF were machined to make samples according to the dimensions provided in the appendix. Three temperatures, which are 550^0C (0.511 T_m), 650^0C (0.574 T_m) and 700^0C (0.605 T_m), were chosen. Where, T_m was considered as 1609^0K (1336^0C) [61]. Some tests were manually stopped well into the secondary region so that the creep parameters can be extracted based on Mukherjee-Bird-Dorn equation [62-64].

2.3 Microstructure and texture characterization

The initial microstructure and texture of both virgin and reused category were characterized by electron back scatter diffraction (EBSD) in a scanning electron microscope (SEM). It was a

Tescan Lyra 3 (Ga) field emission type of SEM and was equipped with Pegasus system (Octane Plus SDD detector and Hikari High Speed Camera). Automated EBSD data collection was performed at 20kV with ~2 μm step size at a working distance of 9-12 mm. Multiple scans from each category of samples were performed with a large scan area (about 3mm x 3 mm) in order to obtain representative texture measurement.

The samples of each materials category were mechanically polished by a series of SiC papers from 120 grit to 1200 grit. Then they were polished using 5 μm, 0.5 μm, 0.05 μm alumina suspension on a non-abrasive cloth. After vibratory polishing by 0.02 μm colloidal silica suspension, the samples were etched for 25-30s. The etching solution was prepared by mixing 25 mL deionized water, 20 mL hydrochloric acid (HCl), and 5 mL hydrogen peroxide (30%) (H_2O_2).

2.3.1 Fractography

Fractography was performed by Tescan Lyra 3 (Ga) field emission type of SEM. The SEM pictures were taken in secondary electron (SE) mode at 10-15 kV.

3 Results

3.1 Tensile and compressive behavior

True stress – true strain curves for virgin and reused powder sample categories at room temperature (RT) are presented in Fig: 1. As is evident, reused powder samples are a bit stronger in both tension and compression. The materials exhibit similar tension – compression asymmetry. The mechanical properties acquired from these tensile tests are shown in Table 2. The 0.2% yield strength (YS) is ~13% higher for reused powder than virgin powder. On the other hand, the ultimate tensile strength (UTS) and ductility for virgin powder category was 2.78% and 22.4% higher. The curves of wrought material (AMS 5663) are provided for reference.

To observe the change of strength and ductility at elevated temperature, tensile tests were performed at 600^0, 650^0, 700^0 and 750^0C (Fig. 2). The C-type dynamic strain aging (DSA) or serrated behavior was present for both virgin and used powder category. This type of serrations was characterized by sudden drop of stress below the general level of stress-strain curve because of dislocation unlocking at higher temperature and low strain rate [65]. At 650^0C, the serrated

behavior disappeared for virgin powder category. For reused powder category, DSA was present at all test temperatures. These results suggest some difference in the solid solution atom distribution between virgin and reused sample microstructures. However, characterizing this by microscopy would be challenging.

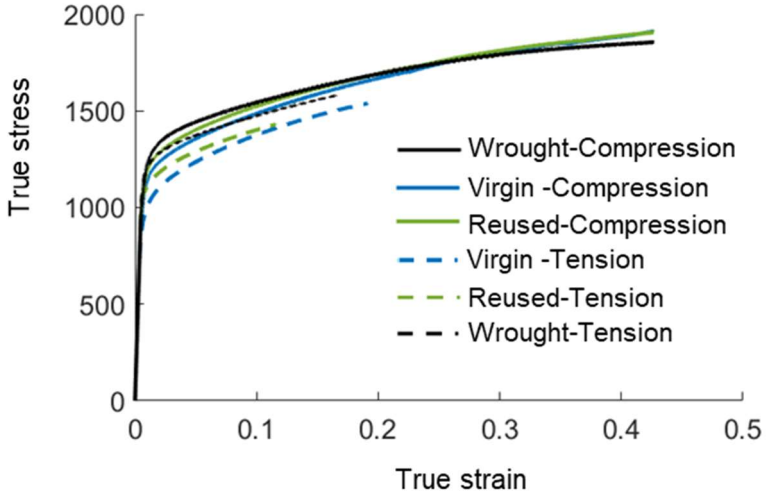

Figure 8: True stress – true strain curves measured in tension and compression for virgin and reused powder sample categories at room temperature. The curves of wrought material are provided for reference. While the compression tests were interrupted, the tension tests went to fracture.

Stress-strain curves recorded at elevated temperatures show that YS, UTS, uniform ductility, and ductility reduce with temperature. The YS and UTS of virgin powder category were always lower than the reused powder category except for the UTS at 650 ^{0}C, which was ~2% higher. In terms of ductility, the virgin powder category samples provided more uniform ductility than the reused powder category for all the temperatures. Among the temperatures chosen for this study, only 650^{0}C tensile behavior was found in the literature for commercially available wrought material [66, 67]. The YS and ductility of virgin powder samples were ~2% and ~7% lower than the wrought samples, respectively, while the UTS showed ~9% increase. For reused powder samples, the YS, UTS and ductility increased ~4%, ~6%, and ~7% compared to the wrought IN 718, respectively.

3.2 Microstructural characterization

To investigate the microstructure and texture of both category samples, EBSD was performed for initial samples (Fig. 3). The IPF maps show that the grains were elongated along the build direction (BD). Furthermore, ~30% of incoherent annealing twins were observed for both reused and virgin powder categories. The grain size was estimates to be 80 μm for both virgin and reused powder category. Given that grain size and texture are similar, these should not play any appreciable role in the difference in mechanical properties between the two categories of materials. However, the KAM maps for both categories exhibited some differences. The average KAM for reused powder material category was ~24% higher than the virgin category - meaning the dislocation density for reused powder samples is likely higher than in the virgin powder ones.

The pole figures were acquired from multiple large EBSD scans to get statistically significant number of grains that would represent the bulk texture of the material. Texture from both categories shows modest intensity of Goss component {110} <001>, which a consequence of recrystallization during HIP [38].

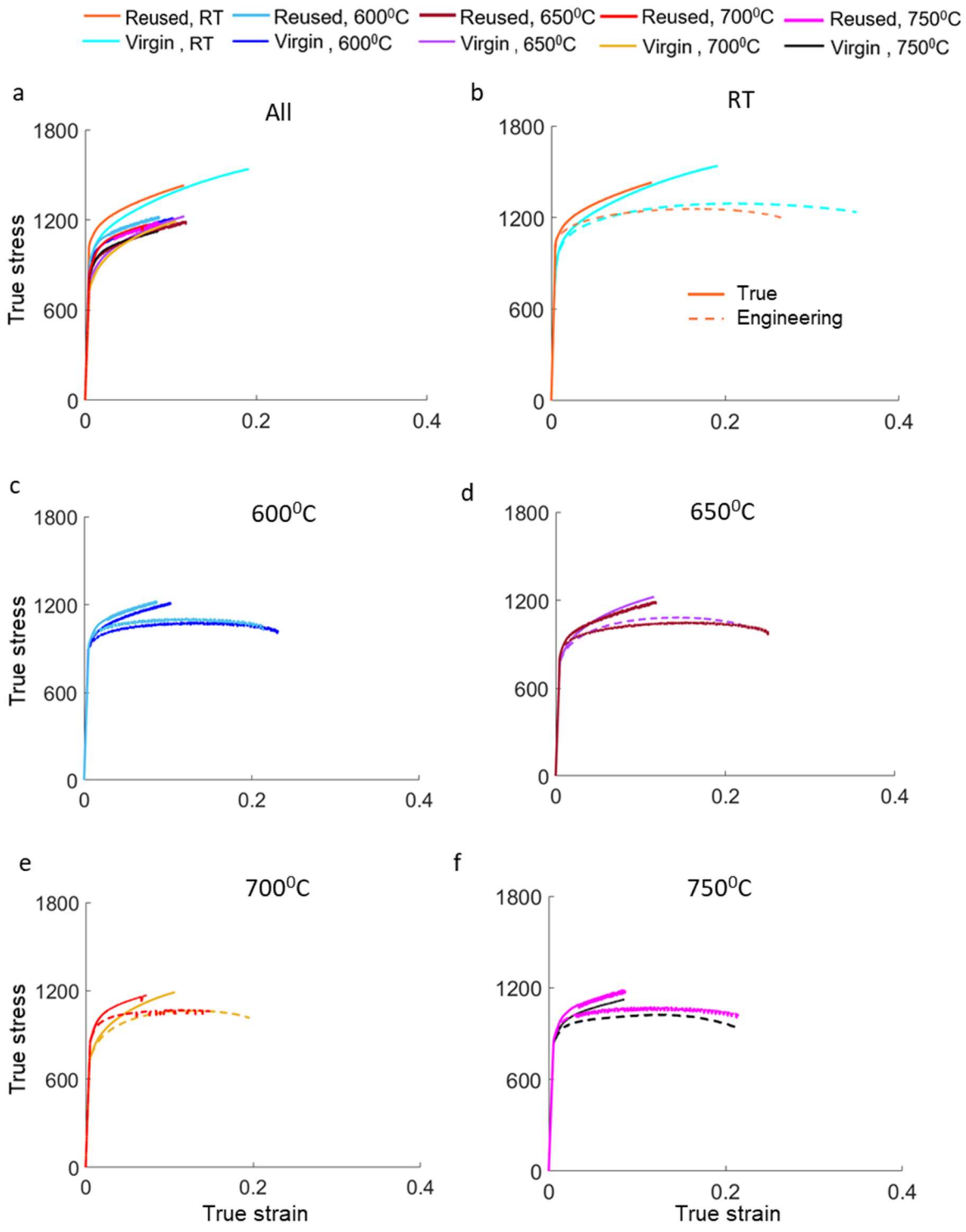

Figure 9: The true stress – true strain curves for virgin and reused powder samples at RT, 600^{0}C, 650^{0}C, 700^0 C, and 750^0 C in tension. All the samples were tested until fracture.

Table 5: 0.2% Yield Strength, UTS, engineering strain at UTS (uniform ductility), engineering strain at fracture (ductility) for tensile tests performed at various temperatures. The value for wrought sample at 650^0C is taken from literature.

Temperature (^{0}C)	Sample type	Sample category	Young's modulus, GPa	0.2% Yield Strength (MPa)	UTS, MPa	Engineering Strain at UTS (uniform ductility), %	Engineering Strain at fracture (ductility), %
RT	LPBF+HIP	Virgin	204.58	925	1293	21.01	35.09
		Reused		1074	1257	16.09	27.23
	Wrought (AMS 5663)		193.69	1169	1356	17.70	18.14
600 (0.543 T_m)	LPBF+HIP	Virgin	166.01	931	1081	13.65	23.15
		Reused		966	1106	12.26	21.32
650 (0.573 T_m)	LPBF+HIP	Virgin	162.89	817	1084	14.48	21.86
		Reused		867	1055	14.34	25.05
	Wrought [66]		----	830	990	17.16	23.38
700 (0.645 T_m)	LPBF+HIP	Virgin	160.74	767	1066	13.01	19.53
		Reused		898	1069	11.07	14.79
750 (0.635 T_m)	LPBF+HIP	Virgin	155.92	873	1024	12.27	21.63
		Reused		902	1075	11.57	21.48

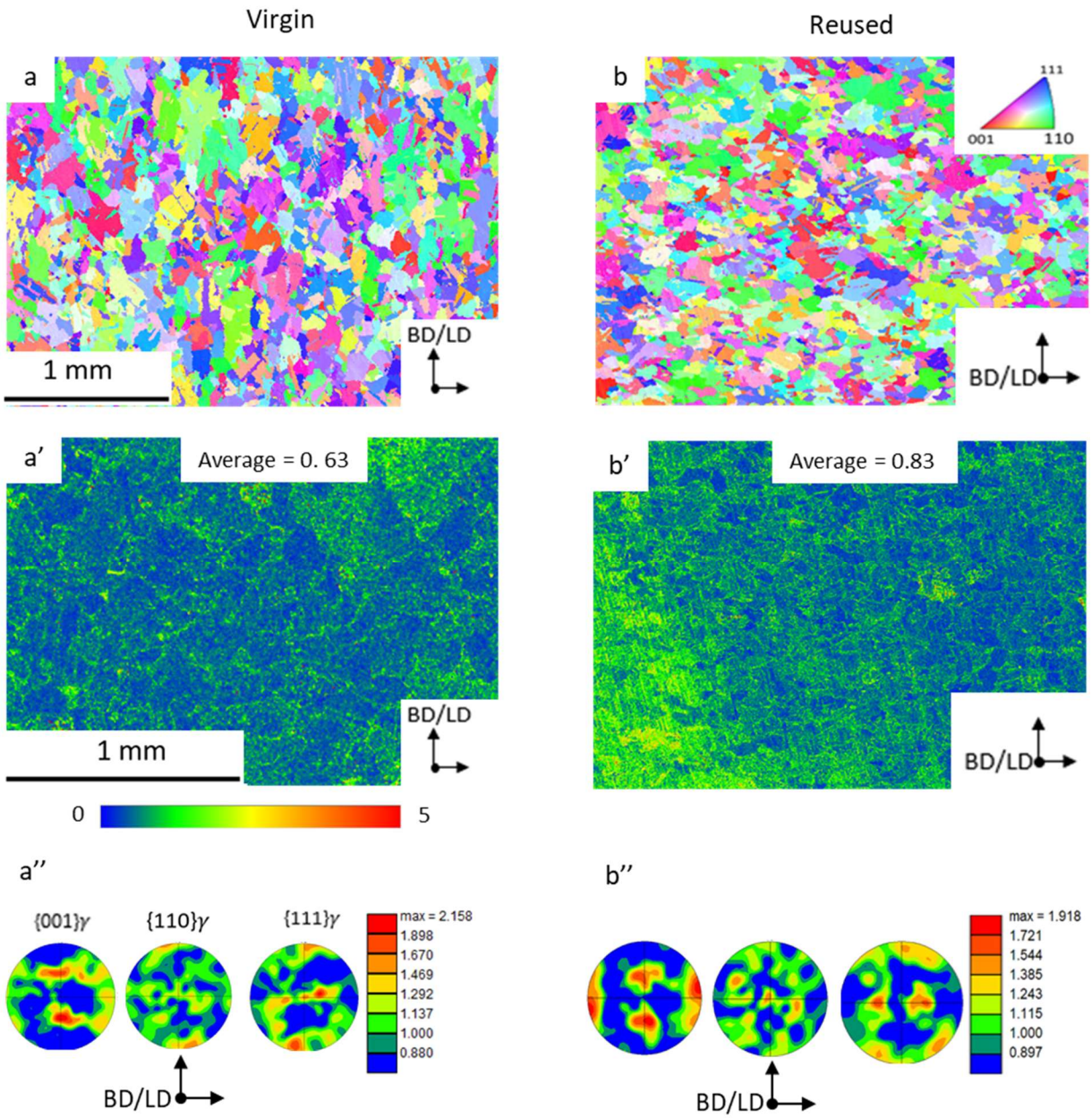

Figure 10: Inverse pole figure (IPF) maps (a, b), Kernel average misorientation (KAM) maps (a′, b′) and stereographic pole figures (a″, b″) showing microstructure and texture in the samples made from virgin and reused powders. The colors in the IPF maps represent the orientation of BD sample axis with respect to the crystal lattice frame according to the coloring in the standard IPF triangles. The pole figures were plotted after combining multiple scans.

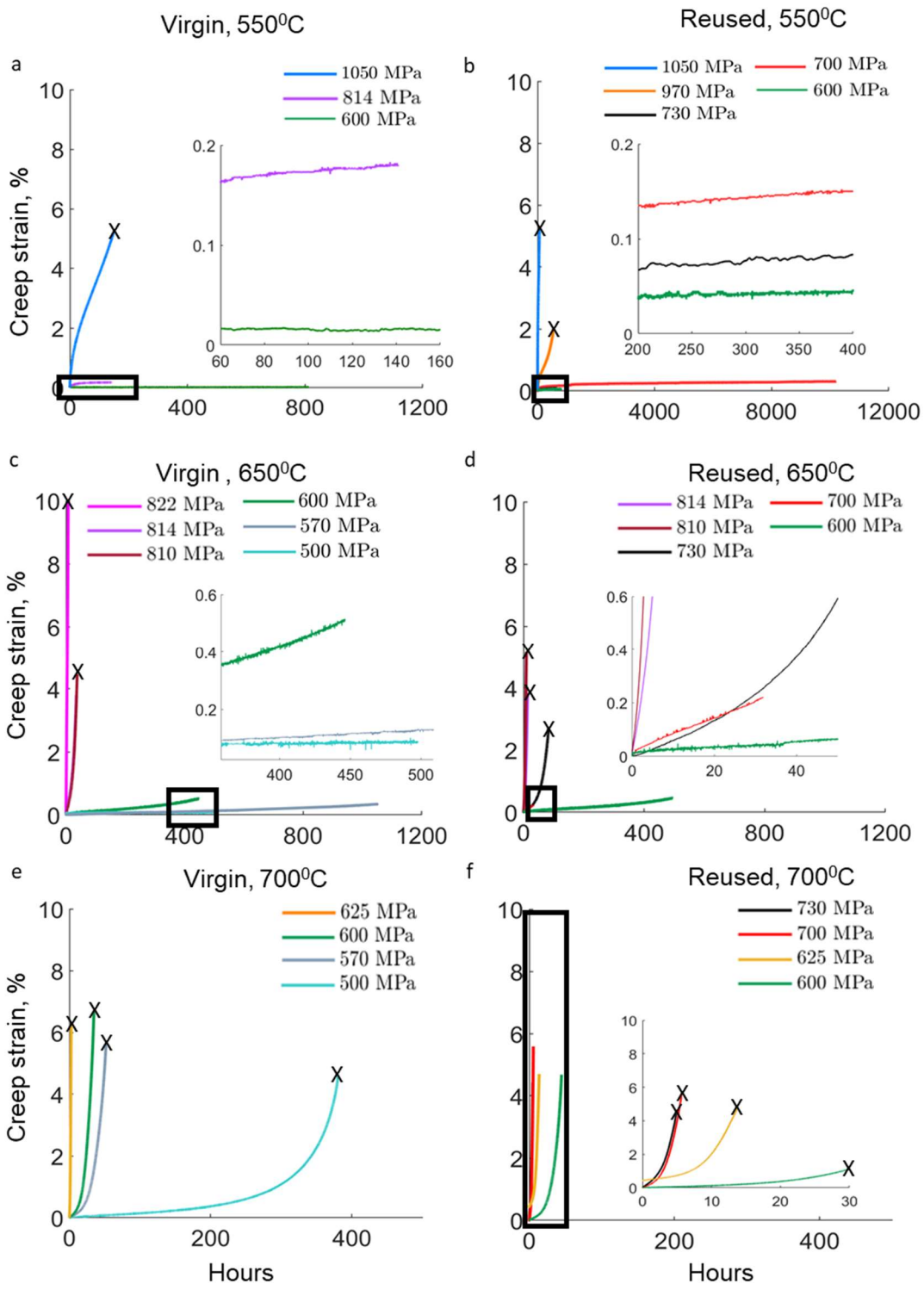

Figure 11: Creep strain (%) vs run time (hours) curves for samples made from virgin (a, c, and e) and reused (b, d, and f) powder at (a, b) 550^{0}C, (c, d) 650^{0}C, and (e, f) 700^0 C. The cross marks represent the point where the specimens ruptured.

Table 6: Applied stresses (σ MPa), measured time to rupture (t_r hours) and measured minimum creep rate ($\dot{\epsilon}_m$ /s) for all specimens tested in creep. The cross marks represent the point of time when the specimens ruptured. Here, Tm = 1609^0K (1336^0C).

	Virgin			Reused		
	Stress, σ MPa	Time to rupture, t_r hrs	Minimum creep rate,$\dot{\epsilon}_m/s$	Stress, σ MPa	Time to rupture, t_r hrs	Minimum creep rate, $\dot{\epsilon}_m/s$
550^0C (0.51 T_m)	**1050**	**150**^{x}	$5.19x10^{-4}$	**1050**	**63.67**^{x}	$5.44x10^{-4}$
	814	>142	$3.01x10^{-7}$	970	533^x	$3.08x10^{-6}$
	600	>300	$6.94x10^{-9}$	730	>688	$3.71x10^{-6}$
				700	>10120	$1.78x10^{-6}$
				600	>795	$1.08x10^{-8}$
650^0C (0.57 T_m)	822	7.30^x	$2.56x10^{-2}$	**814**	**13.02**^{x}	$7.57x10^{-4}$
	814	**34.00**^{x}	$5.36x10^{-4}$	**810**	**9.69**^{x}	$3.39x10^{-3}$
	810	**37.40**	$7.53x10^{-4}$	730	83.00^x	$7.84x10^{-5}$
	600	>470.0	$1.04x10^{-5}$	700	>30.00	$5.07x10^{-5}$
	570	>1050	$1.50x10^{-6}$	600	>493.00	$4.36x10^{-6}$
	500	>500	$1.47x10^{-7}$			
700^0C (0.60 T_m)	**625**	**2.54**^{x}	$1.29x10^{-2}$	730	4.9^x	$2.62x10^{-3}$
	600	**34.67**^{x}	$2.87x10^{-4}$	700	5.40^x	$1.39x10^{-3}$
	570	51.73^x	$1.46x10^{-4}$	**625**	**13.48**^{x}	$5.67x10^{-4}$
	500	379.00^x	$1.03x10^{-5}$	**600**	**46.00**^{x}	$1.80x10^{-4}$
	Total time = 3,157.64 hours			Total time = 12,898.39 hours		

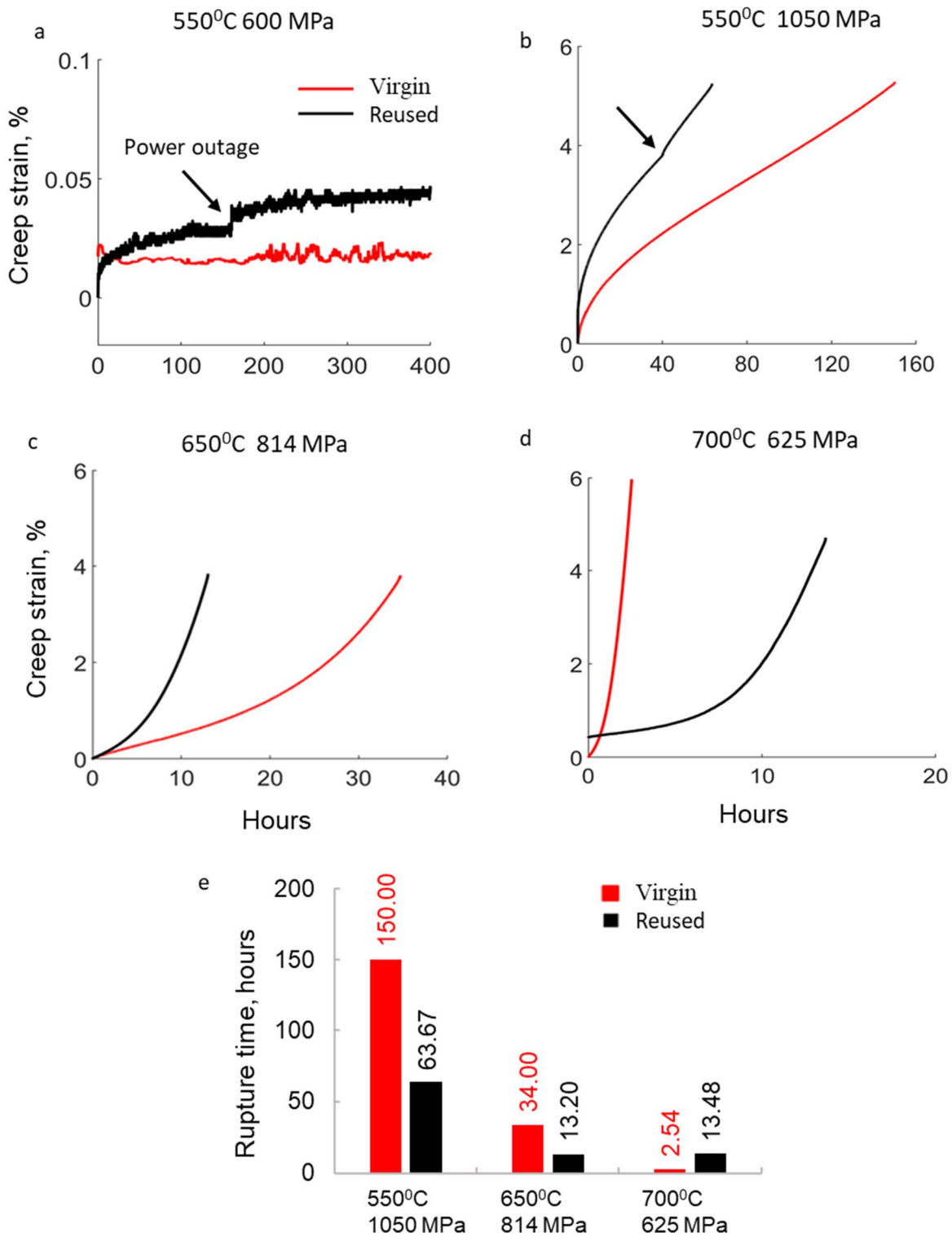

Figure 12: Creep strain (%) vs run time (hours) curves for samples made from virgin and reused powder at 550^{0}C and 600 MPa (a), 550^{0}C and 1050 MPa (b), 650^{0}C and 814 MPa (c), 700^{0}C and 625 MPa (d). The comparison between tests shown in (b), (c) and (d) in terms of the rupture time are showed in (e). The tests

performed at 650^0C 810 MPa and 700^0C 600MPa also show similar behavior relative to the ones performed as well as shown in this figure at 650^0C 814 MPa and 700^0C 625MPa.

3.3 Creep behavior

A total of 27 tests were performed from both categories at 550^0, 650^0 and 700^0C to observe the creep behavior in this study while keeping the applied stress constant. The creep strain (%) vs run time (hours) are shown in Fig. 4 for all tests. The purpose of performing all these tests was to evaluate any difference in creep behavior of the two sample categories and to establish the steady state creep behavior parameters (activation energy and stress exponent) for the materials. The stresses were chosen in such a way that at least three stresses are the same for all three temperatures at a specimen category (virgin or reused). Some tests which were taking very long time to rupture were manually stopped in the steady state creep region. The tests went to fracture are marked with cross at the end. As mentioned before, creep curves are normally divided into three stages: primary (usually very short), secondary (usually the longest) and tertiary. At high stress levels, the secondary stage is transient. Therefore, steady state creep rate ($\dot{\epsilon}_s$, /s) becomes a minimum strain rate ($\dot{\epsilon}_m$, /s) which will be used here after for all the tests. The minimum creep rate ($\dot{\epsilon}_m$/s), applied stress (σ MPa), and time to rupture (t_r hrs) for all the tests are shown in Table 3. To visualize these tests easily, Fig. 5 was plotted.

Tests under 550^0C and 600 MPa from both virgin and reused powder category were manually stopped in the steady state creep region. It was observed that the virgin powder sample is stronger and very little deformation or strain accumulation occurred during the creep test. On the other hand, the reused powder sample deformed and accumulated some strain at 600 MPa suggesting that the virgin powder sample is indeed stronger in the test condition. One thing to note here is that the sudden increase in strain at ~170 hours was because of a power outage while performing these long tests. Similar behavior was observed when the stress is increased to 1050 MPa. Both tests ruptured within 160 hours at the same strain level yet rupture life for the virgin powder sample was ~57% higher than reused powder category. At 650^0C and 814MPa, the rupture life exhibited similar pattern (~61% higher life for virgin powder sample) as the ones in 550^0C. The tests performed at 810 MPa show similar behavior to 814 MPa at 650^0C. Thus, the virgin powder category continues to be stronger at 650^0C. However, the virgin powder sample category

had ~81% shorter rupture life while accumulating ~21% more strain before fracture than the reused powder sample category for the tests performed at 700^0C under 625 MPa stress. The tests performed at 600 MPa show similar behavior to 625 MPa at 700^0C.

The stress exponent was calculated from the slope of ln ($\dot{\epsilon}_m$, /s) vs ln(σ) (showed in appendix) based on Mukherjee - Bird - Dorn equation [68] $\dot{\varepsilon}_m = A\sigma^n \exp(-\frac{H}{RT})$, where, A is a material constant. At a constant temperature, this equation can be written as $\ln \dot{\varepsilon}_m = n\ln\sigma + c$, where c is a constant. The stress exponent for virgin powder category samples were 20.0, 16.7 and 18.6 for 550^0C, 650^0C, and 700^0 C temperature, respectively. For reused powder category, the exponents of 16.1, 19.6, and 12.2 were estimated. These values are much higher than what is normally observed which is between 1 and 5 [69, 70]. The higher stress exponents were called the apparent stress exponents (n_{app}) and were an indication of shearing of precipitates by dislocations [71] . The significance of stress exponent will be discussed in detail in the following sections.

The Mukherjee - Bird - Dorn equation can also be rewritten as $\ln \dot{\varepsilon}_m = B - \frac{H}{RT}$ for a constant value of stress, where B is a constant. The activation energy (H) can be calculated from the slope of ln ($\dot{\epsilon}_m$, /s) vs $\frac{1000}{T(K)}$ at constant stress as shown in Fig. 6. Only activation energy for reused powder category was calculated. The activation energies for 600, 700 and 730 MPa at 550^0C, 650^0C, and 700^0C were 383.7, 280.4 and 290.5 kJ/mol, respectively.

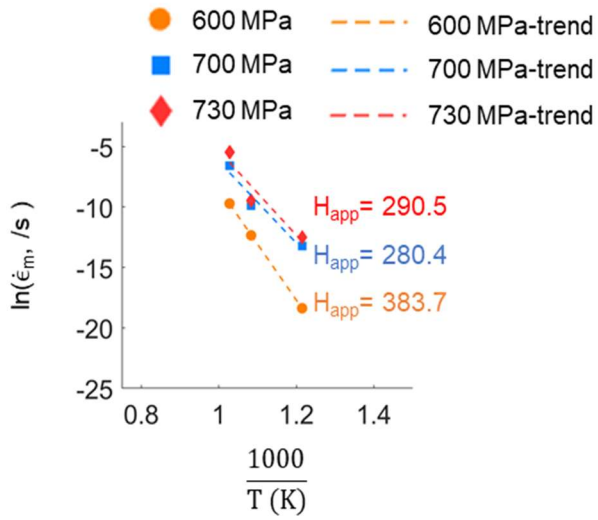

Figure 13: Apparent activation energy (H_{app} = kJ/mol) fits for samples of reused powder at 700, 730 and 600 MPa.

4 Discussion

4.1 Room temperature tension and compression

HIP was performed to improve the density by reducing pores, reduce residual stress fields, and improve the overall microstructural homogeneity. A set of fractography images showing some residual voids will be presented shortly. During compression residual voids collapse. The materials did not fracture during compression even up to a strain of ~0.45. During tension, voids can act as stress concentrations and influence the ductility. Samples made of virgin powder exhibited22.4% higher ductility than samples made of reused powder. However, the samples made of virgin powder were ~13% softer than those made of reused powder. The behavior is rationalized by a higher dislocation density as revealed by KAM and likely more effective dispersion hardening in the samples made of reused powder due to multiple heating cycles experienced by the reused powder. The stress-strain behavior of the alloy is characterized with some T-C asymmetry, which was rationalized with non-Schmid effects [72-74].

4.2 High temperature tensile behavior

IN 718 exhibits DSA at high temperatures. According to Nalawade et. al. [75] above 525^0C, substitutional elements are the main cause of DSA for IN 718 . The concentration of these elements in the matrix depends on the volume fraction of precipitates, γ' and γ'', since the primary composition of these precipitates includes substitutional elements such as Nb. At 700^0C, when the

thermal exposure itself can cause the γ" precipitation, Nb is quickly disappeared from the matrix causing the disappearance of serration – insufficient Nb to completely pin the dislocation [75].

Hayes [76] proposed another theory that the disappearance of DSA can be attributed to the formation of NbC causing insufficient Nb in the matrix. Literature also suggests that other substitutional elements like Cr in IN 718 [77] and Mo in IN 625 [78] might also contribute to the DSA. However, the occurrence of DSA is not only related to the diffusion energy but also to the solute-dislocation binding energy (W) which is directly related to solute vs matrix atom sizes [75, 79]. Therefore, Nb and Mo are considered to be the most effective in DSA mechanism since they contribute the most among other substitutional atoms (Cr, Fe) to expand the Ni lattice size, thus, increasing the binding energy between solute and dislocation [80].

Moreover, the temperature range of DSA can be shifted to higher or lower temperature based on the amount of interstitial solute atoms (especially C). Although they are not directly responsible for DSA at higher temperature by blocking the dislocations, the higher amount of C in the dislocation decreases the available sites for substitutional atoms in the tensile stress field near dislocation at high temperature. Therefore, increasing the interstitial elements shifts the DSA region to the lower temperature [80].

DSA or serrated yield behavior was observed in this study for high temperature tensile test at 600^0C for both virgin and reused powder category. However, it disappeared at 650^0C and continued being absent until 750^0C for the samples made of the virgin powder, while samples of the reused powder exhibited DSA from 650^0C to 750^0C (Fig. 2). Hence, samples made of virgin powder have different content and distribution of solute atoms in the solid solution and dislocation (less substitutional and more interstitial) than those made of reused powder. The behavior is likely due to the formation of NbC at high temperature will be lower than the reused powder category since dislocations can act as nucleation sites for NbC [81] as well as for lower fraction of Nb [54].

A decrease in ductility at high temperature is observed relative to RT. The decrease is likely caused because of the precipitation of MC carbide (NbC) at high temperatures. Zheng et. al. observed that with sufficient amount of Nb presence in the alloy, the precipitation of MC carbide (NbC) should not affect the formation of γ" phase [75, 82]. These carbides are very hard and brittle particles, which enhance strength but reduce ductility by forming microcracks around them. Such

cracks spread quickly throughout the matrix leading to fracture. Recently, Dong et. al. performed elevated temperature tests for samples fabricated by selective laser melting (SLM) and noticed that the main cause of ductility reduction is stress assisted time dependent intergranular cavitation which they rationalized as creep damage [83]. Although clear evidence of intergranular cavitation in this study was not found from the fractography (Fig. 8), the possibility was not ruled out.

4.3 Creep behavior

The formation intergranular precipitates (especially δ phase) has a greater effect at elevated temperature since preferential nucleation and growth of precipitates and also segregation of elements at grain boundaries can enhance intergranular cracking [84]. While at 550 °C and 600 °C samples of virgin powder last longer, at 700 °C samples of reused powder last longer (Fig. 5). The interesting behavior likely has to do with the difference in the content and distribution of diffusing solute atoms, initial dislocation density influencing the glide and diffusion, and precipitate spacing governing the dispersion strengthening. The material made of reused powder has more available dislocations to easily activate and start accommodating creep strain. However, at 700°C the more dislocations hinder the diffusion processes slowing down dissolution of the strengthening phases (PTT diagram presented in the appendix), but higher Nb content [54] might accelerate the precipitation of strengthening phase (mostly γ''). Moreover, needle like δ phase is breaking up into spherical δ phase by dislocation piling up at the needle shape δ phase and cutting through at elevated temperature and under high tensile stress [85]. Spherical δ phase has a retardation effect on the grain boundary crack initiation and propagation during creep [86].

Traditionally, the steady state creep or minimum creep rate ($\dot{\epsilon}_m$) is related to the applied stress (σ) by Mukherjee-Bird-Dorn power law creep equation [62-64]:

$$\dot{\varepsilon}_m = \frac{AGb}{kT} D_0 \exp\left(-\frac{H}{RT}\right)\left(\frac{\sigma}{G}\right)^n, \qquad (1)$$

where, A is material and structure dependent constant, G is shear modulus (Pa), b is Burger's vector (m), D_0 is diffusion coefficient (m^2/s), k is Boltzmann's constant (J/K), R is universal gas constant (J/mol), T is absolute temperature in K, H is activation energy (kJ/mol), and n is stress exponent for steady state creep. For most pure metals and simple alloys, n generally varies between

1 – 5 and H is generally the activation energy of self-diffusion [87]. The value of n is very useful to identify the creep mechanism and i.e., diffusion creep (n =1), grain boundary sliding (n = 2), dislocation glide (n =3), dislocation climb (n = 4–8) [69, 70, 88]. However, for alloys with complex microstructures (e.g., precipitation and/or oxide dispersion strengthened (ODS) nickel-based super alloys), n values have been observed between 7- 75 and activation energy (H) 2-3 times higher than reported self-diffusion [89-94]. The exponent, n, calculated based on Eq. 1 is referred to as n_{app}. This high n and H have been rationalized by the presence of back stress or threshold stress. An applied stress is opposed by the threshold stress generated from the presence of precipitates and defect structure within the material [95]. Hence, the creep deformation at the steady state is a consequence of effective stress ($\sigma - \sigma_0$) where, σ_0 is the threshold stress. The threshold stress is defined as a lower limiting stress below which strain rate is not measurable [96]. σ_0 is a microstructural characteristic. After including it into the Eq. 1, the governing equation is:

$$\dot{\varepsilon}_m = \frac{AGb}{kT} D_0 \exp\left(-\frac{H_a}{RT}\right)\left(\frac{\sigma-\sigma_0}{G}\right)^{n_a}, \qquad (2)$$

where n_a is the actual stress exponent and H_a is the actual activation energy. Introduction of σ_0 value reduces the stress exponent value for complex alloys to that for normally expected for pure metals and simple alloys [97] and once the σ_0 has been calculated, the rate controlling creep mechanism (i.e., diffusion, dislocation glide, dislocation climb) would also be similar [98].

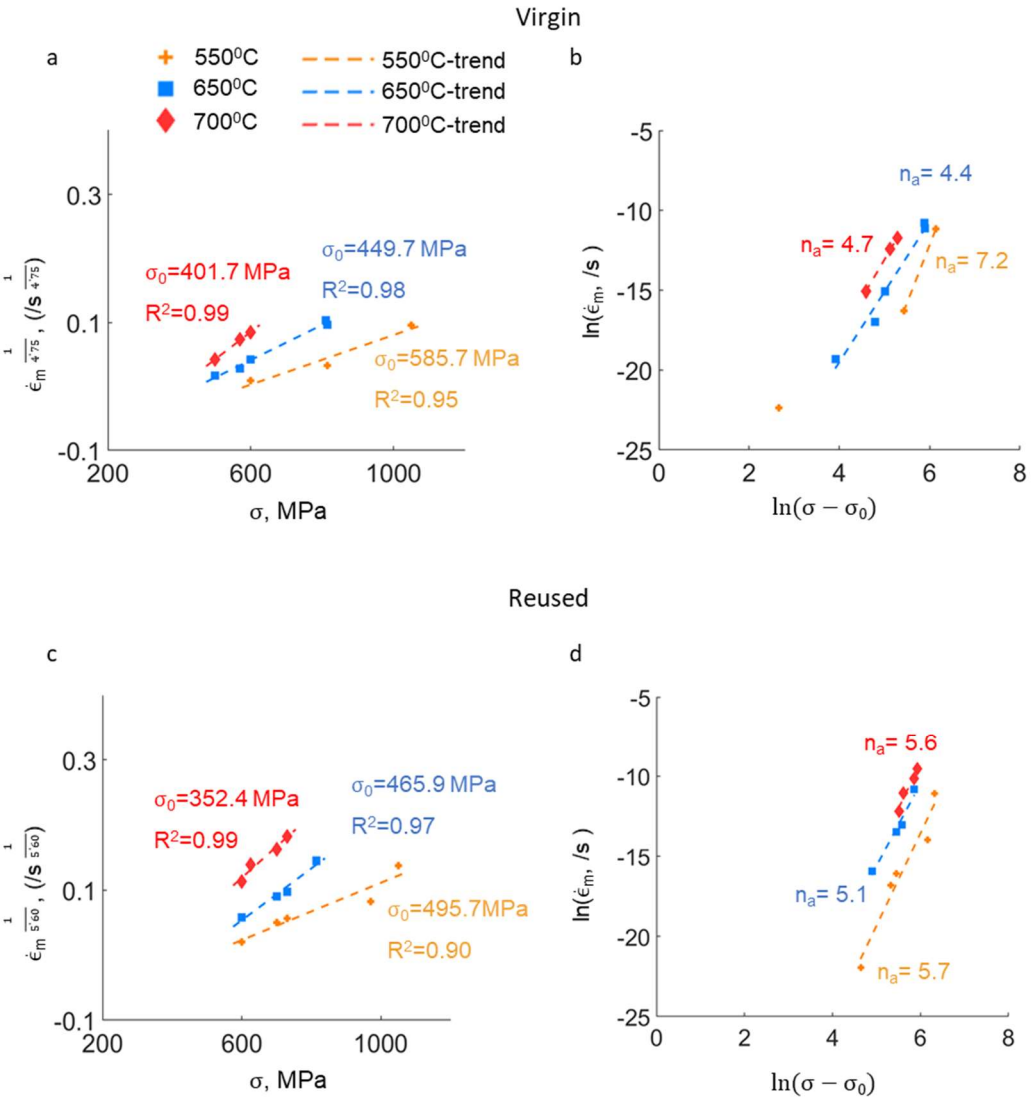

Figure 7: Lagneborg-Bergman plots to estimate threshold stress (σ_0) for (a) virgin and (c) reused category of samples. Recalculated stress exponents after using the obtained σ_0 (b, d).

In this study, the calculation of n_{app} provided about 3-4 times larger values relative to pure metals and alloys (showed in the appendix). Thus, threshold stress has been calculated by using Lagneborg-Bergman method [99] where $\dot{\varepsilon}_m^{\frac{1}{n}}$ is plotted on linear axes against σ after rearranging Eq. 1 at three test temperatures. The magnitude of σ_0 is the point where linear extrapolation of the curve intersects with zero strain rate (Fig. 7). The slope the curves will be $(\frac{AGb}{kT} D_0 \exp(-\frac{H}{RT}))^{\frac{1}{n}} \frac{1}{G}$

. It will be different because of the change in temperature and shear modulus. In our study, the value of n had been chosen as 4.75 and 5.60 for virgin and reused powder category, respectively, because the best fit (R^2) was achieved at these values after changing p between 3-8 [100]. The σ_0 value decreased with increasing temperature for both virgin and reused powder category which is consistent with the trend observed in the literature [95, 100]. The creep test performed at 550^0C and 600MPa showed very small strain rate could be because the threshold stress was ~0.97σ (see Table 4).

Normally, the activation energy is calculated for constant stress at various temperatures. At least three temperatures are needed to obtain a linear fit and from the slope calculate activation energy. In our case, for 500^0C, a couple of more tests under 570 and 500 MPa could not be performed which would have been lower than the σ_0 (585.87 MPa) for virgin powder category where power law creep might not be valid. The values of σ_0 is listed in Table 4 for both categories. Thus, activation energy of only reused powder category was calculated using same stress value for all three test temperatures.

Based on the parameters estimated from the experiment, the experimental curves were fitted at the steady state creep region based on Eq. 2. The parameter A was estimated as a constant for all stresses and temperatures per material and H was the same for a certain stress level across all three temperatures. The fit parameters are presented in Table 4, while the quality of fits is presented in the appendix. Some parameters (i.e., b, G, D_0) were taken from the literature [101, 102]. The dimensionless constant A can be approximated using an equation: $8e8*\exp(-103.8*(b/\lambda)^{0.5}$, where λ represents an interparticle spacing [103]. The λ for virgin and reused powder category was found as 21.99 and 16.43 nm, respectively, which was within the range of interparticle spacing of strengthening precipitates of IN 718 [104]. Note that precipitation radius scales inversely with the particle spacing. Reused powder underwent multiple heating cycles, which influences the precipitates. The main strengthening mechanism in IN 718 is shearing of dislocation through γ'' precipitates [105]. The higher number of precipitates provide higher dispersion hardening. Samples of reused powder are stronger than those of virgin powder in part due to better dispersion strengthening.

The stress exponents determined after fitting the steady state region of experimental curves (Table 5) exhibit similar values for both virgin and reused powder categories relative to the ones estimated in the earlier sections except for virgin category samples tested at 550^0C. The stress exponents determined after fitting decrease with increasing temperature likely because of precipitation of new strengthening particles with increasing temperatures and holding time. The exponents also suggest that creep is likely dominated by the dislocation climb. In this process the dislocations moved to another lattice plane while encountering an obstacle or precipitate. The rearrangements of atoms by vacancy diffusion were necessary for dislocation climb. Hence, the activation energy of dislocation creep normally coincides with self-diffusion of the material in its own crystal structure [88]. It had been observed that the apparent activation energy of Ni self-diffusion in austenite phase is H_d = 265-285 kJ/mol and the H_{app} for the power law creep is higher than H_d [106]. It was established that the dislocation density and dislocation velocity both control the creep and they are both dependent on activation energy equal to the self-diffusion of Ni [106]. The H_{app} in this study for reused powder (Fig. 6) exhibit the values within power law creep region. However, the activation energies are lower than what is reported in literature at intermediate temperature (around 650^0C) [85]. The activation energies were refined using fitting of the experimental curves as a function of stress. The determined values were close to the estimated ones in Fig. 6 for reused powder category (Table 6). The activation energy for 600 MPa was the highest because the test performed at 550^0C under 600 MPa required more activation energy for creep deformation since the threshold stress was within 85-97% of applied stress. For all cases, the activation energy decreased with increasing stress which was also supported by literature [107]. Furthermore, higher activation energies for virgin powder category were observed than the reused powder category. This difference in activation energies can be attributed to the difference in dislocation density, precipitation radius, and interparticle spacing.

Table 4a: Parameters used to fit the steady state region for the curves of virgin powder categories.

Temperature, K	G, $x10^{10}$ Pa	k, 10^{-23} m^2 kg s^{-2} K^{-1}	R, J/mol-K	b, 10^{-10} m	D_0, 10^{-4} m^2/s	n_a	σ, 10^6 Pa	σ_0, 10^6 Pa	H, 10^3 J/mol	A	Instantaneous + primary creep strain
823	6.94	1.38	8.314	2.50	2.00	4.80	1050.00	585.74	288.00	$1.25x10^4$	1.13
							814.00		332.20	$1.25x10^4$	0.18
							600.00		345.00	$1.25x10^4$	0.02

923	6.23					4.20	814.00	449.79	332.20	$1.25x10^4$	0.00
							810.00		336.00	$1.25x10^4$	0.00
							600.00		345.00	$1.25x10^4$	0.06
							570.00		352.00	$1.25x10^4$	0.07
							500.00		360.00	$1.25x10^4$	0.07
973	6.00					4.00	600.00	401.73	345.00	$1.25x10^4$	0.00
							570.00		352.00	$1.25x10^4$	0.00
							500.00		360.00	$1.25x10^4$	0.04

Table 4b: Parameters used to fit the steady state region for the curves of reused powder categories.

Temperature, K	G, $x10^{10}$ Pa	k, 10^{-23} m^2 kg s^{-2} K^{-1}	R, J/mol-K	b, 10^{-10} m	D_0, 10-^{4} m^2/s	n_a	σ, 10^6 Pa	σ_0, 10^6 Pa	H, 10^3 J/mol	A	Instantaneous + primary creep strain
823	6.94	1.38	8.314	2.50	2.00	5.90	1050.00	495.74	239.50	$2.20x10^3$	1.10
							970.00		255.00	$2.20x10^3$	0.20
							730.00		280.00	$2.20x10^3$	0.09
							700.00		273.00	$2.20x10^3$	0.15
							600.00		370.00	$2.20x10^3$	0.05
923	6.23					5.15	814.00	465.95	268.00	$2.20x10^3$	0.00
							730.00		287.00	$2.20x10^3$	0.00
							700.00		280.00	$2.20x10^3$	0.02
							600.00		370.00	$2.20x10^3$	0.02
973	6.00					5.69	700.00	352.49	280.00	$2.20x10^3$	0.00
							625.00		285.00	$2.20x10^3$	0.48
							600.00		370.00	$2.20x10^3$	0.02

Table 5: Stress exponents estimated and determined after fitting at 550^0C, 650^0C, and 700^0 C temperature.

Temperature (^{0}C)	Virgin	Reused
	n_a	

	Estimated	Determined by fitting	Estimated	Determined by fitting
550	7.26	4.80	5.90	5.90
650	4.40	4.20	5.15	5.50
700	4.79	4.00	5.69	5.45

Applied stress, MPa	Virgin	Reused	
	H, kJ/mol		
	Determined by fitting	Estimated	Determined by fitting
500	360.00	---	---
570	352.00	---	---
600	345.00	383	370.00
625	---	---	285.00
700	---	280	273.00
730	---	290	280.00
810	336.00	---	---
814	332.20	---	268.00
970	---	---	255.00
1050	288.00	---	239.50

Table 6: The estimated and determined fitting activation energy (kJ/mol) at stresses the tests were performed for virgin and reused powder category.

after the creep both

4.4 Fractography

The fractography of virgin and reused powder category samples under high temperature tension at RT and 650^0C shows dimple fracture (intragranular) (Fig. 8). For RT and 650^0C, both category of samples showed cup and cone fracture surface which is also typical for ductile fracture.

The fracture surface of the samples tested at 600^0C, 700^0C and 750^0C also exhibit similar behavior. They are not presented. On the other hand, the fractography of samples ruptured in creep clearly show two distinct regions (Fig. 9), which are the region fractured by creep (pointed with green arrow) and the region fractured by simple tension. Interestingly, the area of creep region increased with increasing temperature for both virgin and reused powder category. The bigger the creep fracture area the sample lasts longer. The high magnification pictures in creep fractured region shows mostly intergranular fracture with some trans granular fracture. A few zoomed in sections in the tensile fractured region exhibit mostly dimple fracture along with some trans-granular regions like in simple tension.

Xu et. al. observed during fractography that the IN 718 samples failed by creep have 2 distinct regions and called them as creep fracture zone (creep dominated area) and tensile fracture zone (ductile tearing) [84]. They theorized that because of creep void and pores will start to emerge and during their growth they will connect with each other. After a while, the cross section will start to fail, and cross-section area will decrease. With stressed area continuously decreasing, the applied stress will exceed the YS and UTS, and the rest of the cross-section area will be torn apart by pure tensile loading [108]. Further analysis revealed that, (Nb, Ti) C carbides which are at the grain boundaries act as crack initiator for heat-treated samples. On the other hand, the HIPed samples only exhibited semi-ductile fracture along with observable precipitates at the grain boundary. Those precipitates were identified as δ phase. In the tensile zone, both HIPed and heat-treated samples showed only dimple fracture indicative of pure ductile fracture [84].

In our samples, the creep region showed intergranular sharp cracks for all the cases probably because of carbides and δ at the grain boundary. According to the literature, wedge type

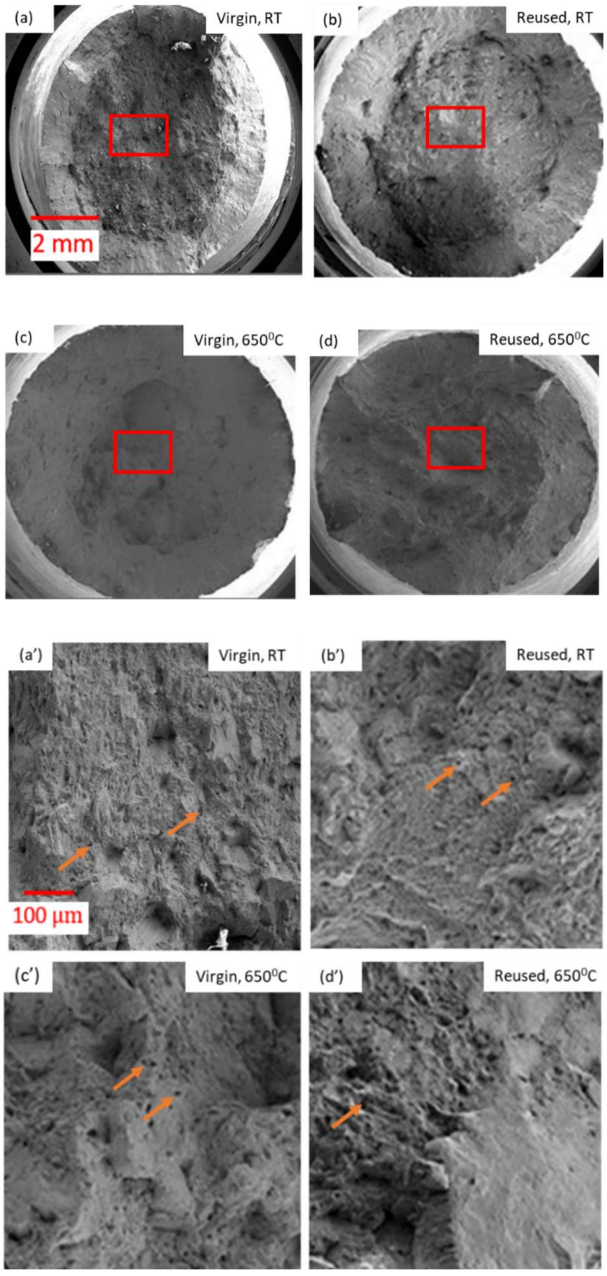

Figure 8: Fractured surfaces for several samples after tensile tests at various temperatures. The subfigures are arranged as follows: (a) virgin powder samples at RT, (b) reused powder samples at RT, (c) virgin powder samples at 650^0C, (d) reused powder samples at 650^0C. The areas with red rectangles from (a-d) are magnified in (a′-d′). A few pores are pointed out with orange arrows.

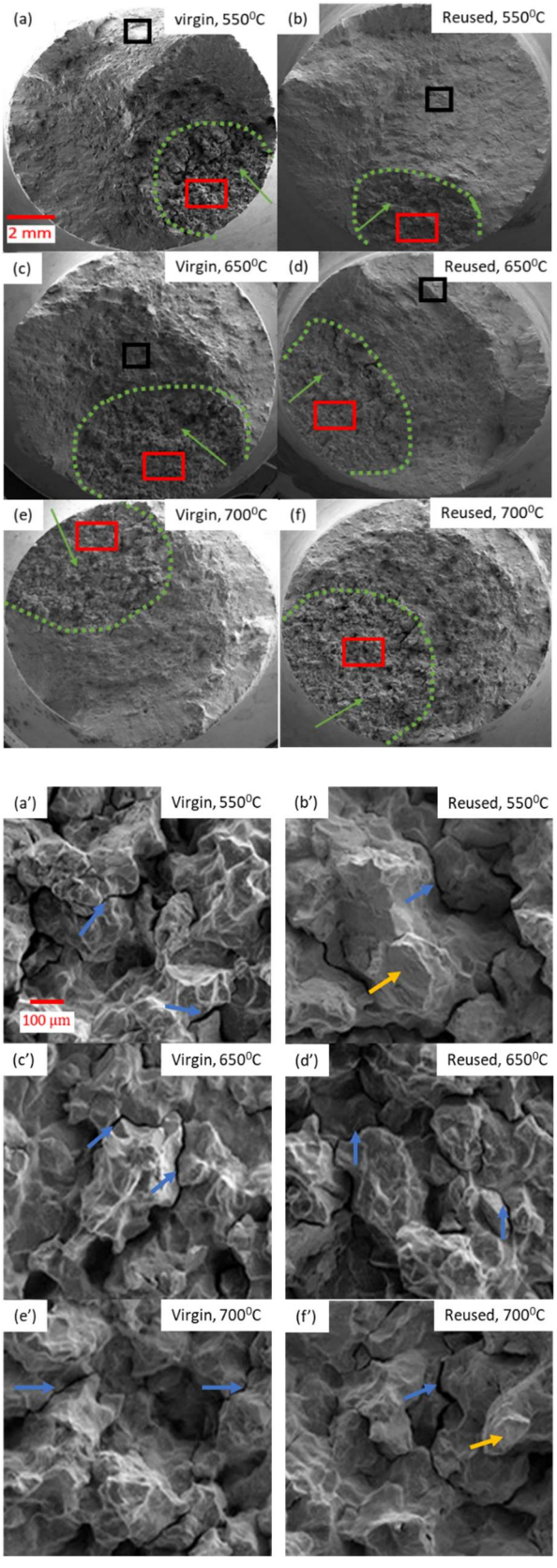
(a)
virgin, 550^{0}C
(b)
Reused, 550^{0}C
2 mm
(c)
Virgin, 650^{0}C
(d)
Reused, 650^{0}C
(e)
Virgin, 700^{0}C
(f)
Reused, 700^{0}C
(a')
Virgin, 550^{0}C
(b')
Reused, 550^{0}C
100 µm
(c')
Virgin, 650^{0}C
(d')
Reused, 650^{0}C
(e')
Virgin, 700^{0}C
(f')
Reused, 700^{0}C

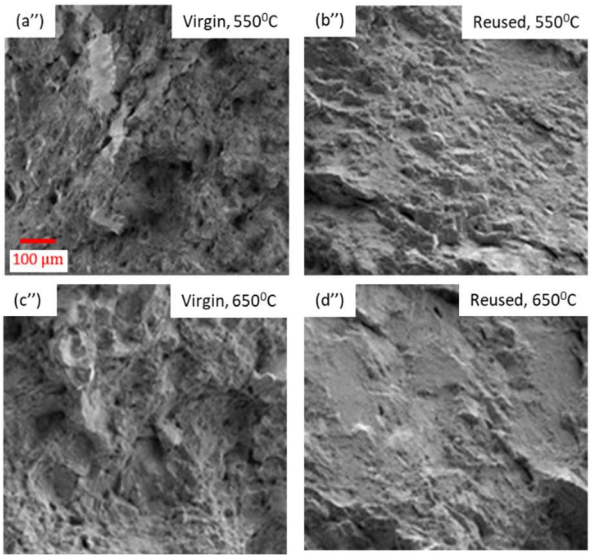

Figure 9: Fractured surfaces for selected samples after creep rupture at various temperatures. The subfigures are arranged as follows: (a) virgin category samples at 550^{0}C and 1050 MPa, (b) reused category samples at 550^{0}C and 1050 MPa, (c) virgin category samples at 650^{0}C and 814 MPa, (d) reused category samples at 650^{0}C and 814 MPa (e) virgin category samples at 700^{0}C and 625 MPa (f) reused category samples at 700^{0}C and 625 MPa. The regions fractured during creep are separated by the green lines and indicated by the green arrows from the regions fractured by simple tension. Selected areas in red are magnified in (a′-f′), while selected areas in black are magnified in (a′′-d′′). Some intergranular fracture is shown by blue arrows, while some trans-granular fracture is depicted with yellow arrows.

(w-type) cracks, formed mainly at the triple junctions of grain boundaries, are the main source of voids for heat-treated LPBF samples [84]. Chen et. al. found that when the density of δ precipitates at the grain boundary is low, fracture was caused by the propagation of w-type cracks which was originated from the δ precipitates [109]. The nucleation of these cracks had been attributed to the grain boundary sliding [110]. Since the material in this study had been heat treated after LPBF + HIP and intergranular sharp cracks was observed, w-type cracks could be the reason of crack formation during creep. Some trans-granular region observed in the fractography could be a consequence of larger voids present in that region originated from lack of fusion in LPBF. The tensile zone was mostly consisted of dimple fracture and facets, but some trans-granular features were also observed for reused samples ruptured at 550^0 and 650^{0}C.

5 Conclusions

In this study, the effect of powder reusing on the tensile, compressive and creep strength were investigated for Inconel 718 samples fabricated by LPBF. The rods, made by LPBF for both virgin and reused powders, were HIPPed and then heat treated by AMS 2774. Grain structures and

textures, characterized by EBSD, did not exhibit significant difference, but higher dislocation density was estimated in the sample made by reused powder. From room temperature compression and tensile tests, it was perceived that the reused powder samples had higher dispersion hardening compared to the virgin powder ones. Although serrated behavior was observed for both category of samples at 600^0C, it disappeared for virgin powder category samples at 650^0, 700^0C, and 750^0C. This disappearance of serration was rationalized by higher NbC formation because of higher Nb content and higher dislocation density. Furthermore, the creep test results showed that until 650^0C temperature, the samples made from virgin powder lasted significantly (~2.5 times) longer than the reused powder. At 700^0C, reused powder samples lasted about 6 times longer relative to virgin powder samples. The stress exponents estimated by measured data and subsequent refinement by a data fitting using the Mukherjee -Bird – Dorn equation suggest that the creep behavior at secondary region was controlled by dislocation climb for both category of samples. Higher creep life for samples made by reused powder was attributed to the higher precipitation rate of strengthening particles as well as spheroidization of needle shaped δ phase particles because of interaction with dislocations. From these observations, it will be our recommendation to use a component fabricated by LPBF with virgin powder until 650^0C. After 650^0C, components made by reused powder will be more suitable. This study will also provide the creep behavior at 550^0C which will be important for designing parts for this temperature application with additively manufactured Inconel 718.

Acknowledgments

This research was sponsored by the U.S. Army Research Laboratory and was accomplished under Cooperative agreement no. W911NF-15-2-0084.

Appendix

This appending presents drawings of the specimens used in the testing in tension (Fig. A1) and in creep (Fig. A2), calculation of apparent stress exponent (Fig. A3), precipitation-temperature-time diagram for IN 718 (Fig. A4), and creep parameters fits (Fig. A5).

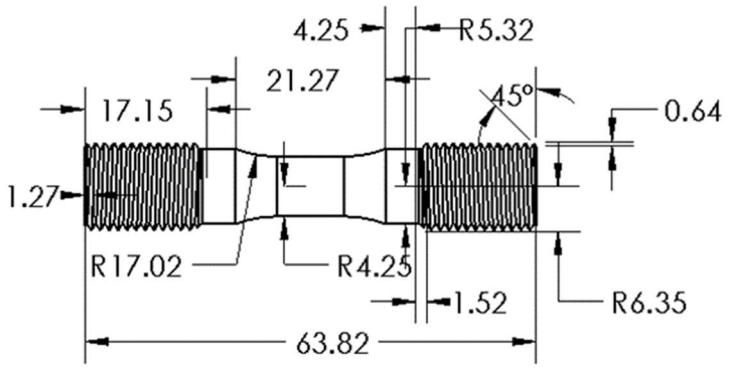

Figure A2: Drawing of the sample used for performing tensile tests at various temperatures following ASTM E8/E8M – 13a standard. Dimensions are in mm.

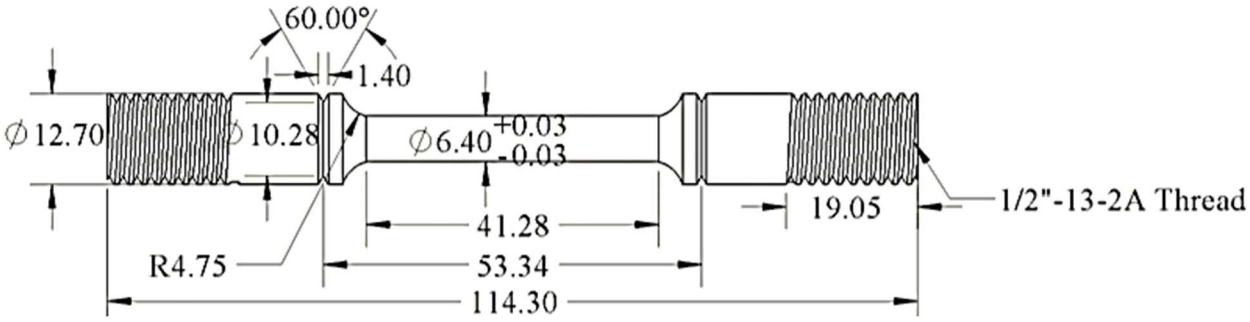

Figure A3: Drawing of the creep specimen. Dimensions are in mm.

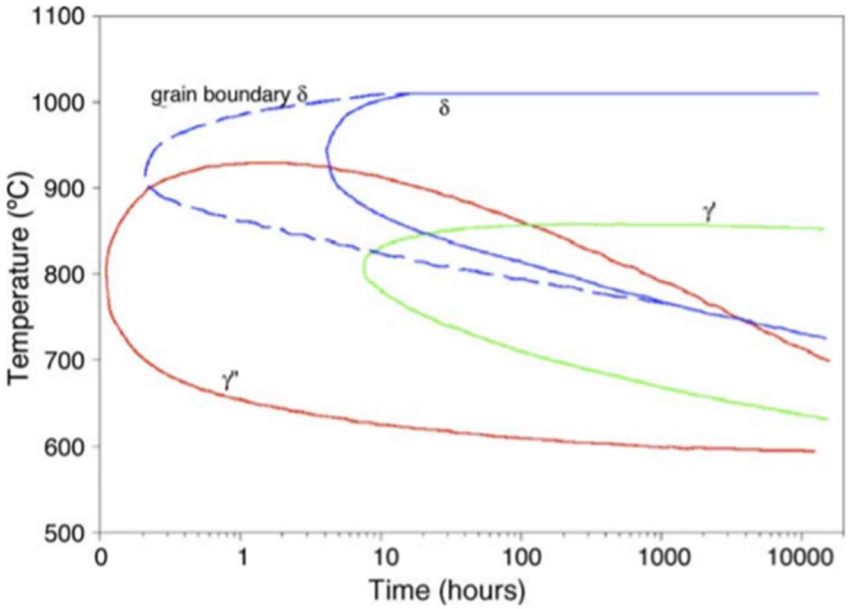

Figure A3: Precipitation-time-temperature (PTT) diagram of different phases in IN 718 [111].

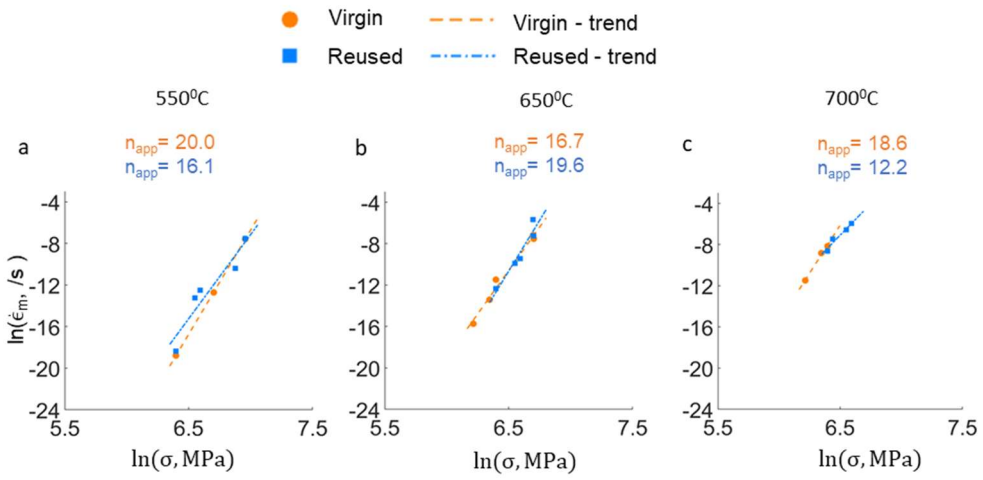

Figure A 4: The creep strain (%) vs run time (hours) curves for both virgin and used category samples at 550^{0}C and 600 MPa (a), 550^{0}C and 1050 MPa (b), 650^{0}C and 814 MPa (c), 700^{0}C and 625 MPa (d). The comparison between tests performed at 550^{0}C, 650^{0}C and 700^{0}C under 1050, 814 and 625 MPa in terms of rupture time are showed in (e).

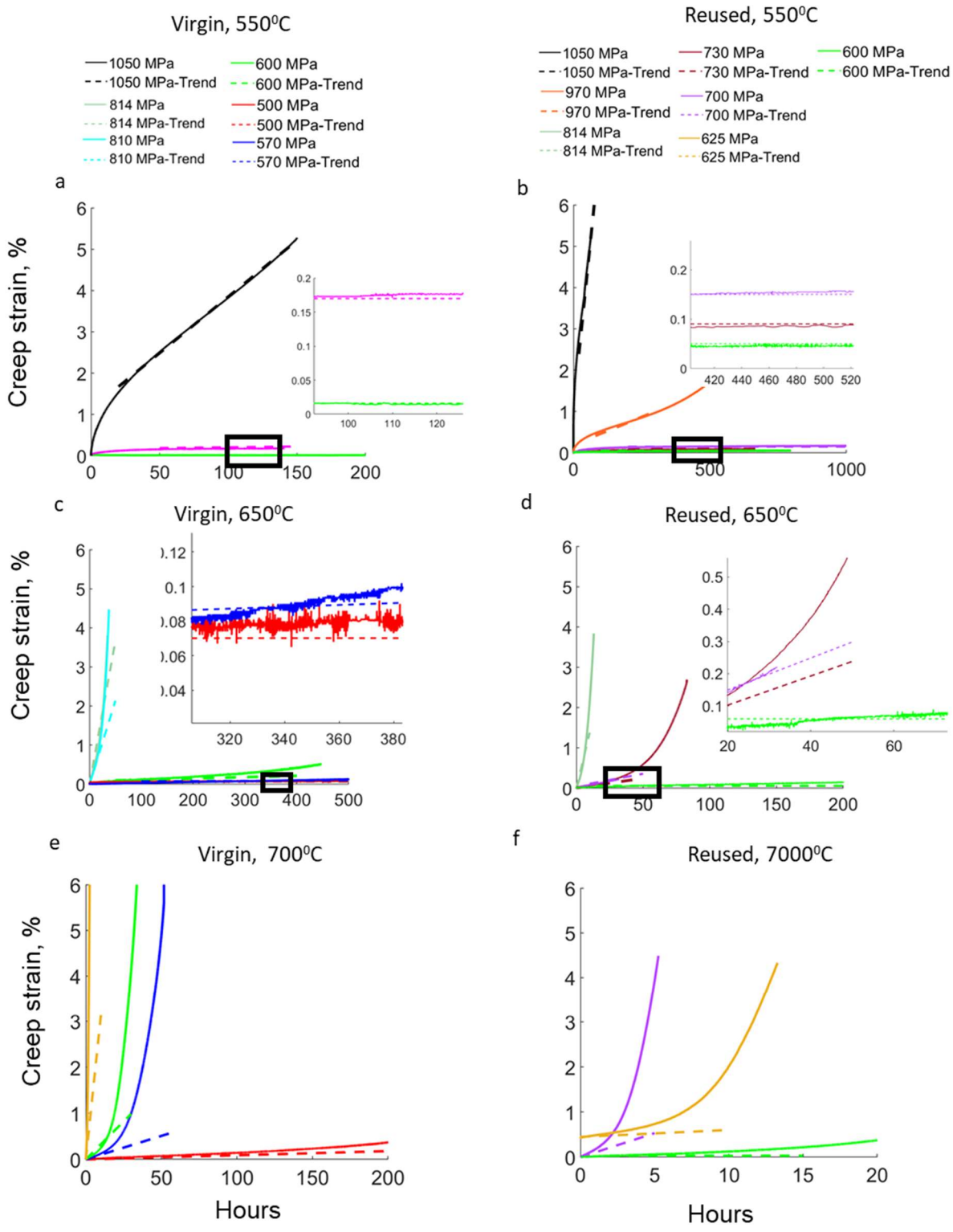

Figure A5: Fits of the steady state region of the creep strain (%) vs run time (hours) curves using the Mukherji-Bard-Dorn equation for the samples of virgin (a, c, and e) and reused (b, d, and f) powder at (a, b) 550^{0}C, (c, d) 650^{0}C, and (e, f) 700^0 C.

References

[1] W.F. Smith, Structure and properties of engineering alloys, McGraw-Hill Book Co., xiv+ 512, 23 x 16 cm, illustrated(16. 95) (1981).

[2] J.R. Davis, ASM specialty handbook: heat-resistant materials, Asm International1997.

[3] S. Safdar, A.J. Pinkerton, L. Li, M.A. Sheikh, P.J. Withers, An anisotropic enhanced thermal conductivity approach for modelling laser melt pools for Ni-base super alloys, Applied mathematical modelling 37(3) (2013) 1187-1195.

[4] M. Knezevic, B.K. Chun, J.Y. Oh, W.T. Wu, R.A. Ress Ill, M.G. Glavicic, S. Srivatsa, Modeling the machining distortion using the finite element method: application to engine disk, Los Alamos National Lab.(LANL), Los Alamos, NM (United States), 2011.

[5] A.K. Misra, J.D. Whittenberger, Fluoride salts and container materials for thermal energy storage applications in the temperature range 973–1400 K, 22nd Intersociety Energy Conversion Engineering Conference, American Institute of Aeronautics and Astronautics, 1987, p. 9226.

[6] N.C. Ferreri, S.C. Vogel, M. Knezevic, Determining volume fractions of γ, γ′, γ ″, δ, and MC-carbide phases in Inconel 718 as a function of its processing history using an advanced neutron diffraction procedure, Materials Science and Engineering: A 781 (2020) 139228.

[7] M. Burke, M. Miller, Precipitation in alloy 718: a combined Al3M and apfim investigation, Superalloys 718(625) (1991) 337-350.

[8] S. Ghosh, S. Yadav, G. Das, Study of standard heat treatment on mechanical properties of Inconel 718 using ball indentation technique, Materials Letters 62(17) (2008) 2619-2622.

[9] S. Azadian, L.-Y. Wei, R. Warren, Delta phase precipitation in Inconel 718, Materials characterization 53(1) (2004) 7-16.

[10] A.W. Thompson, J.F. Knott, Micromechanisms of brittle fracture, Metallurgical Transactions A 24(3) (1993) 523-534.

[11] A. Weronski, Thermal fatigue of metals, CRC Press1991.

[12] E.D. Herderick, Progress in additive manufacturing, JOM 67(3) (2015) 580-581.

[13] T. Kellner, World's first plant to print jet engine nozzles in mass production, GE Reports (2014).

[14] This Electron Gun Builds Jet Engines. https://www.ge.com/news/reports/this-electron-gun-builds-jet-engines, August 18, 2014).

[15] D. Cooper, J. Thornby, N. Blundell, R. Henrys, M. Williams, G. Gibbons, Design and manufacture of high performance hollow engine valves by additive layer manufacturing, Materials & Design 69 (2015) 44-55.

[16] S. Gribbin, J. Bicknell, L. Jorgensen, I. Tsukrov, M. Knezevic, Low cycle fatigue behavior of direct metal laser sintered Inconel alloy 718, Int. J. Fatigue 93, Part 1 (2016) 156-167.

[17] R. Jiang, A. Mostafaei, J. Pauza, C. Kantzos, A.D. Rollett, Varied heat treatments and properties of laser powder bed printed Inconel 718, Mater. Sci. Eng. A 755 (2019) 170-180.

[18] D. Brown, D. Adams, L. Balogh, J. Carpenter, B. Clausen, G. King, B. Reedlunn, T. Palmer, M. Maguire, S. Vogel, In situ neutron diffraction study of the influence of microstructure on the mechanical response of additively manufactured 304L stainless steel, Metallurgical and Materials Transactions A 48(12) (2017) 6055-6069.

[19] N.C. Ferreri, S. Ghorbanpour, S. Bhowmik, R. Lussier, J. Bicknell, B.M. Patterson, M. Knezevic, Effects of build orientation and heat treatment on the evolution of microstructure and mechanical properties of alloy Mar-M-509 fabricated via laser powder bed fusion, International Journal of Plasticity 121 (2019) 116-133.

[20] L. Portolés, O. Jordá, L. Jordá, A. Uriondo, M. Esperon-Miguez, S. Perinpanayagam, A qualification procedure to manufacture and repair aerospace parts with electron beam melting, Journal of Manufacturing Systems 41 (2016) 65-75.

[21] A. Cooke, J. Slotwinski, Properties of metal powders for additive manufacturing: a review of the state of the art of metal powder property testing, US Department of Commerce, National Institute of Standards and Technology2012.

[22] J.A. Slotwinski, E.J. Garboczi, Metrology needs for metal additive manufacturing powders, Jom 67(3) (2015) 538-543.

[23] A.T. Sutton, C.S. Kriewall, M.C. Leu, J.W. Newkirk, Powder characterisation techniques and effects of powder characteristics on part properties in powder-bed fusion processes, Virtual and physical prototyping 12(1) (2017) 3-29.

[24] L. Grainger, Understanding the effects of metal powder re-use in laser powder-bed fusion AM, Proceedings of Fraunhofer direct digital manufacturing conference, 2018.

[25] K. Riener, N. Albrecht, S. Ziegelmeier, R. Ramakrishnan, L. Haferkamp, A.B. Spierings, G.J. Leichtfried, Influence of particle size distribution and morphology on the properties of the powder feedstock as well as of AlSi10Mg parts produced by laser powder bed fusion (LPBF), Additive Manufacturing 34 (2020) 101286.

[26] K. Gruber, I. Smolina, M. Kasprowicz, T. Kurzynowski, Evaluation of Inconel 718 Metallic Powder to Optimize the Reuse of Powder and to Improve the Performance and Sustainability of the Laser Powder Bed Fusion (LPBF) Process, Materials 14(6) (2021) 1538.

[27] C.K. Sudbrack, B.A. Lerch, T.M. Smith, I.E. Locci, D.L. Ellis, A.C. Thompson, B. Richards, Impact of powder variability on the microstructure and mechanical behavior of selective laser melted alloy 718, Proceedings of the 9th International Symposium on Superalloy 718 & Derivatives: Energy, Aerospace, and Industrial Applications, Springer, 2018, pp. 89-113.

[28] A. Du Plessis, E. Macdonald, Hot isostatic pressing in metal additive manufacturing: X-ray tomography reveals details of pore closure, Additive Manufacturing 34 (2020) 101191.

[29] H. Gong, K. Rafi, H. Gu, T. Starr, B. Stucker, Analysis of defect generation in Ti–6Al–4V parts made using powder bed fusion additive manufacturing processes, Additive Manufacturing 1 (2014) 87-98.

[30] J.J. Lewandowski, M. Seifi, Metal additive manufacturing: a review of mechanical properties, Annual review of materials research 46 (2016) 151-186.

[31] H. Atkinson, S. Davies, Fundamental aspects of hot isostatic pressing: an overview, Metallurgical and Materials Transactions A 31(12) (2000) 2981-3000.

[32] U.F. Kocks, C.N. Tomé, H.-R. Wenk, Texture and anisotropy: preferred orientations in polycrystals and their effect on materials properties, Cambridge university press1998.

[33] M. Zecevic, R.J. McCabe, M. Knezevic, A new implementation of the spectral crystal plasticity framework in implicit finite elements, Mechanics of Materials 84 (2015) 114-126.

[34] M. Jahedi, M.H. Paydar, S. Zheng, I.J. Beyerlein, M. Knezevic, Texture evolution and enhanced grain refinement under high-pressure-double-torsion, Materials Science and Engineering: A 611 (2014) 29-36.

[35] M. Zecevic, W. Pantleon, R.A. Lebensohn, R.J. McCabe, M. Knezevic, Predicting intragranular misorientation distributions in polycrystalline metals using the viscoplastic self-consistent formulation, Acta Materialia 140 (2017) 398-410.

[36] R.A. Lebensohn, M. Zecevic, M. Knezevic, R.J. McCabe, Average intragranular misorientation trends in polycrystalline materials predicted by a viscoplastic self-consistent approach, Acta Materialia 104 (2016) 228-236.

[37] M. Knezevic, N.W. Landry, Procedures for reducing large datasets of crystal orientations using generalized spherical harmonics, Mechanics of Materials 88 (2015) 73-86.

[38] S. Gribbin, S. Ghorbanpour, N.C. Ferreri, J. Bicknell, I. Tsukrov, M. Knezevic, Role of grain structure, grain boundaries, crystallographic texture, precipitates, and porosity on fatigue behavior of Inconel 718 at room and elevated temperatures, Materials Characterization 149 (2019) 184-197.

[39] A.M. Beese, Z. Wang, A.D. Stoica, D. Ma, Absence of dynamic strain aging in an additively manufactured nickel-base superalloy, Nature communications 9(1) (2018) 1-8.

[40] Y. Cai, C. Tian, G. Zhang, G. Han, S. Yang, S. Fu, C. Cui, Q. Zhang, Influence of γ′ precipitates on the critical strain and localized deformation of serrated flow in Ni-based superalloys, Journal of Alloys and Compounds 690 (2017) 707-715.

[41] P. Maj, J. Zdunek, M. Gizynski, J. Mizera, K. Kurzydlowski, Statistical analysis of the Portevin–Le Chatelier effect in Inconel 718 at high temperature, Materials Science and Engineering: A 619 (2014) 158-164.

[42] R. Hayes, W. Hayes, A proposed model for the disappearance of serrated flow in two Fe alloys, Acta Metallurgica 32(2) (1984) 259-267.

[43] A. Sleeswyk, Slow strain-hardening of ingot iron, Acta Metallurgica 6(9) (1958) 598-603.

[44] S. Mannan, Role of dynamic strain ageing in low cycle fatigue, Bulletin of Materials Science 16(6) (1993) 561-582.

[45] W.D. Callister, D.G. Rethwisch, A. Blicblau, K. Bruggeman, M. Cortie, J. Long, J. Hart, R. Marceau, M. Ryan, R. Parvizi, Materials science and engineering: an introduction, wiley2021.

[46] B. Dyson, Microstructure based creep constitutive model for precipitation strengthened alloys: theory and application, Materials science and technology 25(2) (2009) 213-220.

[47] Z. Xu, L. Cao, Q. Zhu, C. Guo, X. Li, X. Hu, Z. Yu, Creep property of Inconel 718 superalloy produced by selective laser melting compared to forging, Materials Science and Engineering: A 794 (2020) 139947.

[48] J. Shi, X. Li, Z. Zhang, G. Cao, A. Russell, Z. Zhou, C. Li, G. Chen, Study on the microstructure and creep behavior of Inconel 718 superalloy fabricated by selective laser melting, Materials Science and Engineering: A 765 (2019) 138282.

[49] H. Zhang, C. Li, Q. Guo, Z. Ma, H. Li, Y. Liu, Improving creep resistance of nickel-based superalloy Inconel 718 by tailoring gamma double prime variants, Scripta Materialia 164 (2019) 66-70.

[50] J. Shi, S. Zhou, H. Chen, G. Cao, A. Russell, Z. Zhou, X. Qi, C. Li, G. Chen, Microstructure and creep anisotropy of Inconel 718 alloy processed by selective laser melting, Materials Science and Engineering: A 805 (2021) 140583.

[51] P.E. Carrion, A. Soltani-Tehrani, N. Phan, N. Shamsaei, Powder recycling effects on the tensile and fatigue behavior of additively manufactured Ti-6Al-4V parts, Jom 71(3) (2019) 963-973.

[52] F. Yi, Q. Zhou, C. Wang, Z. Yan, B. Liu, Effect of powder reuse on powder characteristics and properties of Inconel 718 parts produced by selective laser melting, Journal of Materials Research and Technology 13 (2021) 524-533.

[53] L. Cordova, M. Campos, T. Tinga, Revealing the effects of powder reuse for selective laser melting by powder characterization, Jom 71(3) (2019) 1062-1072.

[54] L.C. Ardila, F. Garciandia, J.B. González-Díaz, P. Álvarez, A. Echeverria, M.M. Petite, R. Deffley, J. Ochoa, Effect of IN718 Recycled Powder Reuse on Properties of Parts Manufactured by Means of Selective Laser Melting, Physics Procedia 56 (2014) 99-107.

[55] E.N.I.D. Sheet, EOS GmbH-Electro Optical Systems, 2014.

[56] A. 2774, Heat Treatment Wrought Nickel Alloy and Cobalt AlloyParts. https://doi.org/10.4271/AMS2774E, 2016).

[57] S. Ghorbanpour, B.A. McWilliams, M. Knezevic, Effect of hot working and aging heat treatments on monotonic, cyclic, and fatigue behavior of WE43 magnesium alloy, Materials Science and Engineering: A 747 (2019) 27-41.

[58] S. Ghorbanpour, B.A. McWilliams, M. Knezevic, Low-cycle fatigue behavior of rolled WE43-T5 magnesium alloy, Fatigue & Fracture of Engineering Materials & Structures 42(6) (2019) 1357-1372.

[59] M. Jahedi, B.A. McWilliams, P. Moy, M. Knezevic, Deformation twinning in rolled WE43-T5 rare earth magnesium alloy: influence on strain hardening and texture evolution, Acta Materialia 131 (2017) 221-232.

[60] D.H. Smith, J. Bicknell, L. Jorgensen, B.M. Patterson, N.L. Cordes, I. Tsukrov, M. Knezevic, Microstructure and mechanical behavior of direct metal laser sintered Inconel alloy 718, Materials Characterization 113 (2016) 1-9.

[61] S. Metals, Inconel alloy 718, Publication Number SMC-045. Special Metals Corporation (2007).

[62] A. Mukherjee, J. Bird, J. Dorn, The role of climb in creep processes in proceedings of symposium, The interactions between dislocations and point defects, United Kingdom Atomic Energy Authority Harwell, UK1968, pp. 422-495.

[63] J.E. Dorn, A.K. Mukherjee, Application of Rate Theory to Dislocation Dynamics, (1969).

[64] J. Bird, A. Mukherjee, J. Dorn, Quantitative relation between properties and microstructure, Israel Universities Press, Jerusalem, 1969) p 255 (1969).

[65] S. Chen, X. Xie, W. Li, R. Feng, B. Chen, J. Qiao, Y. Ren, Y. Zhang, K.A. Dahmen, P.K. Liaw, Temperature effects on the serrated behavior of an Al0. 5CoCrCuFeNi high-entropy alloy, Materials Chemistry and Physics 210 (2018) 20-28.

[66] M.M. Kirka, F. Medina, R. Dehoff, A. Okello, Mechanical behavior of post-processed Inconel 718 manufactured through the electron beam melting process, Materials Science and Engineering: A 680 (2017) 338-346.

[67] K.A. Unocic, L.M. Kolbus, R.R. Dehoff, S.N. Dryepondt, B.A. Pint, High-temperature performance of UNS N07718 processed by additive manufacturing, NACE corrosion (2014).

[68] J. Harper, J.E. Dorn, Viscous creep of aluminum near its melting temperature, Acta Metallurgica 5(11) (1957) 654-665.

[69] F. Garofalo, Fundamentals of Creep and Creep-Rupture in Metals Macmillan Company, New York 620 (1965) G237f.

[70] O.D. Sherby, P.M. Burke, Mechanical behavior of crystalline solids at elevated temperature, Progress in materials science 13 (1968) 323-390.

[71] J. Huo, J. Gou, L. Zhou, X. Qin, G. Li, High temperature creep deformation mechanisms of a hot corrosion-resistant nickel-based superalloy, Journal of materials engineering and performance 16(1) (2007) 55-62.

[72] S. Copley, B. Kear, A dynamic theory of coherent precipitation hardening with application to nickel-base alloys(Coherent precipitation hardening theory treats yielding in nickel base alloy containing coherent stress-free ordered particles as dynamic process), AIME, TRANSACTIONS 239 (1967) 984-992.

[73] S. Keshavarz, S. Ghosh, A crystal plasticity finite element model for flow stress anomalies in Ni3Al single crystals, Philosophical Magazine 95(24) (2015) 2639-2660.

[74] S. Ghorbanpour, M. Zecevic, A. Kumar, M. Jahedi, J. Bicknell, L. Jorgensen, I.J. Beyerlein, M. Knezevic, A crystal plasticity model incorporating the effects of precipitates in superalloys: Application to tensile, compressive, and cyclic deformation of Inconel 718, Int. J. Plast. 99(Supplement C) (2017) 162-185.

[75] S. Nalawade, M. Sundararaman, R. Kishore, J. Shah, The influence of aging on the serrated yielding phenomena in a nickel-base superalloy, Scripta Materialia 59(9) (2008) 991-994.

[76] R. Hayes, On a proposed theory for the disappearance of serrated flow in fcc Ni alloys, Acta Metallurgica 31(3) (1983) 365-371.

[77] C. Hale, W. Rollings, M. Weaver, Activation energy calculations for discontinuous yielding in Inconel 718SPF, Materials Science and Engineering: A 300(1-2) (2001) 153-164.

[78] I.S. Kim, M.C. Chaturvedi, Serrated flow in Inconel 625, Transactions of the Japan institute of metals 28(3) (1987) 205-212.

[79] R. Hayes, Dynamic aging of 18 wt-% Ni maraging 250 steel, based on studies of serrated flow, Materials Science and Technology 1(4) (1985) 285-290.

[80] B. Max, B. Viguier, E. Andrieu, J.M. Cloue, A re-examination of the Portevin-Le Chatelier effect in alloy 718 in connection with oxidation-assisted intergranular cracking, Metallurgical and Materials Transactions A 45(12) (2014) 5431-5441.

[81] K. Gururaj, S. Pal, Influence of dislocation density and grain size on precipitation kinetics on P92 grade steel, Materials Today: Proceedings 18 (2019) 1364-1374.

[82] W.-j. Zheng, X.-p. Wei, Z.-g. Song, Q.-l. Yong, H. Feng, Q.-c. Xie, Effects of carbon content on mechanical properties of Inconel 718 alloy, Journal of Iron and Steel Research International 22(1) (2015) 78-83.

[83] D. Deng, R.L. Peng, J. Moverare, High temperature mechanical integrity of selective laser melted alloy 718 evaluated by slow strain rate tests, International Journal of Plasticity 140 (2021) 102974.

[84] Z. Xu, J. Murray, C. Hyde, A. Clare, Effect of post processing on the creep performance of laser powder bed fused Inconel 718, Additive Manufacturing 24 (2018) 486-497.

[85] K. Chen, J. Dong, Z. Yao, Creep Failure and Damage Mechanism of Inconel 718 Alloy at 800–900° C, Metals and Materials International (2019) 1-15.

[86] S. Li, J. Zhuang, J. Yang, X. Xie, The effect of phase on crack propagation under creep and fatigue conditions in alloy 718, Superalloys 718 (1994) 625-706.

[87] O. Ajaja, T.E. Howson, S. Purushothaman, J.K. Tien, The role of the alloy matrix in the creep behavior of particle-strengthened alloys, Materials Science and Engineering 44(2) (1980) 165-172.

[88] N.E. Dowling, Mechanical behavior of materials : engineering methods for deformation, fracture, and fatigue, Englewood Cliffs, N.J. : Prentice Hall, [1993] ©19931993.

[89] D. Sidey, B. Wilshire, Mechanisms of creep and recovery in nimonic 80A, Metal Science Journal 3(1) (1969) 56-60.

[90] C. Carry, J. Strudel, Apparent and effective creep parameters in single crystals of a nickel base superalloy—I Incubation period, Acta Metallurgica 25(7) (1977) 767-777.

[91] S. Purushothaman, O. Ajaja, J.K. Tien, On the Concept of Back Stress in Particle Strengthened Alloys, Strength of Metals and Alloys, Elsevier1979, pp. 251-257.

[92] A. Clauer, B. Wilcox, Steady-State Creep of Dispersion-Strengthened Nickel, Metal Science Journal 1(1) (1967) 86-90.

[93] B. Wilcox, A. Clauer, Creep of thoriated nickel above and below 0.5 Tm, Trans. Met. Soc. AIME 236 (1966).

[94] R. Cairns, L. Curwick, J. Benjamin, Grain growth in dispersion strengthened superalloys by moving zone heat treatments, Metallurgical Transactions A 6(1) (1975) 179-188.

[95] Y. Han, M. Chaturvedi, A study of back stress during creep deformation of a superalloy inconel 718, Materials science and Engineering 85 (1987) 59-65.

[96] J. Gibeling, W. Nix, The description of elevated temperature deformation in terms of threshold stresses and back stresses: a review, Materials Science and Engineering 45(2) (1980) 123-135.

[97] T. Gibbons, The relation between “friction stress” and “flow stress” in a complex alloy with good creep resistance, Scripta Metallurgica 12(9) (1978) 749-751.

[98] W. Evans, G. Harrison, Power law steady state creep in α/β titanium alloys, Journal of Materials science 18(11) (1983) 3449-3455.

[99] R. Lagneborg, B. Bergman, The stress/creep rate behaviour of precipitation-hardened alloys, Metal Science 10(1) (1976) 20-28.

[100] Y. Li, T.G. Langdon, A simple procedure for estimating threshold stresses in the creep of metal matrix composites, Scripta materialia 36(12) (1997) 1457-1460.

[101] H. Wang, A. Dhiman, H.E. Ostergaard, Y. Zhang, T. Siegmund, J.J. Kruzic, V. Tomar, Nanoindentation based properties of Inconel 718 at elevated temperatures: A comparison of conventional versus additively manufactured samples, International Journal of Plasticity 120 (2019) 380-394.

[102] S. Ghorbanpour, M.E. Alam, N.C. Ferreri, A. Kumar, B.A. McWilliams, S.C. Vogel, J. Bicknell, I.J. Beyerlein, M. Knezevic, Experimental characterization and crystal plasticity modeling of anisotropy, tension-compression asymmetry, and texture evolution of additively manufactured Inconel 718 at room and elevated temperatures, International Journal of Plasticity 125 (2020) 63-79.

[103] A.K. Mukherjee, An examination of the constitutive equation for elevated temperature plasticity, Materials Science and Engineering: A 322(1-2) (2002) 1-22.

[104] T.G. Gallmeyer, S. Moorthy, B.B. Kappes, M.J. Mills, B. Amin-Ahmadi, A.P. Stebner, Knowledge of process-structure-property relationships to engineer better heat treatments for laser powder bed fusion additive manufactured Inconel 718, Additive Manufacturing 31 (2020) 100977.

[105] S. Zhang, X. Lin, L. Wang, X. Yu, Y. Hu, H. Yang, L. Lei, W. Huang, Strengthening mechanisms in selective laser-melted Inconel718 superalloy, Materials Science and Engineering: A 812 (2021) 141145.

[106] G. Webster, B. Piearcey, An interpretation of the effects of stress and temperature on the creep properties of a nickel-base superalloy, Metal Science Journal 1(1) (1967) 97-104.

[107] D.-H. Kim, J.-H. Kim, J.-W. Sa, Y.-S. Lee, C.-K. Park, S.-I. Moon, Stress rupture characteristics of Inconel 718 alloy for ramjet combustor, Materials Science and Engineering: A 483 (2008) 262-265.

[108] Z. Xu, C. Hyde, C. Tuck, A. Clare, Creep behaviour of inconel 718 processed by laser powder bed fusion, Journal of Materials Processing Technology 256 (2018) 13-24.

[109] W. Chen, M. Chaturvedi, Dependence of creep fracture of Inconel 718 on grain boundary precipitates, Acta materialia 45(7) (1997) 2735-2746.

[110] M.E. Kassner, Fundamentals of creep in metals and alloys, Butterworth-Heinemann2015.

[111] A. Thomas, M. El-Wahabi, J. Cabrera, J. Prado, High temperature deformation of Inconel 718, Journal of materials processing technology 177(1-3) (2006) 469-472.

CHAPTER 3:

Fracture toughness of multi-layer Cu/TiN and Al/TiN nanocomposites: Modeling for geometry factor of micro single edge notched bend specimens

This chapter will be submitted to Journal of Materials Research as: “Fracture toughness of multi-layer Cu/TiN and Al/TiN nanocomposites: Modeling for geometry factor of micro single edge notched bend specimens,” Shubhrodev Bhowmik, Daniel J. Savage, Cayla Harvey, Nathan A. Mara, Amit Misra, Johann Michler, Siddhartha Pathak, Marko Knezevic.

In this work, I performed all the simulations in Abaqus and carried out analysis of data. The text was written under the guidance of Dr. Marko Knezevic and other co-authors.

Fracture toughness of multi-layer Cu/TiN and Al/TiN nanocomposites: Modeling for geometry factor of micro single edge notched bend specimens

Shubhrodev Bhowmik [a], Daniel J. Savage [a, g], Cayla Harvey [b], Nathan A. Mara [d], Amit Misra [e], Johann Michler [f], Siddhartha Pathak [c], Marko Knezevic [a,‡]

[a] Department of Mechanical Engineering, University of New Hampshire, Durham, NH 03824, USA

[b] Chemical and Materials Engineering Department, University of Nevada, Reno, NV 89557, USA

[c] Department of Materials Science and Engineering, Iowa State University, IA 50014, USA

[d] Department of Chemical Engineering and Materials Science, University of Minnesota, Minneapolis, MN 55455, USA

[e] Department of Materials Science and Engineering, University of Michigan, Ann Arbor, MI 48109, USA

[f] Empa, Swiss Federal Laboratories for Materials Science and Technology, Laboratory for Mechanics of Materials and Nanostructures, CH-3602 Thun, Switzerland

[g] Materials Science and Technology Division, Los Alamos National Laboratory, Los Alamos, NM 87545, USA

Abstract

This paper determines the shape functions and their applicable limits to estimate fracture toughness of multi-layer metal-ceramic Cu/TiN and Al/TiN nanocomposites within the realm of linear elastic fracture mechanics (LEFM). A set of finite element method (FEM) simulations in Abaqus are performed to determine the shape functions while taking into account the effects of the geometry utilized in the micro single edge notched bend (MSENB) specimens, the cono-spherical indenter stress field, and the phase interface shielding/anti-shielding on the crack tip driving force. The simulations reveal that the design of specimen geometry against bending moment variation is

* Corresponding author at: University of New Hampshire, Department of Mechanical Engineering, 33 Academic Way, Kingsbury Hall, W119, Durham, New Hampshire 03824, United States. Tel.: 603 862 5179; fax: 603 862 1865.

E-*mail address*: marko.knezevic@unh.edu (M. Knezevic).

fundamental for successful MSENB testing and a clamped beam configuration is advantageous. K_I results are presented for several Cu/TiN and Al/TiN nanocomposites varying in their layer thickness and at different temperatures. Analyses of the results suggests that adding either Al or Cu nanolayers to TiN nanolayers does not weaken or significantly improve fracture toughness relative to the single TiN thin film.

Keywords: Fracture toughness; Geometry factor; Micromechanical testing; Metal-ceramic composites; Finite element method

1. Introduction

Microscale testing of fracture behavior can reveal grain scale fracture properties and enable determining fracture properties of materials with limited size (e.g. thin films, carbon nanotubes (CNTs), nano-composites, integrated circuits) [1,2]. To this end, there has been significant efforts to standardize microscale tests such as the micropillar split test and the microcantilever beam[3] test. Parametric finite element (FE) modeling of the tests has been used to understand the sensitivity of the fracture estimate to geometry and experimental methods. In this work we explore using a micro single edge notched bend (MSENB) specimen. The macroscale single-edge notched bend (SENB) specimen is commonly used to measure mode I fracture toughness, and its experimental geometry is favorable for miniaturization and loading using a nano indenter in a scanning electron microscope (SEM). The geometry and loading effects at the macroscale have been thoroughly standardized via the aid of numerical modeling [4]. In particular, for SENB test to be valid, the following criteria must be met; exact sample dimensions (having a beam length, S more than 4 times of width, W, minimum radius, R of wedge shape indenter should be one eighth of W, and $1 \leq \frac{W}{B} \leq 4$, where B is the thickness), and crack lengths (a) should be such that the $\frac{a}{W}$ ratio should be between 0.45 and 0.70, and using roller type supports/indenter. In the MSENB testing, experimental limitations such as the alignment of the loading device, the ability to pre-fatigue, microstructural effects, and the geometry limitation from manufacturing process introduce many nonstandard components. Furthermore, the composite layered structure studied here makes the extraction of fracture toughness non-standardized due to material interfaces introducing shielding and anti-shielding effects[5]. Thus, it is necessary to model the MSENB tests to understand the combination of these effects on fracture toughness measurements. In addition to SENB, Mishra et al.[6] have recently obtained the geometric factor for the single-edge clamped notched bend (SECNB) specimen, which in addition to the SENB geometric factor will be compared with the modeling results of this work.

Thin films are used in industries to make devices like liquid crystal displays and organic light emitting diodes[7]. They are also used to make super hard wear resistant coatings to make modern cutting tools and biomedical implants [8, 9]. To design reliable devices and cutting tools mechanical properties such as elastic modulus, hardness, strength, wear resistance and fracture toughness are important for thin films. However, toughness is particularly microstructure

dependent property. The grain sizes of thin films are usually on the order of 1 μm or less for a film thickness of 1 μm or less. The available toughness of conventional specimens is of the order of tens and hundreds of millimeters with grain size higher than 1 μm [10]. Because of extrinsic (smaller is stronger[11, 12]) and intrinsic (Hall-Petch like effects[13]) size effects, bulk specimens will either overestimate or underestimate the fracture toughness of thin films. To solve this issue, microscale fracture toughness tests are being performed with different techniques such as controlled buckling[10] and nano-indentation[14-16]. For various functions such as scratch resistance, anti-reflection, modifying the weak interfaces for crack deflection, and introducing compressive stress to outer layer[17] multiple layers of thin films are coated[10] and one type of such structure is multilayered composite.

In addition to films, composite materials are made by using two or more materials with the purpose of achieving better performance than the individual component alone. To maximize the performances, harder, stiffer, and stronger material than a selected matrix is typically used [18]. Since composite materials are widely popular in sectors like automobile, aerospace, and nuclear, the fracture behavior is of great importance in designing structures containing composites in critical load bearing regions. Several studies are being performed to extract the fracture toughness of different types composites like fiber (i.e. carbon fiber, glass fiber) reinforced, particle (i.e. carbon powder, ceramic powder) reinforced, and structural (i.e. laminates, sandwich panels) composites. For example, Herráez et. al. performed tensile tests on straight-fronted edge notched specimens to fine the toughness of structural fibers for composite materials [19]. Moreover, Wang performed 3-point bend tests on a sandwich panel to get interlaminar fracture toughness for fiber-reinforced composite materials [20], and similar studies [21-23] have been performed on different types of composites. However, most of the tests are at the macroscale even though obtaining microscale properties is often important to successfully predict the fracture toughness of such components.

Micro multilayered laminated nanocomposites are another class of materials that can be created by accumulative roll bonding [24, 25]. Such materials are usually first explored using physical vapor deposition (PVD). Reliable extraction of fracture toughness of multilayered nanocomposite material systems is an outstanding problem. This paper is a contribution in terms of determining fracture toughness of multilayered nano composites created by PVD using MSENB test specimens. 3-point bend tests were performed by Sidharth et. al. on notched specimens of laminated

nanocomposites made by metals (Al or Cu) and ceramics (TiN) at different temperatures (Figure 1c). The thin film layers were deposited on Si substrate by PVD and by using Focused Ion Beam (FIB) the sample for 3-point bend tests were made (Figure 1a). The notch was also introduced by FIB. These micro-mechanical experiments depart from the ASTM standard in several aspects pertaining to the setup: cono-spherical indenter instead of a spherical wedge indenter was used, pre-cracking of the notch by fatigue for sharpness was not performed, and legs instead of support rollers were used [4]. Moreover, interface rich microstructure made up of metal/ceramic layers induces stress shielding/antishielding around the crack tip[5]. Considering all these aspects, the equations provided by ASTM[4] for a SENB specimen to calculate the geometric factor and, ultimately, K_{IC} are not valid. The motivation of this study is to find equation for geometric factor which will account for these external effects [6]. Relying on the linear elastic fracture mechanics (LEFM), beam theory for composites, interface effects on the crack tip driving force, and the finite element method (FFEM), we evaluate local fields of stress at crack tip locations to determine polynomial fits for the geometric factor, f. To this end, different crack lengths, a, were considered such that 3-5 data points were acquired for crack tip in both metal (Al or Cu) and ceramic (TiN) layers for a given geometry. Afterward, f was plotted as a function of normalized crack length α (where $\alpha = \frac{\mathrm{a}}{\mathrm{W}}$) and a third order polynomial equation was used to fit the points. Subsequently, fracture toughness values for Cu/TiN and Al/TiN multilayers with different layer thickness at several temperatures were estimated. In doing so, the model geometries and the nano-indenter were consistent with the experiments as measured using SEM. The effects of geometry, indenter stress fields, and layer shielding on the fracture toughness estimates are particularly studied. The J and interface integrals are used to isolate the effect of indenter stress field and give insight into the effectiveness of the material systems at preventing crack propagation. We find the leg geometry is significant in MSENB and show that changes in bending moment are responsible for the apparent increase in fracture toughness with decreasing crack ligament length. The design of geometry against bending moment variation is discussed as fundamental for MSENB standardization at small length scales.

In the following sections, the effects of geometry, indenter stress field, and crack tip shielding on the fracture toughness estimates are studied. In section 2, we describe the finite element model, LEFM, and beam theory for composites used to determine polynomial fits for the

geometric factor, f. In section 3 the J and interface integrals are used to generate the geometry factors, isolate the effect of indenter stress field and present fracture toughness as a function of layer size and temperature. In section 4, we discuss the effectiveness of the material systems at preventing crack propagation and the design considerations for MSENB style specimens. Finally, we conclude in section 5 summarizing our findings.

a

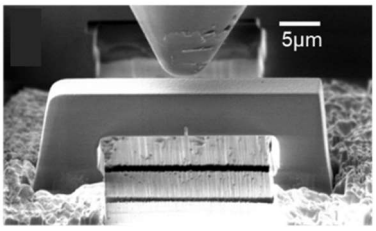

b

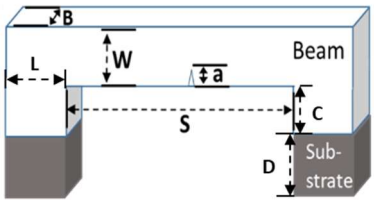

c

	Layer Thickness (nm)	Temperatures
Cu/TiN	50/50, 5/5	100°C (0.27T_m)
		200°C (0.35T_m)
Al/TiN	50/50, 5/5	60°C (0.36T_m)
		100°C (0.39T_m)

Figure 14. a) An SEM image of the FIB fabricated MSENB; b) a schematic showing important beam dimensions: B is the thickness, a is the crack length, W is the width, and S is the length of the inner beam dimension; c) layer thicknesses and temperatures for Cu/TiN and Al/TiN composites.

2. Modeling methodology and calculation of K_I

2.1 Model description

Extraction of the shape functions, their applicable limits, and K_I from the experimental geometries was performed using the commercially available Abaqus finite element software. The model geometries and the indenter were set to match the experimental geometries as measured

using SEM. Symmetry of the specimens in the x-direction was exploited to obtain half (H) models (Figure 2a). Indenter was always set to be centered along x-direction and allowed to vary in z-direction based on experimental measurements. To evaluate the importance of indenter position, the measured location in z (H-models) and the middle location in z (Quarter (Q) models) were both simulated. The effect on load vs displacement is provided in Figure 2d. Since the effect on the load versus displacement is small, Q- models with symmetry in the z and x directions under the indenter are adopted in this study. The geometric factor and reported K_I utilize Q models, wherein the applied z-direction symmetry fully centers the indenter in x and z on the specimen Figure 2a.

Table 7. Dimension of simulated beams. Here, E is the position of indenter along z axis, which was used to perform simulations with half models. The simulations for 5-5 nm cases were not performed with half models because of computational limitations.

Simulated beam	B	W	S	L, μm	C, μm	D, μm	E, μm
Al-TiN-60^{0}C-50-50 nm	5.543	6.028	23.960	3.890	3.520	6.540	1.93
Al-TiN-100^{0}C-50-50 nm	5.150	5.888	25.170	2.800	3.980	4.110	2.03
Cu-TiN-100^{0}C-50-50 nm	4.675	6.407	23.550	2.800	4.280	5.150	1.84
Cu-TiN-200^{0}C-50-50 nm	4.850	7.078	23.765	2.800	3.875	4.460	2.20
Al-TiN-60^{0}C-5-5 nm	5.543	6.028	23.960	2.800	3.620	6.550	Simulations with half model were not performed
Cu-TiN-100^{0}C-5-5 nm	5.410	7.0356	24.190	2.800	3.340	4.220	

The substrate leg was modeled consistent with measurements, and its dimensions given in Table 1 were taken as the average over the experimental geometries performed in each category.

The S, W, and B dimensions of simulated beam are also provided in Table 1. Since the *J*-integral represents an energy release rate at a point in a layer and the layer interfaces introduce shielding and anti-shield effects, the K_I estimate varies with the material in which the crack tip resides and with the distance to the interface in front of the crack tip. Experimentally the crack tip position is observed to zigzag in the x-direction as the crack propagates in the y-direction. Thus, the driving force for the crack tip in the presence of material inhomogeneities such as grain boundaries and interfaces play some role in the toughness. In addition, there is possible influences from the indenter stress field which will be studied in section 3.2. The layers are approximated as homogenous in terms of their thickness with no effects of grain boundaries. For convenience in meshing, the crack tip was placed in each material at the center of the layers nearest the measured experimental crack tip y-position (see Figure 2c). While this arbitrary choice of crack position in the layer influences the magnitude of K_I that we compute, the relative effects of temperature and material choice can be studied.

Given the elastic deformation and the sensitive numerical integration used in determining K_I through the *J*-integral, full-integration quadratic hexahedron elements (C3D20) were utilized. Following standard practice, collapsed edge, wedge elements (See Figure 2c) were used to achieve a sharp crack tip with stress concentrations of $1/r$ for a side node and $1/\sqrt{r}$ for a corner node [26]. The wedge elements also allow a highly structured mesh near the crack-tip to be achieved. The indenter was modeled as an analytically rigid surface, and hard, frictionless contact was used for the interaction properties. The quality of the mesh design shown in Figure 2b and c was evaluated in two ways. First, the density of the mesh under the indenter was studied by reproducing the Hertz analytical solution of spherical indentation of an elastic half space. The density of the mesh shown in Figure 2b exceeds that required to reproduce the Hertz theory within 1% error in pressure profile, load, and max stress (see appendix). Secondly, the effects of increasing the number of elements through layer thickness, around the crack tip, and the meshing biasing along the model were evaluated using the change in *J*-integral as the convergence metric. The converged meshes were utilized in the calculations.

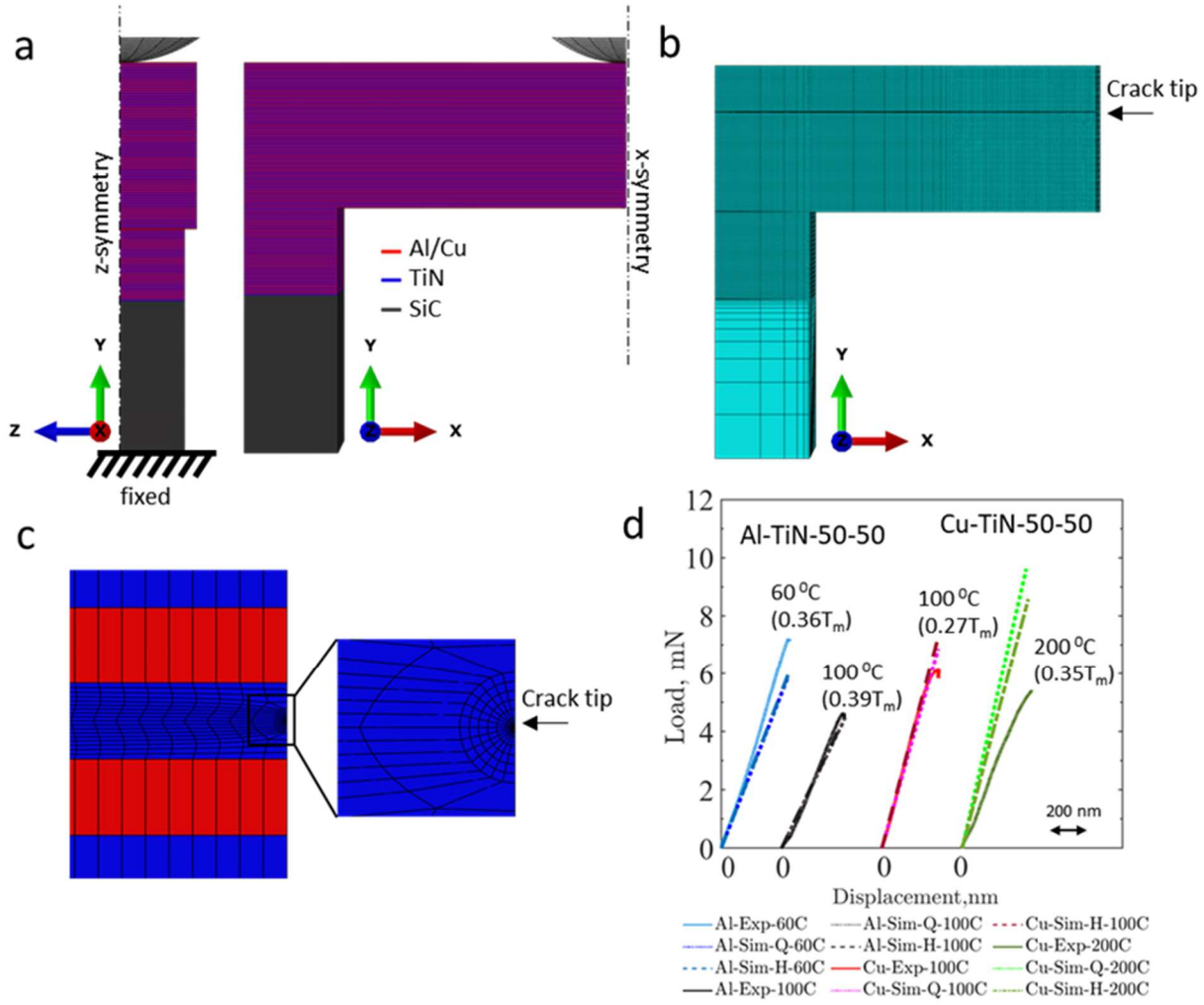

Figure 15. The typical model setup for 50 nm-50nm multilayers highlighting (a) the symmetry, boundary conditions, geometry, and layer structure; (b) the macroscopic brick element mesh design; (c) the mesh design near the crack tip; (d) comparison of measured (Exp.) and simulated (Sim.) load vs displacement curves where 200 nm is the scale bar along x-axis. The simulation results are based on half (H) and quarter (Q) models.

The material behavior of TiN, Al, and Cu layers is approximated as linear elastic with no plasticity; thereby, allowing the relationship between load and stress intensity K_I to be determined shortly after contact initiates. The elastic properties of TiN vary widely in literature due to the quality of the films. In addition, Cu and Al exhibit temperature dependent elastic properties. The elastic properties shown in Table 2 were taken from literature[27, 28] and adjusted using the

experimental geometry to better reproduce the load displacement of the experiments as demonstrated in Figure 2d. For Al-TiN (60 °C and 100 °C) and Cu-TiN (100 °C) 50-50 nm layer cases matches with the experimental curve. We hypothesize that the Cu-TiN (200 °C) 50-50 nm load vs displacement curve could not be matched properly due to neglecting plasticity effects.

Table 8. Summary of elastic properties used in the simulations.

	Al		Cu		TiN	Si
Temperature (°C)	60	100	100	200	All	All
$E\ (GPa)$	60	50	115	100	380	130 [29]
ν	0.3					

2.2 Calculation of J-integral

The *J*-integral in three dimensions represents the point-wise energy release rate along the crack front in the crack propagation direction y (2 if using the indicial notation). For the model geometry shown in Figure 2, the crack front is centered under the indenter, and does not vary in position in x or y for a given crack tip position. We observed that the *J*-integral does not vary substantially except at the free surface – expected in 3D analysis [26] – and can readily be approximated using the plane-strain relationship of

$$K_I = \sqrt{\frac{EJ}{1-\nu^2}} \tag{1}$$

where E and ν are the young modulus and Poisson's ratio of the material layer with the crack tip. This plane-strain observation despite using the cono-spherical indenter is important, since it allows a simple conversion between *J*-integral and K_I, while limiting the effects of contact alignment that would undoubtedly be introduced by a wedge indenter.

The *J*-integral and its numerical implemented using the virtual crack tip displacement method has been thoroughly studied in [26, 30, 31]. The favorable methodologies of [31] were used for

the classical *J*-integral and the formulation of material force C_{int} in the interfaces derived in [5] was adopted with minor changes in numerical integration.

For completeness, we briefly summarize the 3D *J*-Integral as implemented in this study. The *J*-integral over a volume at a position s along the crack-front is

$$J_2(s) = \frac{\bar{J}_2}{\int_{L_c} l_2(s) v_2(s) ds} \tag{2}$$

where the volume average of J_2 over a crack segment L_C is:

$$\bar{J}_2 = \int_V (\sigma_{ij} u_{j,2} - W \delta_{i2}) q_{2,i} dV \tag{3}$$

and the integral $\int_{L_c} l_2(s) v_2(s) ds$ represents the weight of $J_2(s)$ in the crack propagation direction v_2 as described by the function $l_2(s)$. In practice, the *J*-integral is easily evaluated at nodes along the crack front and $l_2(s)$ is chosen to be linear and described using shape functions of neighboring elements, thereby allowing the integral to be performed exactly using a one-point quadrature. The calculation of Eq. (3) requires the Cauchy stress $\boldsymbol{\sigma}$, the gradient of displacements $\mathbf{u}$, the strain energy $W_i = \frac{1}{4}\sigma_{ij}(u_{j,k} + u_{k,j})$, and the gradient of a scalar function q_2, which is known at quadrature points. This is achieved by interpolating nodal quantities $\mathbf{u}$ and q_2 to gauss points using shape functions. Calculation of $\bar{J}_2(s)$ is best performed from regions where the mesh quality is high, structured, and away from the crack tip [31]. Taking advantage of the path independence of the *J*-integral within a layer, element sets for Gaussian quadrature were constructed in concentric rings about the crack front in the x-y plane and q_2 was appropriately chosen to vary from 1 to 0 across the outer ring of elements in the set of interest [26]. Since Eq. (3) depends on the gradient of q_2 the integral only considers the region from which q_2 varies. For the calculation in this paper, the *J*-integral is evaluated directly under the indenter and as shown in Figure 2c, highly structured rings of elements were put in the layer with the crack tip, allowing an appropriate evaluation of the *J*-integral which we call J_{tip}.

Should the domain of the *J*-integral described in Eq. (3) include an inhomogeneity such as a sharp interface, the material force at the interface Σ can be accounted for such that

$$\bar{J}_{tip} = \bar{J}_2 + \bar{C}_{int} = \int_V (\sigma_{ij} u_{j,2} - W \delta_{i2}) q_{2,i} dV + \int_\Sigma (\sigma_{ij} u_{j,2} - W \delta_{i2}) l_2 z_2 dS \tag{4}$$

where, z_2 is the unit surface normal of the interface [5]. The calculation of $\bar{C}_{int}$ was performed using a 3x3 quadrature rule and Eq. (4) is numerically carried out as:

$$\bar{J}_{tip} = \sum_{\substack{\text{all} \\ \text{elements} \\ \text{in V}}} \sum_{p=1}^{27} \left\{ \left(\sigma_{ij} \frac{\partial u_j}{\partial x_2} - W \delta_{2i} \right) \frac{\partial q_2}{\partial x_i} det(\mathbf{J}) \right\}_p w_p +$$

$$\sum_{\substack{\text{all} \\ \text{interfaces} \\ \text{in V}}} \sum_{p=1}^{9} \left\{ \left(\frac{\left(\sigma_{ij}^{+} + \sigma_{ij}^{-}\right)}{2} \left(\frac{\partial u_j^{+}}{\partial x_2} - \frac{\partial u_j^{-}}{\partial x_2} \right) - (W^{+} - W^{-}) \delta_{2i} \right) l_2 z_2 \, det\left(\mathbf{J}_{surface\ element}\right) \right\}_p w_p \quad (5)$$

where $\det(\mathbf{J})$ and $det\left(\mathbf{J}_{surface\ element}\right)$ are the jacobians mapping the integral from global to natural coordinates and the $+$ and $-$ superscripts denote values interpolated from gauss points above and below the interface, respectively. The validation of Eq. (5) was performed by reproducing analytical solution for a through crack in an infinite plate and the interface implementation is readily verified since J_{tip} should not change when the *J*-integral Eq. (5) is performed across an interface.

We note that the magnitude of the *J*-integral will increase or decrease as the crack tip approaches an interface, depending on the (anti)-shielding effects. The *J*-integral saturates by the third ring of elements, which is by design completely inside a layer. Therefore, for the purpose of constructing the geometric factor Eq. (2) is sufficient. However, there are three advantages to calculating $\bar{C}_{int}$: 1) The interaction of the *J*-integral domain with the stress field of the indenter can be studied, 2) the magnitude of $\bar{C}_{int}$ gives a sense of the importance of interfaces and whether the interface shielding effects are a function of layer geometry, and 3) the spatial distribution and sense of shielding and anti-shielding of layers can be studied.

2.3 Calculation of geometric factor, f

The mode I stress intensity factor for a through crack in an infinite plate is

$$K_I = O\left(\sigma\sqrt{\pi \mathrm{a}}\right), \quad (6)$$

where the $\sqrt{\mathrm{a}}$ is the characteristic length scale of the crack and σ is the tensile stress field at the crack tip causing the crack to open. A dimensionless function representing the geometry and mode of loading can be introduced to scale the local stress state. Key to the dimensionless function

identification is a constant moment for a give value of S. The geometry of Figure 1 is not standardized and may be analogous to a fixed beam, a simply supported beam, or a combination which do not have the same moment as a function of normalized crack length $\alpha = \frac{\mathrm{a}}{\mathrm{W}}$.

Adopting the convention from [32] for the SENB specimen, we can write Eq. 6 as

$$K_I = \frac{\sigma_0\sqrt{\pi \mathrm{a}}}{(1-\alpha)^{3/2}} f(\alpha), \tag{7}$$

Where,

$$\sigma_0 = \frac{6M}{\mathrm{BW}^2}, \tag{8}$$

is the max tensile bending stress in a smooth, uncracked specimen (bottom of beam), $M = \frac{PS}{4}$ is the bending moment because of the load P at the center of a simply supported beam, and $f(\alpha)$ is the dimensionless stress intensity factor (geometric factor). Note, that f represents a change in the local stress at the crack tip compared to the maximum tensile stress in an uncracked beam. In the case of single edge notched clamped bending specimen (SENCB) [6] specimen Eq. (7) remains the same except the moment becomes $M = \frac{PS}{8}$ due to the fixed beam configuration. This change in moment was not taken into account in [6] and is generally embedded in f. The relationship between P and K_I should also take $\frac{\mathrm{a}}{\mathrm{W}}, \frac{\mathrm{S}}{\mathrm{B}}, \frac{\mathrm{S}}{\mathrm{W}}$ into account if these geometries vary from specimen to specimen.

In [33] it was demonstrated that the effective K_I seen by the composite extracted from the experimental testing using a shape factor was partially consistent with the path independent J_{far} integral. In the case of a composite material with no residual stress field, the path independent J_{far} is calculated by performing the integration across all interfaces such that all contributions of are accounted for. Here the stress-field from the indenter prevents us from evaluating J_{far} in this manner; however, one might argue for small loading and when far enough from the indenter that a path independent J_{far} can be appropriately obtained (see Figure 4). The magnitudes of J_{far} and J_{tip} can also be dramatically influenced by the presence of residual stress and thermal stresses[33]. We choose to focus on the value of J_{tip} which is the local crack driving force in the composite layer with the crack tip. Leveraging the observation that $J_{tip} > J_{far}$ in anti-shielding, we can conveniently provide an upper estimate for the effective driving force of a crack tip in the center of a TiN layer. To obtain comparable geometric factors, the bend stress σ_0 in the uncracked

composite needs to be appropriate in terms of the layered geometry and material properties. In practice, the shielding effects will make a single geometric factor unobtainable without averaging.

The bending stress in Eq. (8) can be written in the general form as

$$\sigma = -\frac{My}{I} \tag{9}$$

where y is the distance of the layer from the neutral axis and I is the moment of inertia about the neutral axis. For a single-phase material, the maximum tensile stress in each phase is at $\mathrm{y} = -\frac{\mathrm{W}}{2} + \mathrm{y}'$, where y' is the distance to the center of the layer from the bottom of the beam.

In the case of a 2-phase, layered composite, elementary beam theory gives the bending stress for each phase as

$$\sigma_X = \frac{-MyE_X}{E_X I_X + E_{TiN} I_{TiN}} \text{ and } \sigma_{TiN} = \frac{-MyE_{TiN}}{E_X I_X + E_{TiN} I_{TiN}} \tag{10}$$

where X is either Al or Cu. The neutral axis is defined by both phases and the individual area moment of inertia are provided using the parallel axis theorem and can be written in terms of the number of bilayers, n, in the composite. If the number of bilayers is greater than ~50 in a given W, a general expression can be obtained as a function of W, n, E_X, and E_{TiN}. To visualize the effect of the number of layers we defined the ratio of bending stress $r = \sigma_{TiN}/\sigma_X$ and provided the plot in the appendix. The predicted stresses from Eq. (10) are consistent with those found by FEM. In this study we evaluated Eq. (10) numerically so there is no approximation, but a general solution can be extracted.

Using Eqs. (7) and (10), the polynomial form for the geometric factor can be fit. To achieve that for a composite material, different crack lengths a where considered such that 3-5 data points of K_I are acquired for crack tip in both metal (Al or Cu) and ceramic (TiN) layers for a given geometry. Afterward, f was plotted as a function of normalized crack length α and a third order polynomial equation was fit. From the fitted geometric factor, K_I can be calculated for the array of experiments.

3. Results

3.1 Geometry factor, f

From Figure 2d, it can be observed that the half and quarter models give similar load vs displacement curves. Considering $K_I \propto P$ and the geometry is constant one can infer that the quarter model is appropriate despite misalignments in indenter position in the z-direction up to 30%. The error with the experimental and simulated curve is within 5% for all the cases except Cu-TiN (200 °C) 50-50 nm which is ~9% error within the region where the experimental curve shows linearity. This outlier had substantially larger Si legs (31% larger than the mean used for the modeling). We observed in modeling of long supporting legs that the legs have a tendency to bend outward. This causes the beam to rotate at the ends and lowers the force seen by the indenter for a given displacement. The role of plastic deformation may also be non-negligible in the observed nonlinearity; however, to appropriately partition effects of plasticity and elasticity for nanolayered materials is non-trivial. The results in this Section 3 are given for the quarter model since the load vs displacement curves are found to be reasonably close to the half model which employed the experimentally measured indenter position.

To investigate the potential to use a single geometric factor for the Al/TiN and Cu/TiN we employ eq. (7) and (10) and fit geometric factors for crack tips in each of the material systems. The polynomial fit employed here is

$$F(\alpha) = c_0 + c_1\alpha + c_2\alpha^2 \tag{11}$$

and the coefficient c_i are summarized in Tables 3 and 4 for the experimental geometries and loading cases investigated. The R^2 value represents the quality of fit and the third order polynomial shows the lowest R^2 value 0.97 which is regarded as good. Notably each specimen has a different $\frac{S}{W}$ ratio varying across the cases up to 21% and it is expected based on the work of [6] and [32] to have some influence on the geometric factor. In particular, it is expected that a lower $\frac{S}{W}$ ratio will have lower geometric factor all other geometry equal.

In addition to geometric variation, one must consider the effects of the number of bilayers in the ligament ahead of the crack since we are considering 5nm and 50nm layer sizes in the same W. When the number of layers is large, a single effective stress ratio is calculated using Eq. (10) and the crack ligament length will not affect the ratio of bending stress; however, the ratio of the

bending stress changes substantially when the number of bilayers is less than 50 as showed in the appendix. The 50/50 nm composite consists approximately of 60 bilayers and at an $\frac{a}{W}$ of 0.79 only 13 layers remain. This introduces approximately 12% change in the bending stress ratios due to change in the number of layers. This variation will not be present for the 5/5nm composite. Based on this observation we expect the geometric factor for crack tip in TiN layer to have a different geometric factor than crack tip in Al or Cu layer at $\frac{a}{W}$ greater than 0.5. However, there is roughly a 30% difference for $\frac{a}{W}$ less than 0.5, far more than the error introduced by reduction in the number of layers. Here asymmetry in (anti)-shielding effects in J_{tip} are manifested[5].

As mentioned, leg geometry may play an important role in the load displacement response and therefore the bending moment experienced by the beam. The maximum bending moment for beams with simply supported ends is $M = \frac{PS}{4}$ and is appropriate for the SENB specimen. The maximum bending moment for clamped SENCB specimen is $M = \frac{PS}{8}$. The geometry may not be simply supported since the legs will introduce a restoring moment. The close correlation between the geometric factor calculated for each phase and that for SENCB does indicate that the clamped beam analog is appropriate, though the magnitude may be coincidental given J_{tip} is used with the crack tip in the middle of the layer. One obvious concern would be that as the ligament size changes, the moment changes from a simply support to a clamped beam. Such a transition would indicate the geometric factor is a function of the leg rigidity. To test this, the moment on the ligament is calculated numerically in Abaqus for a crack tip in TiN layer at an $\frac{a}{W}$ of 0.52 and 0.69. In the former case the beam moment is consistent with a simply supported beam while for the latter the beam is close to fixed. This finding explains why load increases substantially in the load vs displacement curves during the experiments (Figure A1 – Figure A4 in the appendix), but the crack driving force remains approximately constant (Figure 3). The changes in moment will also result in unloading the crack tip which will arrest a crack after a large unstable crack growth event. Clearly, the effects introduced by leg geometry are substantial and the leg geometry needs to be designed for a single geometric factor to be utilized. The practical implications are that changes in leg length and width and especially the stiffness of the composite, will have a substantial impact on the geometric factor in the range of $\frac{a}{W}$ studied in Al/TiN and Cu/TiN experiments.

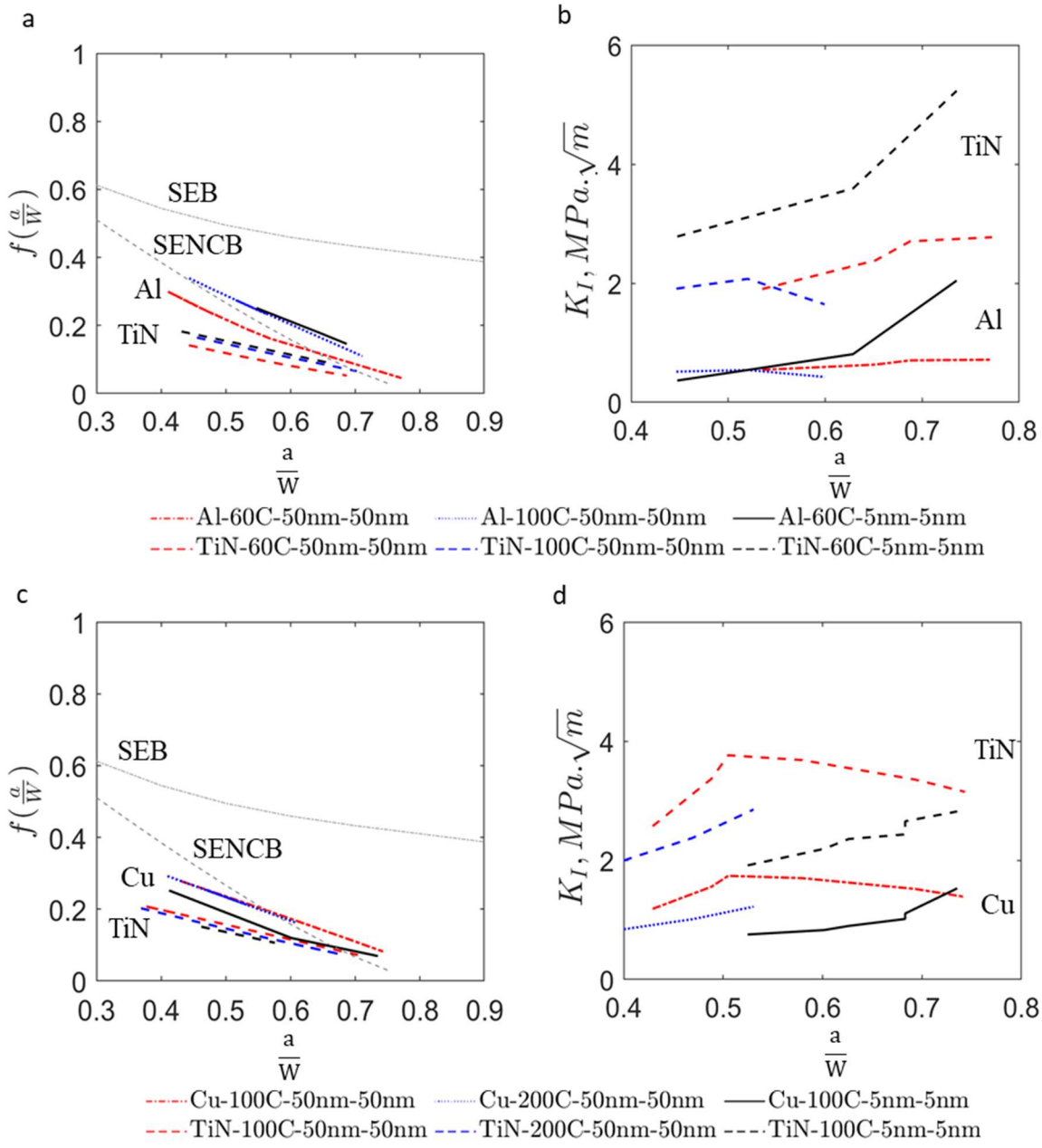

Figure 16. (a) and (c) are a comparison of geometric factors for different experimental geometries and depend on the phase the crack tip is in (the legends specify the phase in which the crack tip is). (b) and (d) are a comparison of the mode I stress intensity factor, K_I, shown as a function of crack growth by using the corresponding model geometric factors and the experimental load (Table A3 – Table A6 in the appendix) and measured crack length (Table A1 and A2 in the appendix). The curve for SECB is generated by taking the values from Mishra et. al., 2020 for S/W = 4[6]. The 60°C Al-TiN-50-50-nm and 100°C Cu-TiN-50-50nm shape factors do vary substantially, suggesting that geometry standardizing and the repeatability of the FIBing process is critical. The

upward trends are with the expected range for the beam going from simply supported to fixed beam which is not accounted for in the shape functions.

Table 9. Summary of the polynomial fits to $\frac{(1-\alpha)^{\frac{3}{2}}K_I}{(\sigma_0\sqrt{\pi a})}$ from FE simulations for 50/50 cases for Al-TiN at 60^0C (0.36 T_m) and 100^0C (0.39 T_m), and Cu-TiN at 100^0C (0.27 T_m) and 200^0C (0.35 T_m). Where, σ_0 was calculated by using eq. 10.

S/W	3.97		4.27		3.68		3.36	
Material	Al-TiN 60^0C		Al-TiN 100^0 C		Cu-TiN 100^0C		Cu-TiN 200^0 C	
Crack tip in	Al	TiN	Al	TiN	Cu	TiN	Cu	TiN
c_0	0.85	0.37	0.19	0.27	0.51	0.36	0.54	0.37
c_1	-1.69	-0.62	-1.08	-0.12	-0.50	-0.40	-0.60	-0.50
c_2	0.84	0.23	0.78	-0.27	-0.10	-0.01	-0.05	0.08
σ_0, MPa	97.90	609.70	99.27	741.79	164.40	535.00	122.60	459.50
R^2	0.97	0.99	0.98	0.99	0.99	0.99	1.00	0.99
a/W $range$	0.41-0.77	0.44-0.68	0.34-0.71	0.45-0.70	0.43-0.74	0.37-0.70	0.41-0.61	0.37-0.68

Table 10. Summary of the polynomial fits to $\frac{(1-\alpha)^{\frac{3}{2}}K_I}{(\sigma_0\sqrt{\pi a})}$ from FE simulations for 5/5nm layers. Note: The dimensions of Al-TiN- 60°C (0.36Tm)-50-50 nm case was the same as Al-TiN- 60°C (0.36Tm)-5-5 nm. Where, σ_0 was calculated by using eq. 10.

S/W	3.97		3.44	
Material	Al-TiN 60^0C (0.36 T_m)		Cu-TiN 100^0 C (0.27 T_m)	
Crack tip in	Al	TiN	Cu	TiN
c_0	0.58	0.35	0.78	0.30
c_1	-0.50	-0.39	-1.71	-0.27
c_2	-0.20	-0.006	1.005	-0.11
σ_0, MPa	97.36	615.58	125.81	415.13
R^2	1.00	0.99	1.00	1.00
a/W $range$	0.55-0.69	0.43-0.66	0.41-0.73	0.46-0.58

3.2 Effect of indenter stress field on interface shielding

Experimentally it was observed that as cracks propagated, they would self-arrest as they near the indenter. In Section 3.1 we identified a changed in moment that would promote crack stability[6]. Additional, it is important to understand whether the indenter stress field is changing the (anti)-shielding effects and whether a rule-of-thumb can be identified for the interaction of the indenter stress field and cracktip stress field. To investigate this, a crack tip at a = 3.21 μm in Al and at a = 3.56 μm in TiN was investigated. The *J*-integral was evaluated for these crack tips with concentric sets of elements at a distance d_{top} from the indenter (See Figure 4a). For each interface C_{int} was calculated and summarized in Figure 4c and d. We find for both crack tip locations, that the *J*-integral is affected if the integral is computed within 3.5 times the contact radius (r) of the indenter, obtained from the contact pressure distribution (CPRESS) observed in the simulations (Figure 4b). This is consistent with linear elastic spherical contact theory and is a general rule of thumb in spherical nanoindentation for the interaction zone under the indenter[34, 35].

The change in K_I appears to be tightly linked to the change in interface contribution C_{int} as shown in Figure 4c and d. This reveals that close to the indenter the crack driving force will increase for TiN and decrease for Al. Presumably, the crack tip arrests under the indenter because of the increase in crack tip shielding when the crack tip is in Al or Cu. However, the indenter stress field may also play a role in reducing the tensile stress at the crack tip that is separate from the interface shielding effects. Regardless the rule of thumb provided above can be a useful tool to identify a valid test, provided the experimental contact radius is known.

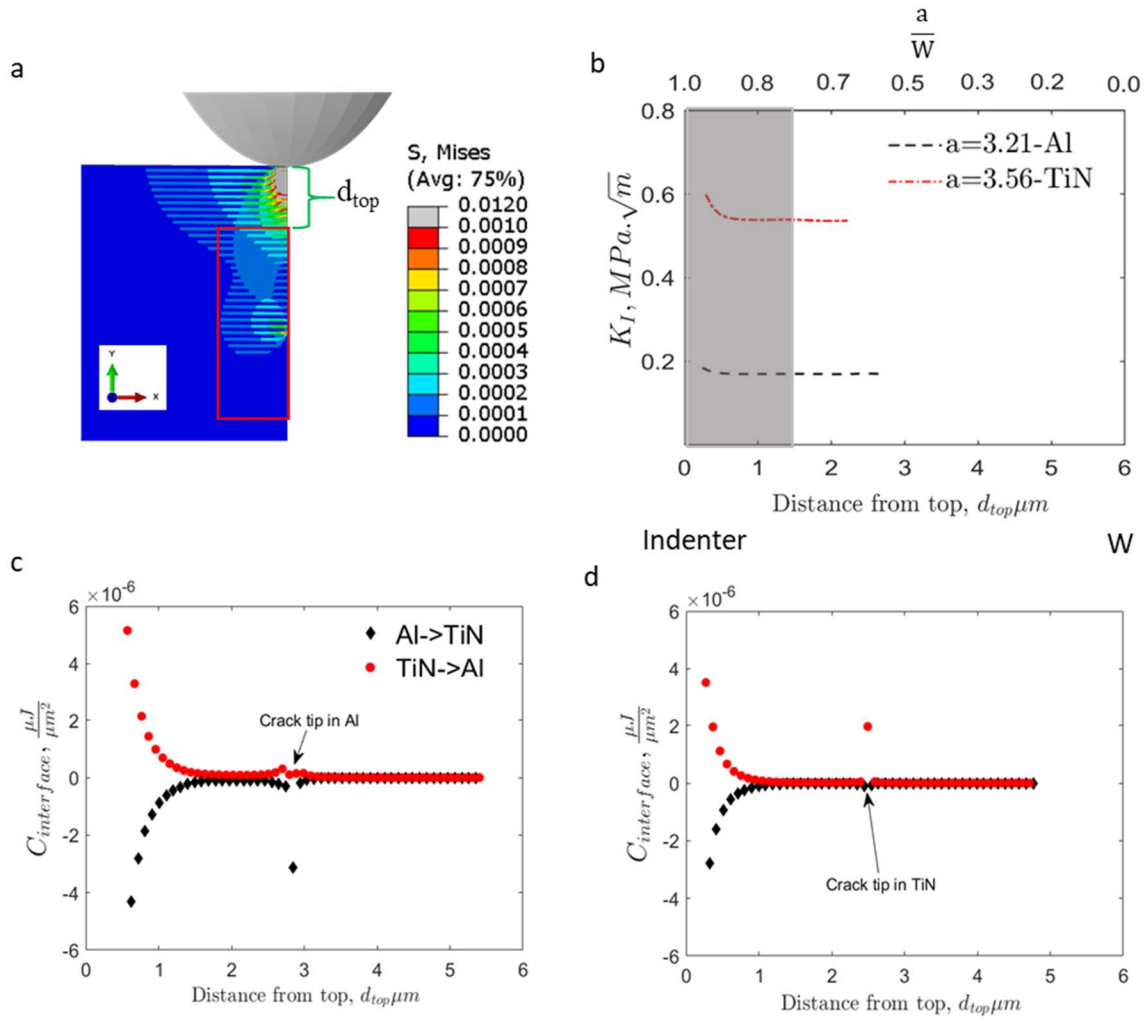

Figure 17. (a) Shows how distance from the top of the specimen is calculated for a given contour set which is shown as a gray box. (b) Effect of calculating K_I based on distance from indenter for crack tip positions in: Al (a = 3.21 μm) and TiN (a = 3.56 μm). The rise in K_I stems from asymmetric shielding antishielding contributions that is driven by a stress field other than the cracktip stress field. (c) The difference in shielding and anti-shielding for stiff/compliant (red) and compliant/stiff (black) layer transitions in the direction of crack propagation. The shaded portion in (b) corresponds to the region to the region where the shielding effects are expected to augment the calculation K_I; suggesting that the *J*-integral should be calculated at least 3.5 indenter contact radius away from the top.

3.3 Temperature and layer effects on K_I

To summarize the K_I for the test suite showed in appendix we elect to use the geometry factor for TiN (meaning using the shape factor when crack is in TiN layer). The motivation comes from the crack presumably being stopped in the Cu or Al layer due to shielding effects. The driving force for TiN predicted using the shape factor and the load will continue to increase until the crack

tip goes through the tough layer. An increase in TiN toughness is not indicative of the TiN layer being very tough, but it is indicative of the effectiveness of the composite to enhance the toughness of TiN i.e., an effective toughness. When the crack tip re-enters the TiN, the layer is presumably overloaded, and the anti-shielding effects will help drive the crack tip through TiN and back into the tough layer. Furthermore, we expect $J_{tip} > J_{far}$ due to anti-shield effects and will extract an upper value. If the TiN K_I is substantially less than the expected K_{IC} for TiN, it is likely being weakened by the anti-shielding effects of the composite and the Al or Cu layer has too low of a fracture toughness to improve the effective fracture toughness of TiN.

In Figure 5, the Mode I stress intensity factor, K_I is shown by using the TiN shape factor obtained for experiments Al-TiN (a, c) and Cu-TiN (b, d). Same tests are used to get multiple points of $\frac{a}{W}$ ratio and load is calculated from the load vs displacement curves as shown in appendix (Figure A1 - Figure A4). The orange color line and arrow show the unacceptable region based on the contact radius rule of thumb identified in Section 3.2. The contact radius is calculated by Hertz equation[34, 35] for contact mechanics. This is not an exact value since the simulation shows elliptical nature of stress field. But this is the best tool we have so far to calculate the contact radius based on experimental results. The dark gray line and arrow represents the unacceptable region by ASTM recommendations which clearly is much smaller than that is observed in this study. Sharp K_I increase in the region after the orange line is noticed for all the cases because of indenter stress interaction. Encouragingly, the K_I results are similar to those observed in literature which is 1.19 to 3.3 MPa $m^{\frac{1}{2}}$ [36-40] . However, we note that an arbitrary choice of crack tip in the middle of the layers and the use of J_{tip} when computing the shape function influence the absolute values of K_I, limiting the comparison.

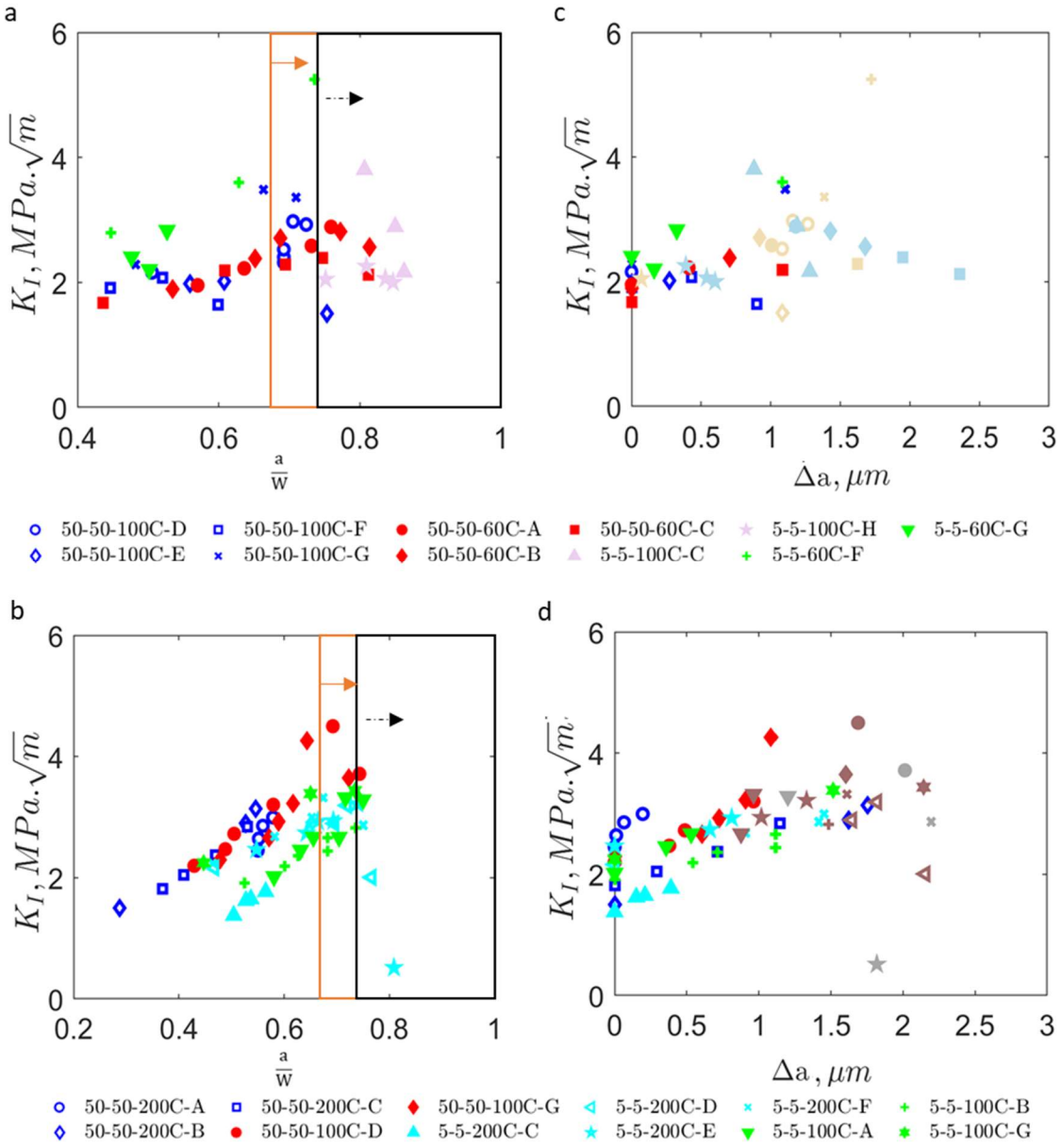

Figure 18. Mode I critical stress intensity factor, K_I, calculated by using the TiN shape factor (meaning shape factor was calculated when crack tip is in TiN layer) obtained for experiments Al-TiN (a,c) and Cu-TiN (b,d). For Figure a and c, the orange color line and arrow indicate the unacceptable region based 3.5r interaction depth observed in this study. The black line and arrow represent the unacceptable region by ASTM recommendations. Moreover, symbols that are yellow /brown or sky color /gray are still meaningful and defined in the legends. The change of color is due to represent the unacceptable region while keeping the symbols from the legends the same. The points with yellow/brown represent that the crack is within the 3.5r interaction depth and sky color/gray points stand for crack position at unacceptable region by both ASTM recommendations

and this study. Note: Multiple experiments were performed and -A, -B, - C, -D, -E, -F, -G in the legend are used to differentiate the tests performed in each temperature and material category.

4. Discussion

The purpose of choosing ductile metal with brittle ceramic to make a layered composite is to use metal's higher intrinsic fracture toughness and shield the crack's driving force when it tries to enter the ductile material. From literature it has been observed that the fracture toughness, K_{IC} of TiN coatings is in the range of 1.19 to 3.3 $MPa.\mathrm{m}^{\frac{1}{2}}$ [36-40]. The K_I calculated by using TiN shape factor from this study (Figure 5) shows that within acceptable region found by this study the K_I varies at the range of 1.674-2.381 $MPa.\mathrm{m}^{\frac{1}{2}}$ for Al-TiN-50-50 nm-60^{0}C, 1.909-2.381 $MPa.\mathrm{m}^{\frac{1}{2}}$ for Al-TiN-50-50 nm-100^{0}C, and 2.792 -3.6 $MPa.\mathrm{m}^{\frac{1}{2}}$ for Al-TiN-5-5 nm-60^{0}C cases. Moreover, for Cu-TiN cases, the values show the scattering at the range of 1.498-2.995 $MPa.\mathrm{m}^{\frac{1}{2}}$ for 50-50 nm-200^{0}C, 2.196-4.257 $MPa.\mathrm{m}^{\frac{1}{2}}$ for 50-50 nm-100^{0}C, 1.377-2.993 $MPa.\mathrm{m}^{\frac{1}{2}}$ for 5-5 nm-200^{0}C, and 1.915-3.387 $MPa.\mathrm{m}^{\frac{1}{2}}$ for 5-5 nm-100^{0}C. There are clearly systematic effects in the ranges of K_I as evidenced by the increasing trend with a observed in Figure 5. For both temperature and layer thickness cases, the Al-TiN and Cu-TiN K_I remains close to the fracture toughness found in the literature. However, for Al-TiN nanocomposites, the TiN in 5-5nm-60^{0}C case seems to have higher crack driving force than the 50-50nm layer thickness. On the other hand, crack driving force in 50-50 nm-100^{0}C seems to be higher than all the other Cu-TiN cases. Considering all these, it is found that adding the Al or Cu layer does not significantly improve the TiN layer fracture toughness and it would behave on par with a single TiN thin film. The low value of fracture toughness observed in Figure 3 for Al and Cu layers compared to the individual fracture toughness of the materials, suggest that shielding benefits of the composite are being undermined by fracture contributors such as grain boundaries, weak interfaces, or residual tensile stress fields.

Mishra et. al., 2020[6] studied fracture toughness tests in macroscale of single edge-notched clamped beam specimens (SENCB) to find out the effect of geometry on the stability of crack growth in brittle materials. They not only suggested geometric factors for SENCB structures by FE modeling but also observed that the aspect ratio of the beam controls the crack growth i.e., at and $\frac{S}{W} = 4$ the crack will be stable at $\frac{a}{W} = 0.35$ and $\frac{S}{W} = 8$ the stable crack will be at $\frac{a}{W} = 0.6$. Moreover, at proper design of beam geometry, valid fracture toughness tests can be performed without fatigue pre-cracking for brittle materials[26]. The geometric factor suggested by Mishra et.

al. for and $\frac{S}{W}$ = 4 is shown in Figure 3 a and c. It can be observed that the curve is similar to the results obtained by this study and variation might have occurred because of the inconsistencies in beam geometry and the effect of using heterogeneous materials. Based on their analysis and our results, we propose some future recommendation for designing similar experiments:

- While performing FIB, if possible, only the beam should be machined. In this way, the effect of leg geometry and moment introduced by the leg on K_I can be avoided. The changes in moment will result in unloading the crack tip after a large unstable crack growth event. This might be leveraged in leg design to stop the crack at an $\frac{a}{W}$ much smaller than 0.5.
- It is ideal for $\frac{S}{W}$ from 4 to 6 for fracture toughness tests since it will provide largest range of stable crack growth[6]. The beam dimensions should follow this range. Then bending can be used instead of fatigue for pre-cracking. In other words, during pre-cracking by bending the crack will stop at an advantageous location by choosing proper and $\frac{S}{W}$.
- It was also observed during the experiment that the higher $\frac{a}{W}$ ratios the cracking occurs at the fixed end because crack is stable at higher $\frac{a}{W}$ ratios causing to need larger load for the crack to propagate. A tapered beam might be a way to solve this issue as suggested by Cui et. al[41].
- Cono-spherical indenter instead of roller type indenter was used to perform these experiments. Although the cono-spherical shape indenter does not have any effect on the experiment being performed in plain strain conditions (verified by FE simulations), the indenter interaction zone is about 31% higher than what it is predicted by the Hertz theory[34, 35] which causes interaction between indenter stress field under contact point and field around crack tip at a/W>0.65. In order to negate this issue, we recommend to use indenter with larger radius of curvature for shorter beams so that the stress field under the indenter can be smaller[6].
- The next step after this study could be performing SENCB tests for composite material keeping the and $\frac{S}{W}$ and $\frac{a}{W}$ under the recommended value. Moreover, fracture toughness can be predicted by using the crystal plasticity and make R-curve for composite materials.

5. Conclusions

FEM is used to simulate the fields of stress at crack tip locations and determine the underlying shape functions for estimating the fracture toughness of multi-layer metal-ceramic Cu/TiN and Al/TiN nanocomposites. In doing so, the effects of specialized geometry of MSENB specimens as measured using *in situ* SEM, cono-spherical indenter stress fields, and phase interface shielding/anti-shielding on the crack tip driving force are studied. The J and interface integrals are used in the calculations. Although the indenter is analogous to a point load, the J-integral along the crack front is found to be in plane strain. The bending stress away from and under the indenter are similar and the J-integral does not vary substantially under the indenter. The interaction between the crack tip and the indenter stress occurs at 3.5 of the indenter contact radius. The simulations reveal that the design of specimen geometry against the bending moment variation is fundamental for successful MSENB testing. The boundary conditions on the legs lead to a rise in the force needed to drive the crack as the beam goes from simply supported to a fix beam configuration. As a result, the indenter interaction zone i.e., the indenter contact area increases. Since the SENB geometric factor does not account for this change, K_I increases with decrease in crack ligament length. K_I results are presented for several Cu/TiN and Al/TiN nanocomposites varying in their layer thickness and at different temperatures. The K_I values appear largely independent of crack length, suggesting that the MSENB technique has promise to be generalized if legs are better designed. Furthermore, it gives some confidence that the pre-fatigued is not a dominate component in getting the toughness. Analyses of the results suggests that adding either Al or Cu nanolayers to TiN nanolayers does not weaken or significantly improve fracture toughness relative to the single TiN thin film. The crack tip driving force for a given load goes down due to shielding, which means the load must increase to reach the effective K_{IC} for the Al and Cu layers. This would allow the composite to bare a greater load and effectively raises the toughness of the composite over its constituents. However, the effective fracture toughness of the Al and Cu layers appears substantially reduced and shielding benefits are not observed.

Acknowledgments

S.B., D.J.S., and M.K. gratefully acknowledge support from the U.S. National Science Foundation (NSF) under grant No. CMMI-1727495. D.J.S would also like to acknowledge the Office of Experimental Sciences (Science Campaign C1) and the G. T. Seaborg Institute for partial support.

Appendix

From Figure A 1-4 shows crack propagation during 3-point bending experiments while increasing the load for Cu/TiN (50nm-50nm), Cu/ TiN (5nm-5nm), Al/ TiN (50nm-50nm), Al/ TiN (5nm-5nm).

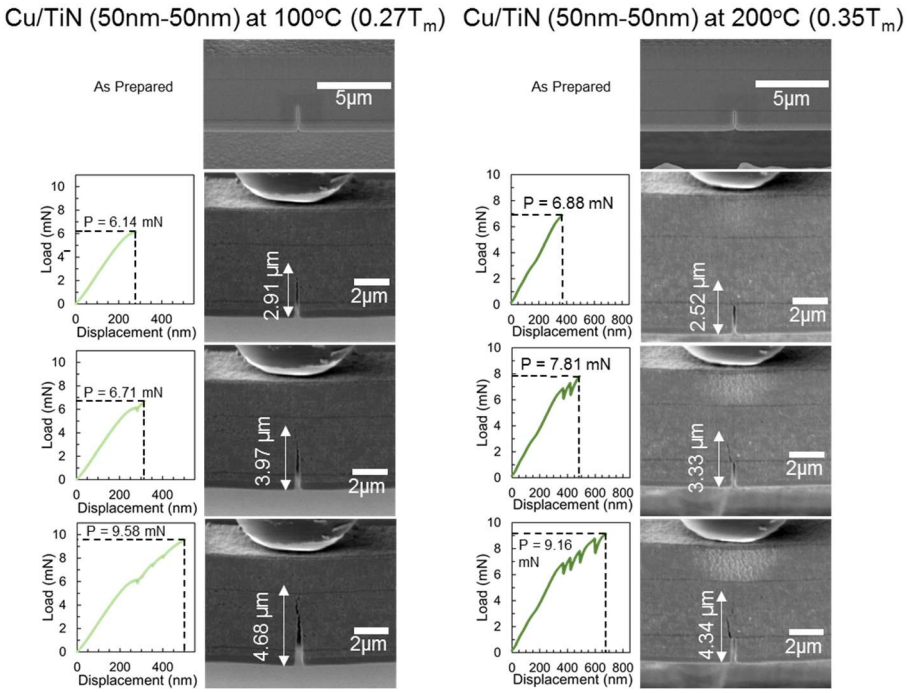

Figure A 4: Crack Propagation in Cu/TiN 50nm-50nm layers at 100^{0}C (0.27T$_m$) and 200^{0}C (0.35T$_m$).

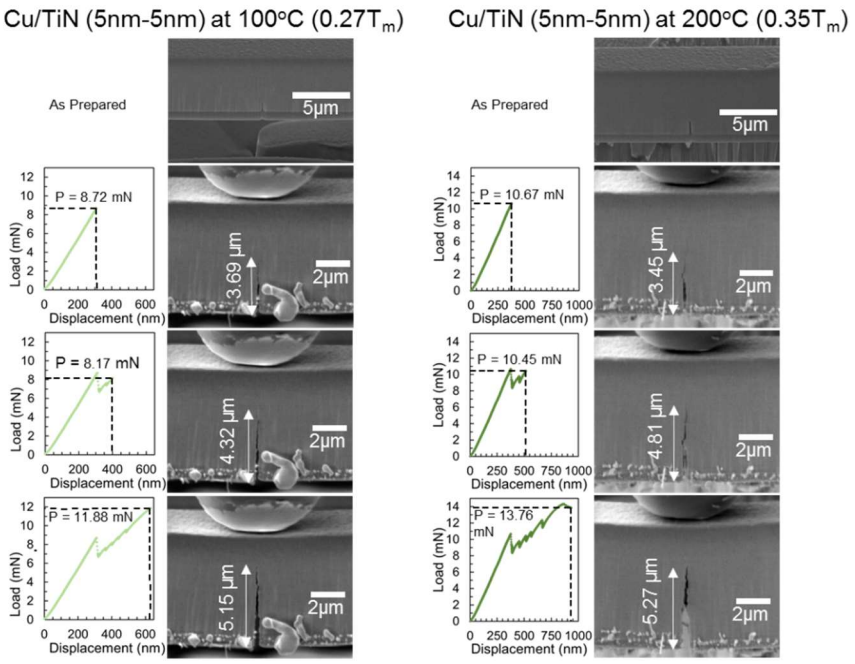

Figure A 5: Crack Propagation in Cu/TiN 5nm-5nm layers at 100^0C (0.27T_m) and 200^0C (0.35T_m).

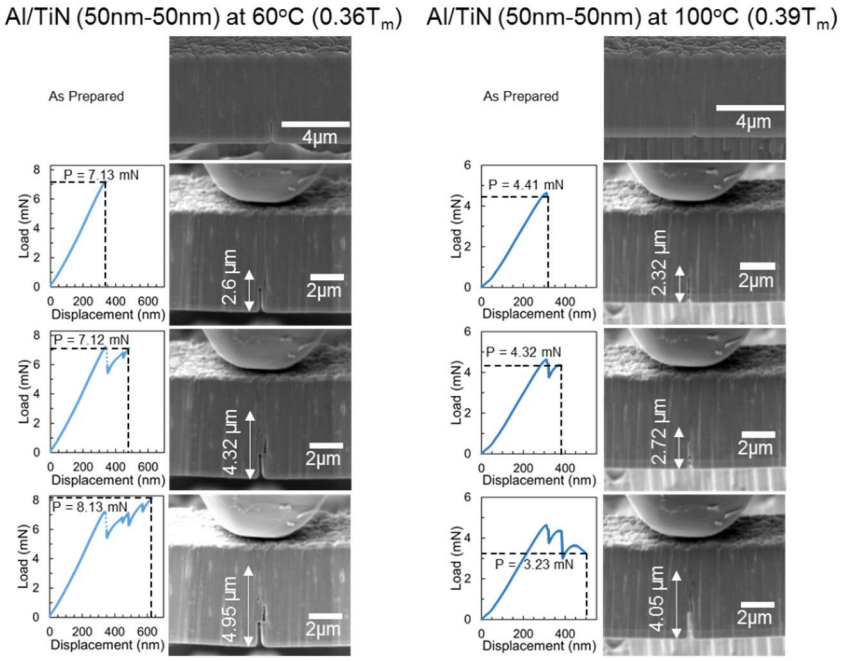

Figure A 6: Crack Propagation in Al/TiN 50nm-50nm layers at 60^0C (0.36T_m) and 100^0C (0.39T_m).

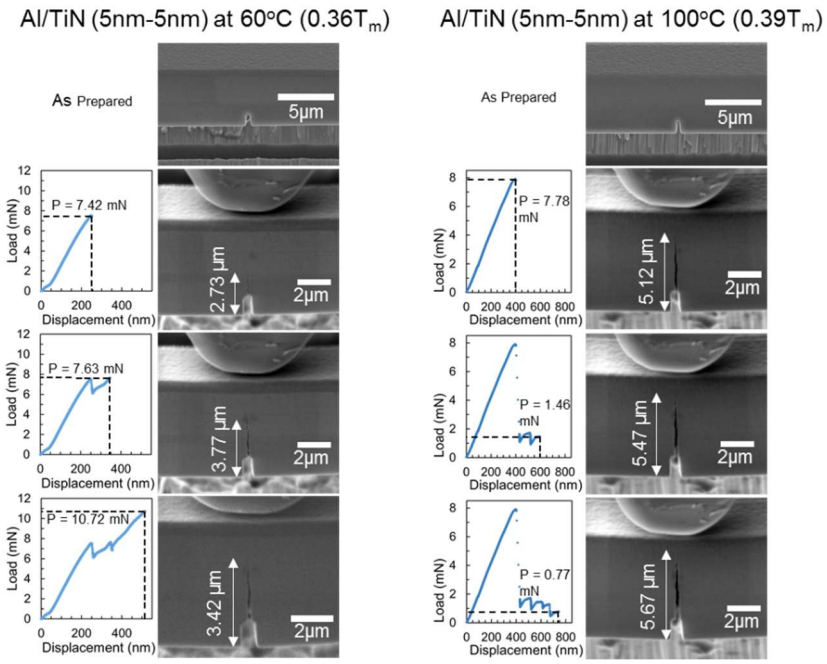

Figure A 7:Crack Propagation in Al/TiN 50nm-50nm layers at 60^{0}C (0.36T$_m$) and 100^{0}C (0.39T$_m$).

The ratio (r) of stress at metal and ceramic layer changes with the number of bilayers left at ligament. According to the beam theory, the ratio will converge after about 17 layers.

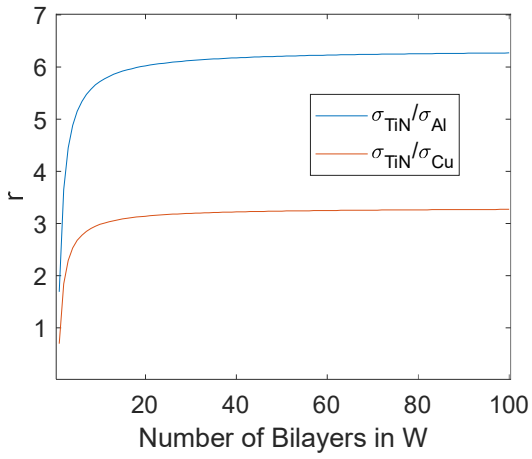

Figure A 5. Ratio r of bend stress calculated using Eq. (10) as a function of the number of bilayers in W.

Stress fields are generated during simulation for 50-50nm layer case. The stress filed looks similar for all the cases but the maximum Von Misses stress is different based on the location of crack tip.

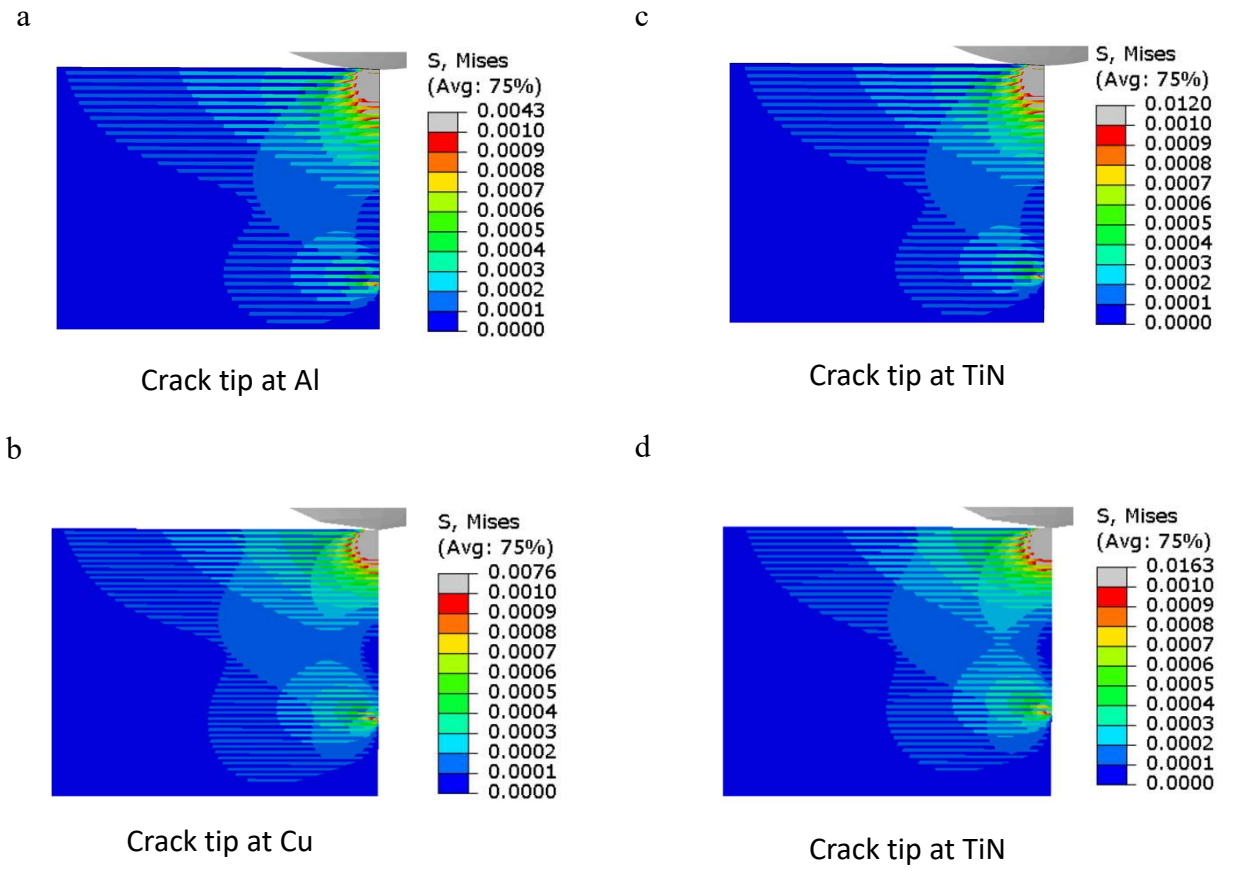

Figure A 6. Representation of stress fields (50 nm layer thickness (Quarter Model) at the displacement of indenter of 50nm. (a) & (c) Al-TiN-60C; (b) & (d) Cu-TiN-100C. Note: In order to observe the stress fields properly, a certain value of Von Misses (VM) stress is used as the contour limit. The values higher than the limit is shown as grey color in the figure. Moreover, stress values are in $N/\mu m^2$. Where, 1 MPa = 10^6 $N/\mu m^2$.

A 20*20*20 μm block with E = 68.5 GPa and ν = 0.32 was used to regenerate the Hertz equation. The contact between indenter and block has been assumed to be frictionless and hard with rigid indenter. The element type under the indenter is C3D8 (An 8-node linear brick) and for the rest of block C3D4 (A 4-node linear tetrahedron) is used to make the simulation faster. The Figure c shows that with this mesh density Hertz theory has been replicated within 1% error.

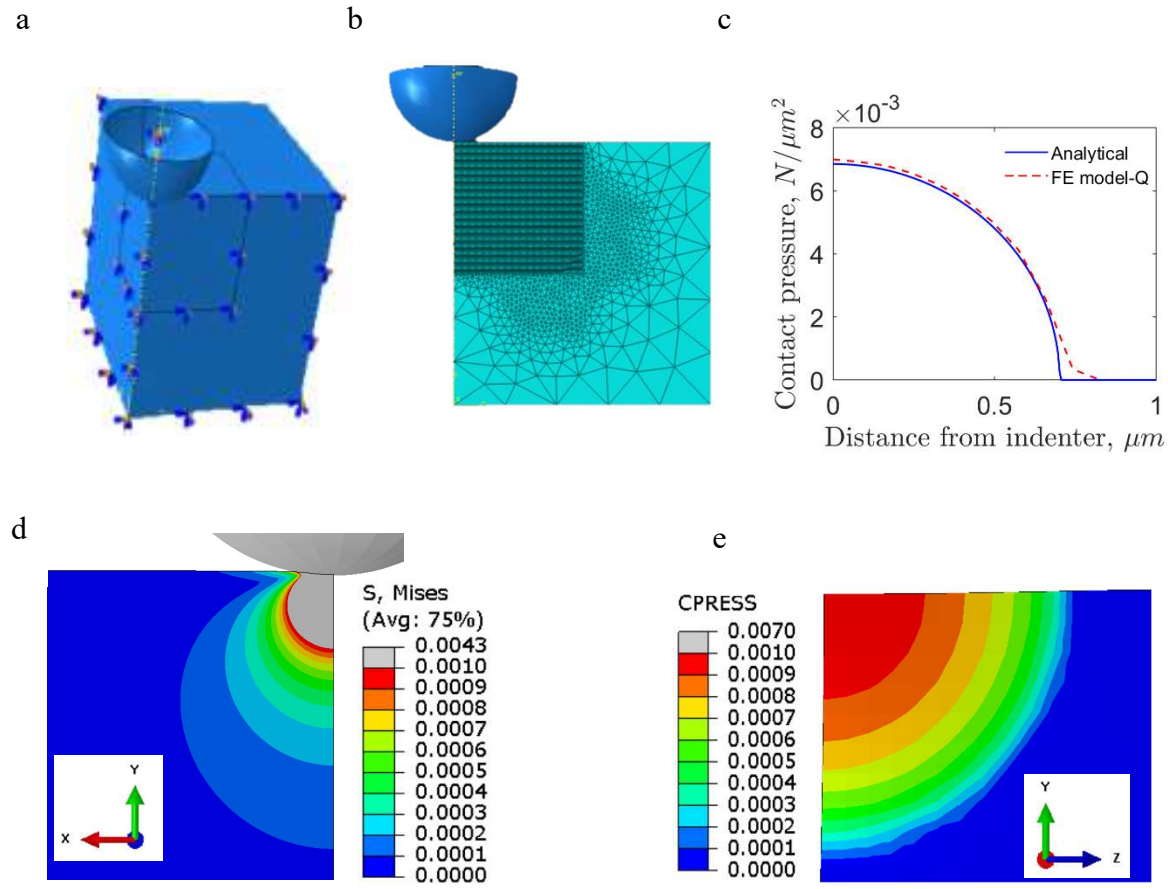

Figure A 7. Hertz equation regeneration. a) BC (Z and X axis symmetry); b) Mesh design; c) Contact pressure distribution from center and comparison with analytical solution; d) Von Misses stress distribution; e) Contact pressure distribution.

The crack lengths used in the simulations are shown in table A1. It should be noted that there are more crack lengths in the table than actually measured during the experiments in order to fit more accurately to get the geometric factor (shown in Figure 3). The crack length obtained from the experiments are shown in bold letter. For Al-TiN-60^{0}C-5-5 nm case, S, W, B values are kept same

as Al-TiN-60^{0}C-50-50 nm for comparison purposes instead of matching the dimensions of the experimental values. That is why the crack lengths are also tried to keep similar to the Al-TiN-60^{0}C-50-50 nm case (the similar crack length values are shown in italic and the minor difference is because of the modification required for the crack tip to be at the center of each layer to make the meshing operation easy).

Table A 1. Crack lengths used to get the shape functions for each simulated beam. The crack length obtained from the experiments are shown in bold letters. For Al-TiN-60^{0}C-5-5 nm case, S, W, B values are kept same as Al-TiN-60^{0}C-50-50 nm for comparison purposes instead of matching the dimensions of the experimental values. That is why the crack lengths are also tried to keep similar to the Al-TiN-60^{0}C-50-50 nm case (the similar crack length values are shown in italic and the minor difference is because of the modification required for the crack tip to be at the center of each layer to make the meshing operation easy).

Simulated beam	a, μm	Layer where crack tip is in
Al-TiN-60^{0}C-50-50 nm	2.47	TiN
	2.68	TiN
	2.74	Al
	2.90	Al
	3.21	**Al**
	3.40	Al
	3.93	**TiN**
	4.14	**TiN**
	4.65	**Al**
Al-TiN-100^{0}C-50-50 nm	**2.63**	**Al**
	2.68	TiN
	2.81	Al
	3.04	**Al**

	3.07	TiN
	3.24	TiN
	3.30	Al
	3.52	**TiN**
	4.16	TiN
	4.185	Al
Cu-TiN-100^0C-50-50 nm	2.37	TiN
	2.70	TiN
	2.75	**Cu**
	3.13	**TiN**
	3.23	**TiN**
	3.28	Cu
	3.49	Cu
	3.71	**Cu**
	3.76	TiN
	4.44	**Cu**
	4.51	TiN
	4.76	**Cu**
Cu-TiN-200^0C-50-50 nm	2.54	Cu
	2.61	**TiN**
	2.90	**Cu**

	3.15	TiN
	3.32	**Cu**
	3.61	TiN
	3.76	**Cu**
	3.94	TiN
	4.25	TiN
	4.30	Cu
	4.80	TiN
Al-TiN-60^{0}C-5-5 nm	*2.60*	TiN
	2.90	TiN
	3.22	TiN
	3.30	Al
	3.90	Al
	4.00	TiN
	4.14	Al
Cu-TiN-100^{0}C-5-5 nm	2.90	Cu
	3.25	TiN
	3.69	**TiN**
	4.05	TiN
	4.23	**Cu**
	5.17	Cu

Table A 2: Experimentally measured crack lengths for Al-TiN-60^{0}C-5-5 nm

	Experimental crack lengths
Al-TiN-60^{0}C-5-5 nm	2.67
	3.75
	4.39

Table A 3-4 shows the load values at various crack lengths in experiments. The load values mentioned in the tables are used to calculate the fracture toughness. The beam used for simulation are shown in bold letters.

Table A 3: Load (μN) at various crack lengths in experiment for Cu/TiN 50nm-50nm layers at 100^{0}C (0.27T_m) and 200^{0}C (0.35T_m). The experiment used for simulation are shown in bold letters.

Temperature	Experiment number	Load,μN	a, μm
200 ^{0}C (0.35T_m)	A	6243.8	3.745077
		6733	3.755901
		7221.1	3.810021
		7447	3.939908
	B	5685.1	1.948306
		7819.8	3.571894
		8310.9	3.701781
	C	**6846.1**	**2.608565**
		7269.5	**2.900811**
		7794.3	**3.322944**
		8736.1	**3.755901**
100 ^{0}C (0.27T_m)	**D**	**6199.7**	**2.749276**
		6381.8	**3.128113**
		6874.5	**3.236353**
		7374.6	**3.712605**
		9525.2	**4.437808**
		7976.7	**4.762526**
	G	6127.2	3.138937

		6467	3.745077
		6711	3.86414
		7468.6	4.048147
		8192	4.22133
		9560.1	4.740878

Table A 4: Load (μN) at various crack lengths in experiment for Cu/TiN 5nm-5nm layers at 100^0C (0.27Tm) and 200^0C (0.35Tm). The experiment used for simulation are shown in bold letters.

Temperature	Experiment number	Load,μN	a, μm
$200\ ^0$C ($0.35T_m$)	C	3600	3.23
		4135	3.38
		4170	3.44
		4370	3.62
	D	7635.8	3.36624
		9602.6	5.011476
		11300.6	5.184659
		9527	5.5202
	E	7132.5	3.810021
		7669.7	4.47028
		8317.4	4.621815
		8691.5	4.827469
		11110.5	5.141363
		6853.3	5.628439
	F	9161.8	3.56107
		9770.6	4.47028
		10412.7	4.979004
		10877.3	5.011476
		12305.2	5.173835
		13763.6	5.758327
$100\ ^0$C ($0.27T_m$)	A	6671.8	4.123914
		8021.7	4.481104
		8803.2	4.654286
		9453.6	5.000652
		12185	5.087243
		14226.4	5.32537

	B	**7009**	**3.690957**
		7611	**4.232154**
		8158.1	**4.405336**
		8766.4	**4.805821**
		9557.1	**4.805821**
		11856	**5.173835**
	G	9023.6	3.333768
		11776.9	4.849117
		14346.2	5.476905

Table A 5: Load (μN) at various crack lengths in experiment for Al/TiN 50nm-50nm layers at 60^0C ($0.36T_m$) and 100^0C ($0.39T_m$). The experiment used for simulation are shown in bold letters.

Temperature	Experiment number	Load,μN	a, μm
100^0C ($0.39T_m$)	D	4872.6	2.933283
		5271.1	4.015675
		5463.7	4.015675
		5745.6	4.015675
		7052.8	4.091443
		7563	4.199682
	E	3918	3.11729
		3910.1	3.387888
		4618.5	4.199682
	F	**4413.9**	**2.630213**
		4322.4	**3.06317**
		3230.3	**3.528599**
	G	5127	2.944107
		7210.3	4.048147
		7791.7	4.329569
60^0C ($0.36T_m$)	A	6456.6	3.56107
		7208.7	3.972379
		8596.7	4.567695
		9936.5	4.740878
	B	**5935.8**	**3.225529**
		7180.6	**3.929084**

		8196.7	**4.145562**
		9221.6	**4.654286**
		9650.3	**4.903237**
	C	5783.2	2.738452
		6823.4	3.820844
		7117.9	4.362041
		7730.8	4.686758
		8134.5	5.098067

Table A 6: Load (μN) at various crack lengths in experiment for Al/TiN 5nm-5nm layers at 60^0C ($0.36T_m$) and 100^0C ($0.39T_m$).

Temperature, ^{0}C	Experiment number	Load,μN	a, μm
100^0C ($0.39T_m$)	C	8096.661	5.75
		9940	6.06
		8096.661	6.15
	H	3500	4.17
		4520	4.49
		5200	4.64
		5990	4.7
		6370	5
		6940	5.15
60^0C ($0.36T_m$)	F	7424.1	2.673509
		7631.9	3.755901
		10721.7	4.394512
	G	7137	3.084818
		6311.2	3.247177
		7840.3	3.409535

References

1. C. Hwu and Y.-K. Yeh: Prediction of fracture toughness for carbon nanotubes *Procedia Structural Integrity.* **2**, 1327 (2016).

2. N. Jaya B, V. Jayaram and S.K. Biswas: A new method for fracture toughness determination of graded (Pt, Ni) Al bond coats by microbeam bend tests *Philosophical Magazine.* **92**(25-27), 3326 (2012).

3. J. Ast, M. Ghidelli, K. Durst, M. Göken, M. Sebastiani and A. Korsunsky: A review of experimental approaches to fracture toughness evaluation at the micro-scale *Materials & Design.* **173**, 107762 (2019).

4. E. Astm: Standard test method for measurement of fracture toughness *ASTM, Annual Book of Standards.* (E1820-20AE01).

5. N.K. Simha, F.D. Fischer, O. Kolednik, J. Predan and G.X. Shan: Crack Tip Shielding or Anti-shielding due to Smooth and Discontinuous Material Inhomogeneities *International Journal of Fracture.* **135**(1-4), 73 (2005).

6. A.K. Mishra, A. Lambai, V. Jayaram and B.N. Jaya: The edge-notched clamped beam bend specimen as a fracture toughness test geometry *Theoretical and Applied Fracture Mechanics.* **105**, 102409 (2020).

7. K.-N. Tu, J.W. Mayer and L. Feldman: Electronic thin film science for electrical engineers and materials scientists (Macmillan, City, 1992).

8. S. Vepřek, S. Reiprich and L. Shizhi: Superhard nanocrystalline composite materials: the TiN/Si3N4 system *Applied physics letters.* **66**(20), 2640 (1995).

9. M. Ueda, M. Silva, C. Otani, H. Reuther, M. Yatsuzuka, C. Lepienski and L. Berni: Improvement of tribological properties of Ti6Al4V by nitrogen plasma immersion ion implantation *Surface and Coatings Technology.* **169**, 408 (2003).

10. Z. Chen and Z. Gan: Fracture toughness measurement of thin films on compliant substrate using controlled buckling test *Thin Solid Films.* **515**(6), 3305 (2007).

11. G. Dehm, C. Motz, C. Scheu, H. Clemens, P.H. Mayrhofer and C. Mitterer: Mechanical size-effects in miniaturized and bulk materials *Advanced Engineering Materials.* **8**(11), 1033 (2006).

12. O. Kraft and P. Gruber: M önig R, Weygand D *Ann Rev Mater Res.* **40**, 293 (2010).

13. A. Chokshi, A. Rosen, J. Karch and H. Gleiter: On the validity of the Hall-Petch relationship in nanocrystalline materials *Scripta metallurgica.* **23**(10), 1679 (1989).

14. Z. Xia, W. Curtin and B. Sheldon: A new method to evaluate the fracture toughness of thin films *Acta materialia.* **52**(12), 3507 (2004).

15. G. Pharr, D. Harding and W. Oliver: Measurement of fracture toughness in thin films and small volumes using nanoindentation methods, in Mechanical Properties and Deformation Behavior of Materials Having Ultra-Fine Microstructures, (Springer, City, 1993), pp. 449.

16. E.I. Preiß, F. Gannott, M. Göken and B. Merle: Scaling of the fracture toughness of freestanding metallic thin films with the yield strength *Materials Research Letters.* **6**(10), 607 (2018).

17. A.J. Blattner, R. Lakshminarayanan and D.K. Shetty: Toughening of layered ceramic composites with residual surface compression: effects of layer thickness *Engineering Fracture Mechanics.* **68**(1), 1 (2001).

18. R.M. Jones: Mechanics of composite materials (CRC press, City, 1998).

19. M. Herráez, A. Fernández, C.S. Lopes and C. González: Strength and toughness of structural fibres for composite material reinforcement *Philos Trans A Math Phys Eng Sci.* **374**(2071), 20150274 (2016).

20. Q.-Z. Wang: A sandwich three-point bend specimen for testing mode-I interlaminar fracture toughness for fiber-reinforced composite materials *International journal of fracture.* **85**(3), 231 (1997).

21. G. Cooper: The fracture toughness of composites reinforced with weakened fibres *Journal of Materials Science.* **5**(8), 645 (1970).

22. G.A. Gogotsi: Fracture toughness of ceramics and ceramic composites *Ceramics international.* **29**(7), 777 (2003).

23. S.T. Pinho, P. Robinson and L. Iannucci: Fracture toughness of the tensile and compressive fibre failure modes in laminated composites *Composites science and technology.* **66**(13), 2069 (2006).

24. D.J. Savage, I.J. Beyerlein, N.A. Mara, S.C. Vogel, R.J. McCabe and M. Knezevic: Microstructure and texture evolution in Mg/Nb layered materials made by accumulative roll bonding *Int. J. Plast.* **125**, 1 (2020).

25. M. Knezevic, T. Nizolek, M. Ardeljan, I.J. Beyerlein, N.A. Mara and T.M. Pollock: Texture evolution in two-phase Zr/Nb lamellar composites during accumulative roll bonding *Int. J. Plast.* **57**(0), 16 (2014).

26. C.F. Shih, B. Moran and T. Nakamura: Energy release rate along a three-dimensional crack front in a thermally stressed body *International Journal of Fracture.* **30**(2), 79 (1986).

27. B. ASME: ASME code for pressure piping *ASME.* (2001).

28. W. Meng and G. Eesley: Growth and mechanical anisotropy of TiN thin films *Thin Solid Films.* **271**(1-2), 108 (1995).

29. M.A. Hopcroft, W.D. Nix and T.W. Kenny: What is the Young's Modulus of Silicon? *Journal of Microelectromechanical Systems.* **19**(2), 229 (2010).

30. D.M. Parks: The virtual crack extension method for nonlinear material behavior**12**(3), 353 (1977).

31. F.Z. Li, C.F. Shih and A. Needleman: A comparison of methods for calculating energy release rates**21**(2), 405 (1985).

32. C.E. Freese and F.I. Baratta: Single edge-crack stress intensity factor solutions *Engineering Fracture Mechanics.* **73**(5), 616 (2006).

33. C. Chen, J. Pascual, F. Fischer, O. Kolednik and R. Danzer: Prediction of the fracture toughness of a ceramic multilayer composite–Modeling and experiments *Acta materialia.* **55**(2), 409 (2007).

34. H. Hertz: Über die berührung fester elastischer Körper (On the contact of rigid elastic solids) In: Miscellaneous Papers *Jones and Schott, London.* (1896).

35. H. Hertz: On the contact of solids—on the contact of rigid elastic solids and on hardness *Miscellaneous papers.* 146 (1896).

36. A.-N. Wang, G.-P. Yu and J.-H. Huang: Fracture toughness measurement on TiN hard coatings using internal energy induced cracking *Surface and Coatings Technology.* **239**, 20 (2014).

37. S. Massl, W. Thomma, J. Keckes and R. Pippan: Investigation of fracture properties of magnetron-sputtered TiN films by means of a FIB-based cantilever bending technique *Acta Materialia.* **57**(6), 1768 (2009).

38. M. Manoharan, A. Desai and M.A. Haque: Fracture toughness characterization of advanced coatings *Journal of Micromechanics and Microengineering.* **19**(11), 115004 (2009).

39. G. Wei, B. Bhushan and S.J. Jacobs: Nanoscale fatigue and fracture toughness measurements of multilayered thin film structures for digital micromirror devices *Journal of Vacuum Science & Technology A: Vacuum, Surfaces, and Films.* **22**(4), 1397 (2004).

40. S. Kataria, S. Srivastava, P. Kumar, G. Srinivas, J. Khan, D.S. Rao and H.C. Barshilia: Nanocrystalline TiN coatings with improved toughness deposited by pulsing the nitrogen flow rate *Surface and Coatings Technology.* **206**(19-20), 4279 (2012).

41. F.Y. Cui and R.P. Vinci: A chevron-notched bowtie micro-beam bend test for fracture toughness measurement of brittle materials *Scripta Materialia.* **132**, 53 (2017).

SUMMARY

In this research, the effects of phase transformation in a HEA with low stacking fault energy, powder reusing on the mechanical properties of IN 718 fabricated by LPBF and the fracture toughness of nano layered MSENB specimens were investigated. The microstructural flexibility of a very low SFE $Fe_{42}Mn_{28}Co_{10}Cr_{15}Si_5$ (in at%) HEA was explored by changing the processing conditions. The as-rolled microstructure had triplex structure consisting of metastable γ, stable σ, and stable ε phases. The 350 RPM FSP changed mostly the grain size, however, 150 RPM FSP increased the fraction of ε phase along with refining the grain structure. The double pass (350 RPM + 150 RPM) microstructure provided increased σ phase as well as refining grain structure. During compression, the metastable γ transformed to stable ε phases. The material with higher amount of ε and σ phases provided higher strength because of highly dislocated ε phase fraction and transformation induced dynamic Hall-Petch-type barrier effect. The material with higher amount of γ phase and lower TRIP rate exhibited higher strain to fracture. The TRIP rate was observed to increase with the initial content on γ and favorable texture i.e., more grains with the <001> orientation parallel to a compression direction. The γ phase texture exhibited {110} fiber along the compression direction, while the texture formation of the ε phase was primarily driven by the variant selection of the TRIP mechanism. A decrease of $\frac{c}{a}$ ratio of ε with compressive strain was also observed which could be an indication of activating non-basal slip systems contributing to the ductility of the alloy.

HIPPed and then heat treated (AMS 2774) Inconel 718 rods, fabricated from both virgin and reused powders, were used to analyze the tensile, compressive and creep strength. It was observed that the reused powder samples had higher strength because of higher dispersion hardening relative to the virgin category samples at room temperature. Although both category samples provided serrated behavior at high temperature, it was absent for virgin powder category at 650^0, 700^0C, and 750^0C mainly because of the difference in solute atom (Nb) content at these temperatures. Furthermore, the samples made by virgin powder samples provided higher creep life until 650^0C. However, the presence of higher dislocation density in the reused powder samples and its interaction with precipitates (especially δ) played vital role during creep tests and provided higher creep life at 700^0C.

Lastly, FEM analysis of experiments, performed on specialized geometry of MSENB specimens, was performed to obtain geometric factor and ultimately fracture toughness of nano-layered composites by using J and interface integrals. It was found that boundary conditions on the legs led to a rise in the force needed to drive the crack as the beam went from simply supported to a fix beam configuration. As a result, the indenter interaction zone i.e., the indenter contact area increased. Moreover, as the SENB geometric factor did not account for this change, K_I increased with decrease in crack ligament length. K_I results were presented for several Cu/TiN and Al/TiN nanocomposites varying in their layer thickness and at different temperatures. The K_I values appeared largely independent of crack length. It was also observed that adding Al or Cu did not significantly improve or weaken the fracture toughness relative to the single TiN thin film. However, the crack tip driving force for a given load needed to go down due to shielding, which meant that the load had to increase to reach the effective K_{IC} for the Al and Cu layers, consequently higher capability of bearing load.

Future work will include performing tensile and nano hardness tests on DP-5Si-HEA, phase analysis of crept samples, analyzing fracture toughness using polycrystal plasticity finite element analysis.